Near Real-Time Precise Orbit Determiation of Low Earth Orbit Satellites Using an Optimal GPS Triple-Differencing Technique

by

Tae-Suk Bae

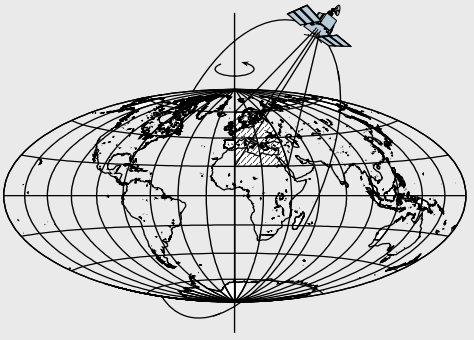

Report No. 481

Geodetic Science and Surveying

The Ohio State University
Columbus, Ohio 43210

November 2006

NEAR REAL-TIME PRECISE ORBIT DETERMINATION OF LOW EARTH ORBIT SATELLITES USING AN OPTIMAL GPS TRIPLE-DIFFERENCING TECHNIQUE

by

Tae-Suk Bae

The Ohio State University
2006

ABSTRACT

During the last decade, numerous Low Earth Orbit (LEO) satellites, including TOPEX/POSEIDON, CHAMP and GRACE, have been launched for scientific purposes at altitudes ranging from 400 km to 1300 km. Because of highly complex dynamics of their orbits, coming from the Earth gravity field and the atmospheric drag, accurate and fast LEO orbit determination has been a great research challenge, especially for the lowest altitudes. To support GPS meteorology that requires an accurate orbit in near real-time, efficient LEO orbit determination methods were developed using the triple-differenced GPS phase observations, as presented in this dissertation. These methods include the kinematic, dynamic, and reduced-dynamic approach based on the wave algorithm.

To test the developed algorithms, 24 hours of CHAMP data on February 15, 2003, which amounts to 15 revolutions, were used for each method. The EIGEN2 geopotential model was used with degree and order up to 120. Precise IGS orbits are used for the GPS satellites, and 43 IGS ground tracking stations were chosen using the algorithm developed in this study, based on the network optimization theory. The estimated orbit solutions were compared with the published Rapid Science Orbit (RSO) and the consistency testing was performed for the dynamic solution. In addition to the comparison with other orbit solutions, the SLR residuals were also computed as an independent validation of the methods presented here.

The kinematic orbit solution depends on the satellite geometry and data quality. The absolute kinematic positioning solution, with an RMS error of ±26 meters in 3D, was used as an initial approximation for the kinematic orbit determination. Because of the inaccuracy of the initial approximated orbit, there is a bias up to a few hundred epochs in the kinematic solution. This bias is effectively removed with the backward filter by fixing the last epoch from the forward filter solution. After the forward and backward filtering, the kinematic approach shows accuracy better than ±20 cm in 3D RMS for a half day arc compared to the reference RSO.

The dynamic approach requires careful modeling of the atmospheric drag force which is the most dominant nonconservative force at LEO's altitude. In addition, the empirical force modeling, which is similar to the stochastic process noise in the reduced-dynamic approach, absorbs most of the remaining unmodeled forces. The two frequencies of the empirical forces, that is, once- and twice-per-revolution, are modeled in this study. Also after a thorough testing of the most suitable size of the arc length for the atmospheric drag parameters, the scaling factors for the drag force are estimated every

hour. With this careful modeling, the dynamic solution shows an agreement within ±8 cm in position and ±0.12 mm/s in velocity of RSO. The computation time of the dynamic solution for the 24-hour arc is 2.5 hours on a 3 GHz PC platform.

The wave algorithm, as implemented in this study, for the LEO precise orbit determination (POD) represents a new approach to the reduced-dynamic technique. This approach shows a better fit to RSO for each tested segment. However, there is slightly larger bias in its solution, thus, the overall RMS of fit is comparable to the dynamic orbit solution. This follows from the fact that the concept of the reduced-dynamic approach is already incorporated in the dynamic orbit determination in the form of the empirical force modeling. Therefore, there is no room for further improvement by the process noise modeling to take care of the unmodeled forces. A simplified force model is considered for future study in conjunction with the wave filter approach.

The CHAMP orbit is successfully estimated in this study to support, for example, the GPS meteorology, using a new method that is accurate as well as fast and efficient. The applied wave algorithm shows the possibility of further improvement in the RMS of fit as long as the bias is modeled appropriately. The hypothesis testing indicates that the estimated dynamic solution of this study is consistent with the published RSO, thus, further accuracy improvement cannot be expected without other types of measurements, while its easy and time-effective implementation represents the major improvement, as compared to the existing solutions. Also, the SLR residual test shows that the CHAMP orbit solution estimated in this study is comparable to solutions determined by other analysis centers, such as JPL and GFZ.

PREFACE

This report was prepared by Tae-Suk Bae under the supervision of Professor Dorota A. Grejner-Brzezinska, Department of Civil and Environmental Engineering and Geodetic Science, The Ohio State University. This report was originally submitted to the Graduate School of The Ohio State University in partial fulfillment of the requirements for the Ph.D. degree.

This research was supported by the grants from NASA (NASA NIP Project, OSURF #740809).

ACKNOWLEDGMENTS

I wish to express my deepest gratitude to my adviser, Dr. Dorota A. Grejner-Brzezinska, for her support, encouragement, and professional guidance throughout this research. My sincere appreciation also goes to my dissertation committee, Drs. Alan Saalfeld, Ralph von Frese, Clyde Goad (Topcon Positioning Systems), and Jim Ray (NOAA/NGS), for their invaluable advice and comments.

I am indebted to Drs. Burkhard Schaffrin, Christopher Jekeli, and C.K. Shum for their many lectures regarding the fields of adjustment and geodesy, both of which were strong bases of my research. Many valuable comments and discussions held with Drs. Henno Boomkamp (ESA) and Da Kuang (JPL) are appreciated. I would also like to thank Dr. Jay Kwon (The University of Seoul) for helpful discussions and inspiration in this study.

I am very grateful for the discussion and collaboration with my colleagues, Chang-Ki Hong and Sangho Baek. I also would like to thank Karla Edwards for pointing out the grammatical errors and inconsistencies in the draft.

Finally, a special thanks to my wife, Jisu Lee, and sons, Sun-Woong and Insu, for their constant enthusiasm and tolerance during the many years of my graduate studies.

TABLE OF CONTENTS

CHAPTER 1

INTRODUCTION

During the last two decades, numerous Low Earth Orbit (LEO) satellites have been launched for scientific purposes at altitudes ranging from 400 km to 1300 km, including TOPEX/POSEIDON (Tapley et al., 1994), CHAMP (Reigber et al., 2002; CHAMP, 2005), JASON-1 (JASON, 2005), GRACE (GRACE, 2005), ICESat (ICESat, 2005). The first multi-satellite constellation FORMOSAT-3/COSMIC was launched in April 2006 (COSMIC, 2006), and more new missions are expected in the next few years. For example, the CHAMP (CHAllenging Minisatellite Payload, launched in July 2000) mission is designed for static Earth gravity field recovery, magnetic field mapping, and atmospheric and ionospheric profiling. The CHAMP satellite, managed by the German GeoForschungsZentrum (GFZ), was placed in an almost circular, near polar orbit with an initial altitude of 454 km. The recent LEO missions carry space-grade Global Positioning System (GPS) receivers onboard, and the measurements to the GPS satellites are used as observations for the precise orbit determination (POD) of these satellites. To meet the science mission objectives, precise orbit determination of the LEO satellites must be guaranteed, although the required accuracy may be different for various applications. For example, 4 cm of vertical coordinate error of a tracking ground station can introduce more than 10 mm bias in the total zenith delay (TZD), depending on the quality of the GPS orbit solutions (Ge et al., 2002).

The primary objective of the research presented here is to provide an accurate LEO orbit for GPS meteorology in near real-time. An acceptable time delay for "near" real-time orbit should be no longer than 2 hours for a 3-hour arc (König et al., 2002). The contribution of ±50 cm of GPS orbit error for a 1000 km baseline would result in ±1 mm precipitable water vapor (PWV) error, which is equivalent to ±6 mm TZD error (Rocken et al., 1995). Assuming the LEO orbit error has a similar impact as GPS orbit error, the LEO orbit accuracy should be better than ±50 cm because ±1 mm PWV is comparable to the accuracy level of radiosondes and microwave radiometers (Ge et al., 2002). Also, according to Zhao (1998), an orbit error better than ±30 cm is required to estimate the temperature profile in GPS soundings to better than ±1 degree K up to an altitude of 40 km. Therefore, the LEO orbit should be computed with an accuracy better than ±30 cm

for a 3-hour arc within 2 hours after the actual measurement.

The LEO satellites experience highly complex dynamics in their orbits, due to the significant impact of the high frequency Earth gravity field components and the atmospheric drag effects, both of which complicate the determination of an accurate orbit solution for LEO. Thus, high-accuracy and fast LEO orbit determination is a great research challenge. With the successful mission of TOPEX/POSEIDON (launched in 1992, the orbit accuracy is around ±2 cm RMS error in radial component and ±8 cm for 3D; Tapley et al., 2004), numerous efforts were undertaken to develop efficient and accurate algorithms for the precise orbit determination using GPS measurements, and these have been successfully applied to various LEO missions. With the recently improved quality of the space-grade GPS receivers, the LEO double-differenced reduced-dynamic orbit solution can be obtained in the post-mission mode at an error level of ±4-5 cm, and ±5-6 cm from the kinematic ambiguity-fixed approach (Švehla and Rothacher, 2001 and 2003; Kuang et al., 2001).

The primary POD technique for GPS satellites is the dynamic approach, because their orbits are high, and thus, smooth enough to use only the low degree/order harmonics for the gravitational effect; moreover, the atmospheric drag effect is negligible at GPS altitude. In the LEO case, however, kinematic, dynamic and reduced-dynamic techniques are used by many researchers. None of them is clearly dominant for all conditions and geometries, as each one has its pros and cons for the LEO orbit determination. Thus, a combination of these methods is often used to ensure the estimation of the best orbit solution. The kinematic approach uses only GPS measurements to determine a time series of positions of the satellite; therefore, it is a simple and efficient algorithm. However, the orbit quality is strongly dependent on the geometry and continuity of the GPS signals. For the dynamic POD, all forces acting on the satellite are computed and numerically integrated to estimate the initial state vector and other unknown dynamic parameters. Thus, accurate force modeling is a critical issue for a successful POD in the dynamic approach. Finally, the reduced-dynamic approach introduces kinematic components to the dynamic force models in the form of the process noise parameters. This means that the dynamic parameters are estimated first; then the state vector is re-estimated using the Kalman filter along with the stochastic process noise which is usually modeled as a first-order Gauss-Markov process (Bertiger et al., 1994).

The double-differenced GPS carrier phase measurements are widely used as observations in the orbit determination procedure. This is because most of the systematic measurement error sources are already removed, including the GPS satellite and receiver clock errors. Moreover, the integer ambiguity fixing, if possible, provides strong constraints to the positioning solution. In the real applications of LEO orbit determination, however, since the baselines between the tracking stations and the LEOs are normally very long (hundreds to thousands of kilometers), it is not easy to resolve the integer ambiguities, primarily due to the residual ionospheric effects (Byun and Schutz, 2001). The reported success rate of the ambiguity resolution is about 40 % for the wide-lane ambiguities (Švehla and Rothacher, 2003). In order to avoid the time-consuming and

complicated ambiguity resolution process, in this research the triple-differenced, ionosphere-free GPS carrier phase data are used as the primary observations. A triple-differencing technique for dynamic orbit determination was first applied for GPS satellites at The Ohio State University (OSU) (Grejner-Brzezinska, 1995). This technique was later applied for LEO satellites in a kinematic application by the research group at OSU (currently called the Satellite Positioning and Inertial Navigation, SPIN Lab.), of which the author of this dissertation is also a member (Grejner-Brzezinska et al., 2002; Kwon et al., 2002 and 2003), and by others (Byun, 2003; Bock, 2003). It was also used for geodetic network adjustment (Eren, 1986 and 1987), baseline estimation of the ground stations with Kalman filtering (Remondi and Brown, 2000), an *a priori* solution for the double-differenced approach of LEO POD (Byun and Schutz, 2001), or LEO dynamic orbit determination (Bae, 2005b).

The most pronounced advantage of the triple-differencing technique is that the unknown phase ambiguities are entirely removed; thus, the size of the system of normal equations is significantly decreased while the solution quality is, under certain conditions, equivalent to the double-difference float solution, as proved by Schaffrin and Grafarend (1986). However, in triple-differencing, the measurement noise is amplified, and the observations are epoch-to-epoch correlated due to the differencing in time. In addition, potentially strong constraints coming from the fixed integer ambiguities are lost. This disadvantage should, however, be considered in the context of the relatively low level of success in the ambiguity resolution in the double-differencing mode that heavily depends on the data quality, continuity, observational geometry, as well as the level of ionospheric activity. The triple-differencing approach is fast, efficient and suitable for real-time applications, as shown already by the aforementioned OSU group (Grejner-Brzezinska et al., 2002; Kwon et al., 2002 and 2003); thus, it can facilitate efficient LEO orbit determination which further supports various applications of LEOs, such as weather forecasting and space weather monitoring/prediction based on the LEO occultation events.

Most of the LEO POD strategies use a predetermined set of ground stations for differential positioning of a LEO satellite. In this research, to further reinforce the LEO POD process, an algorithm for the determination of an optimal configuration of the ground stations is proposed, which uses geodetic techniques of network optimization. The geometric optimization of the network of ground stations used for LEO orbit determination was successfully implemented (Bae, 2005a) by the second order design (Schaffrin, 1985). This method was originally designed to maximize the geometric strength for point positioning, but it is shown here as applicable to baseline optimization for the improvement of the LEO orbit quality.

In this research, all three techniques, namely the kinematic, dynamic and reduced-dynamic approaches for LEO orbit determination, are implemented to support atmospheric profiling for GPS meteorology that requires the near real-time POD estimation. Since April 2002, CHAMP Ultra-rapid Science Orbit (USO) has been available at 3-hour intervals with a latency of 2 hours after the actual observation (König et al., 2002; Wickert et al., 2004), but it is not published with a comparable latency. The most efficient method developed here is demonstrated to produce a 26-hour solution in

just 2.5 hours. Here, the estimated orbit is comprehensively compared and analyzed using the same data set of the CHAMP satellite. The orbit quality is verified in three different ways, namely through the direct comparison with the orbit solutions from other analysis centers, through the internal consistency check for the overlapping arcs, and through the calculation of the Satellite Laser Ranging (SLR) residuals with respect to the orbit estimated in this study.

Chapter 2 describes the overview of the satellite positioning techniques. The modernization of GPS and the basic concept of GPS occultation as the primary application of the LEO orbit determination considered in this study are the main points of this chapter. In addition, the measurement models for GPS positioning, including the triple-differencing technique, are also presented.

Chapter 3 presents three main orbit determination techniques, namely the kinematic, dynamic and reduced-dynamic approaches. The procedures and modeling techniques are discussed in detail in this chapter.

Chapter 4 explains the theory of the network optimization and its application to the baseline configuration for the precise LEO orbit determination.

Chapter 5 discusses the results of the orbit solutions which are obtained by the three different methods described in Chapter 3. These results are analyzed in detail by direct comparison with other orbit solutions, checking the overlapping orbit solutions and computing SLR residuals.

Chapter 6 provides the summary and conclusions of this research and suggests some future research directions.

CHAPTER 2

OVERVIEW OF SATELLITE POSITIONING

2.1 GPS

2.1.1 Development of GPS

The Global Positioning System (GPS) is a satellite-based positioning and time transfer system operated by the US Department of Defense (DoD). Although it was originally developed to support military users, it became indispensable to the civilian users for their commercial as well as scientific purposes. The advantage of GPS is that the receivers can be placed on any kind of platform, such as an aircraft, a ship and even fast moving satellites, and most of the time more than 4 satellites are visible to the tracking receiver. The GPS satellites are orbiting in six different planes with an inclination of 55° at an altitude of 20,200 km, completing one revolution in just under 12 hours.

The accuracy of GPS is guaranteed by its highly precise satellite atomic clocks. Its long term frequency stability is about 10^{-13} to 10^{-14} per day (Hofmann-Wellenhof et al., 2004). Currently, the best cold atomic fountain clock (not adopted by GPS yet) provides the fractional frequency stability of approximately 10^{-16} for the time intervals of a few hours to a day. Two L-band carrier waves, L1 and L2, are derived from the fundamental frequency, namely:

$$\mathrm{L1} = 154 f_0 = 1575.42 \text{ MHz},$$
$$\mathrm{L2} = 120 f_0 = 1227.60 \text{ MHz},$$

where f_0 is the fundamental frequency of 10.23 MHz. Therefore, the wavelengths for L1 and L2 correspond to 19.0 cm and 24.4 cm, respectively. This dual frequency capability can be useful for the elimination of a frequency-dependent error, such as an ionospheric delay.

GPS time is an atomic time scale, coincident with UTC (Coordinated Universal Time) on January 6.0, 1980, which is the origin for the GPS time. The UTC is adjusted by the leap seconds to keep up with the UT1 (Universal Time corrected for polar motion) within 0.9 seconds. GPS time has 19 seconds of constant offset with respect to TAI (International Atomic Time). Since the total leap seconds as of January 1.0, 2006 equal to 33 seconds, the GPS time is currently 14 seconds ahead of UTC. In other words,

$TAI - UTC = 33\,\mathrm{s}$ since 01 January 2006;

thus:

$GPS = UTC + 14\,\mathrm{s}$ since 01 January 2006.

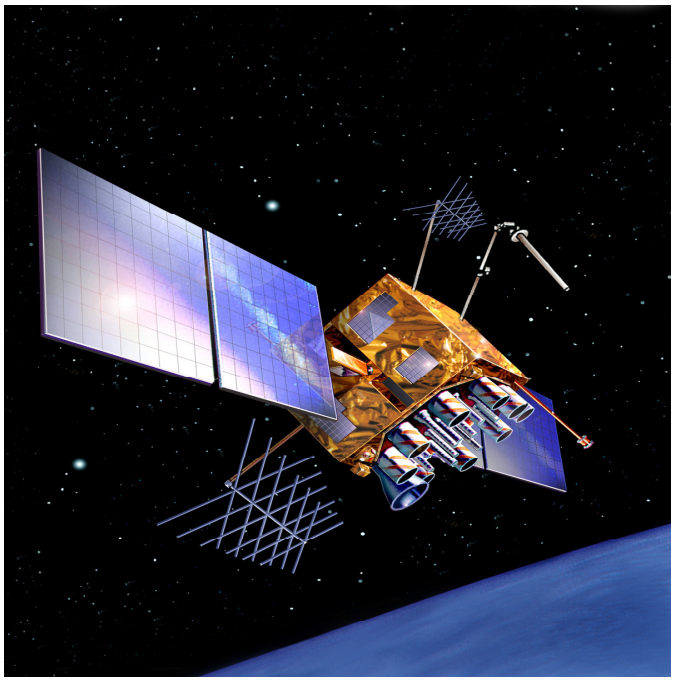

Figure 2.1 GPS Block IIR-M (http://www.lockheedmartin.com/data/assets/10674.jpg).

PRN	Block	Launch Date	Freq. Std.	Orbit Plane
01	IIA-16	22 NOV 1992	Cs	F6
02	IIR-13	06 NOV 2004	Rb	D1
03	IIA-25	28 MAR 1996	Cs	C2
04	IIA-23	26 OCT 1993	Rb	D4
05	IIA-22	30 AUG 1993	Rb	B4
06	IIA-24	10 MAR 1994	Rb	C1
07	IIA-20	13 MAY 1993	Rb	C5
08	IIA-28	06 NOV 1997	Cs	A3
09	IIA-21	26 JUN 1993	Rb	A1
10	IIA-26	16 JUL 1996	Cs	E3
11	IIR-3	07 OCT 1999	Rb	D2
13	IIR-2	23 JUL 1997	Rb	F3
14	IIR-6	10 NOV 2000	Rb	F1
15	II-9	01 OCT 1990	Cs	D5
16	IIR-8	29 JAN 2003	Rb	B1
17	IIR-M1	26 SEP 2005	Rb	C4
18	IIR-7	30 JAN 2001	Rb	E4
19	IIR-11	20 MAR 2004	Rb	C3
20	IIR-4	11 MAY 2000	Rb	E1
21	IIR-9	31 MAR 2003	Rb	D3
22	IIR-10	21 DEC 2003	Rb	E2
23	IIR-12	23 JUN 2004	Rb	F4
24	IIA-11	04 JUL 1991	Cs	D6
25	IIA-12	23 FEB 1992	Rb	A2
26	IIA-14	07 JUL 1992	Rb	F2
27	IIA-15	09 SEP 1992	Cs	A4
28	IIR-5	16 JUL 2000	Rb	B3
29	IIA-17	18 DEC 1992	Rb	F5
30	IIA-27	12 SEP 1996	Rb	B2

Table 2.1 Current (as of August 2006) GPS constellation (ftp://tycho.usno.navy.mil/pub/gps/gpsb2.txt).

The constellation of 29 Block II satellites (II/IIA/IIR/IIR-M) is currently operational, as of August 2006 (Table 2.1); PRN 17, launched on 26 September 2005, is the first modernized GPS satellite (IIR-M), broadcasting a second civil signal L2C (Figure 2.1).

2.1.2 GPS Modernization

While the demand for more precise GPS positioning increases, the current GPS has some weaknesses, such as, for example:

1) A civilian user who operates within the standard positioning system mode has an access only to the L1 C/A code; thus, no option for ionospheric delay correction with dual frequency is possible.
2) Because of the relatively weak signals of L1 and L2, it is difficult to perform positioning in confined environments.
3) GPS signals tend to be affected by multipath.

Therefore, it is necessary to extend the capabilities of GPS further to enhance not only military users but also civilian and/or commercial users with new GPS signals for improved accuracy, integrity and continuity of service. The most significant feature of this GPS modernization is the addition of two new navigation signals for civilian use as well as a new military code on both L1 and L2 frequencies. The new military signals have an increased power for faster signal acquisition and improved security codes. On the other hand, the civilian users have the benefit of a second frequency for ionospheric correction and redundancy, and a third signal for high accuracy and real-time applications.

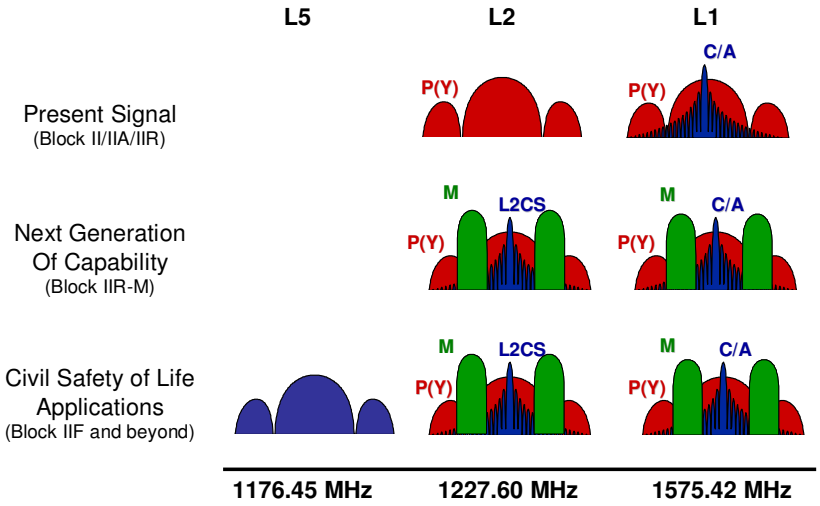

Figure 2.2 GPS signal evolution (Novak, 2001).

A new civil code, L2C, added to the existing GPS L2 frequency has a lower signal power than L1 C/A, and its chipping rate is limited to 1.023 MHz to ensure separation of the spectrum from the new military M code. Also L2C has an enhanced performance in that it divides the transmitted signals into two equal-power components, one with, and one without data. This improves the carrier tracking threshold performance by 3 dB and provides 'full-wavelength' carrier phase measurements, not requiring the phase ambiguity resolution needed for signals with bi-phase data modulation (Fontana et al., 2001). Therefore, L2C performs significantly better than the L1 C/A signal replica on L2. L2C has improved cross-correlation properties for single frequency applications such as for positioning in wooded areas or indoor navigation. The L2C capability was first turned on for Block IIR-M satellite (PRN 17) on 16 December 2005, and is currently under testing.

Another new signal introduced under the GPS modernization is a third civil signal L5. The L5 signal will be provided on GPS Block IIF satellites beginning in 2007 (as of May 2006 schedule), and all subsequent GPS satellites (Figure 2.2). Since L5 is not shared with military signals, it achieves the power split by using two equal-length codes in phase quadrature at 1176.45 MHz with a chip rate of 10.23 MHz. The addition of L5 will make GPS a more robust radio-navigation service for precision navigation, in support of high accuracy and real-time applications.

The next generation GPS III system is expected to have the increased security and accuracy as well as higher power signals for better anti-jamming. It will support all of the legacy signals (backward compatibility) and, additionally, there will be a fourth civil signal, L1C, which will be added to the GPS L1 frequency. This new signal is assured a 1.5 dB increase in minimum C/A code power to mitigate any noise floor increase, providing real-time unaugmented 1-meter accuracy. In addition, it will enable greater civil interoperability with the Galileo L1 signal. The first L1C signal will be available with the first GPS III satellite launch, which is expected in 2013 (as of May 2006 schedule). Great effort has been made to ensure it has robust, supportable, flexible, international capability for the next 30 years.

For further explanation of GPS modernization, one can refer to the following website http://www.navcen.uscg.gov/gps/modernization/default.htm.

2.1.3 GPS Products

The International GNSS Service (IGS) is committed to providing the highest quality of products as the standard for the Global Navigation Satellite Systems (GNSS) in support of Earth science research, multidisciplinary applications, and education (http://igscb.jpl.nasa. gov/).

Products		Accuracy	Latency	Updates	Sample Interval
Ultra-Rapid (predicted half)	orbits Sat. clocks	~ ±10 cm ~ ±5 ns	real-time	four times daily	15 min
Ultra-Rapid (observed half)	orbits Sat. clocks	< ±5 cm ~ ±0.2 ns	3 hours	four times daily	15 min
Rapid	orbits Sat. & Stn. clocks	< ±5 cm ±0.1 ns	17 hours	daily	15 min 5 min
Final	orbits Sat. & Stn. clocks	< ±5 cm < ±0.1 ns	~13 days	weekly	15 min 5 min

Table 2.2 GPS orbit products (http://igscb.jpl.nasa.gov/components/prods.html).

The IGS collects and distributes GPS observation data sets from stations all over the world. These data sets include GPS observations from the ground stations and from LEOs, GPS broadcast ephemerides, and other meteorological data with a latency of one hour to one day (and 4 days of latency in the case of LEO GPS observations). The GPS products are analyzed independently by the IGS analysis centers, and combined, constituting a single IGS product. For example, the orbit solutions from eight analysis centers are combined to produce the final GPS orbit solution. Table 2.2 shows the list of GPS orbit products and their accuracies.

More than 250 ground stations are routinely tracking GPS satellites, with the accuracy of the station coordinates of ±3 mm and ±6 mm in the horizontal and vertical directions, respectively. For the Earth rotation parameters, the final solution is accurate to ±0.05 mas for the polar motion and less than ±0.2 mas/day for the polar motion rates, with a latency of about 13 days. The Length of Day (LOD) which is equivalent to the variation in the rotational rate of the Earth, represented by the time derivative of the difference between Earth rotational time and dynamical time, is provided with an accuracy of ±0.02 ms in the final solution. The final tropospheric zenith delay can be obtained with ±4 mm of accuracy at 2-hour averaging intervals. Also the final ionospheric TEC (Total Electron Content) can be mapped every 2 hours with a resolution of 5 degrees (longitude) by 2.5 degrees (latitude), and an accuracy of ±(2-8) TECU (TEC unit, 10^{16} electrons per m^2 which amounts to 16 cm for L1). The latencies for the tropospheric zenith delay and ionospheric TEC are within 4 weeks and 11 days, respectively.

2.1.4 GPS Measurement Models

The GPS observations are ranges, deduced from the measured time of signal travel, or phase differences on the basis of a comparison between the received signals and receiver-generated signals (Hofmann-Wellenhof et al., 2004). The basic observations for GPS positioning are given by (excluding multipath terms)

$$P_{i,1}^k = \rho_i^k + \frac{I_i^k}{f_1^2} + T_i^k + c(dt_i - dt^k) + b_{i,2} + e_{i,1}^k, \tag{2.1}$$

$$P_{i,2}^k = \rho_i^k + \frac{I_i^k}{f_2^2} + T_i^k + c(dt_i - dt^k) + b_{i,3} + e_{i,2}^k, \tag{2.2}$$

$$\Phi_{i,1}^k = \rho_i^k - \frac{I_i^k}{f_1^2} + T_i^k + \lambda_1 N_{i,1}^k + c(dt_i - dt^k) + \lambda_1(\varphi_0^k - \varphi_{i0}) + \varepsilon_{i,1}^k, \tag{2.3}$$

$$\Phi_{i,2}^k = \rho_i^k - \frac{I_i^k}{f_2^2} + T_i^k + \lambda_2 N_{i,2}^k + c(dt_i - dt^k) + b_{i,1} + \lambda_2(\varphi_0^k - \varphi_{i0}) + \varepsilon_{i,2}^k, \tag{2.4}$$

with:

- P, Φ: the pseudo-range and phase measurement in distance units, respectively;
- ρ: the geometric range between the transmitter and the receiver at the time of signal emission and reception, respectively;
- f: the frequency of the carrier phase;
- I / f^2: the ionospheric refraction;
- T: the tropospheric refraction;
- λ: the wavelength of the signal;
- N: the integer ambiguity;
- c: the speed of light in vacuum;
- dt: the clock error;
- b: the interchannel bias;
- φ_0: the initial fractional phase;
- e, ε: the measurement noise for pseudo-range and phase, respectively.

Also, the superscript k represents the transmitter (GPS satellite) and the subscript i represents the receiver; the subscripted number 1 or 2 means that the term refers to the L1 or L2 signals, respectively (for all nomenclature except the interchannel biases). The interchannel bias represents the possible time delay between the measurements, which is expressed with respect to Φ_1; b_1 is the bias between Φ_1 and Φ_2; b_2 is between Φ_1 and P_1; b_3 is between Φ_1 and P_2. The full expression of the observation equations for

the pseudo-range as well as the phase measurement can be found in Grejner-Brzezinska (1995).

The double-differenced observations are often used for GPS positioning applications because most of the spatially correlated error sources are eliminated by differencing with respect to the simultaneously tracking receivers and satellites. The single-differenced observation can be obtained by differencing two one-way measurements from two receivers *i* and *j* to the common satellite *k*. The single-differenced observation, however, is still affected by the receiver clock error and the interchannel biases, and it is difficult to separate these interchannel biases from the ionospheric delay and the ambiguities (Grejner-Brzezinska, 1995). Thus, one can further difference two single-differenced observations to satellites *k* and *l*, resulting in the double-differenced observation in which the interchannel biases are removed.

$$P_{ij,1}^{kl} = \rho_{ij}^{kl} + T_{ij}^{kl} + \frac{I_{ij}^{kl}}{f_1^2} + e_{ij,1}^{kl}, \tag{2.5}$$

$$P_{ij,2}^{kl} = \rho_{ij}^{kl} + T_{ij}^{kl} + \frac{I_{ij}^{kl}}{f_2^2} + e_{ij,2}^{kl}, \tag{2.6}$$

$$\Phi_{ij,1}^{kl} = \rho_{ij}^{kl} + T_{ij}^{kl} - \frac{I_{ij}^{kl}}{f_1^2} + \lambda_1 N_{ij,1}^{kl} + \varepsilon_{ij,1}^{kl}, \tag{2.7}$$

$$\Phi_{ij,2}^{kl} = \rho_{ij}^{kl} + T_{ij}^{kl} - \frac{I_{ij}^{kl}}{f_2^2} + \lambda_2 N_{ij,2}^{kl} + \varepsilon_{ij,2}^{kl}. \tag{2.8}$$

While the double-difference observations can eliminate most of the nuisance parameters, it is still possible to get additional benefit by forming a linear combination of two carrier phase (or pseudo-range) observations with different frequencies. The most popular linear combination of carrier phase observations is the ionosphere-free combination which can be represented by

$$\begin{aligned} \Phi_{ij,ion-free}^{kl} &= \alpha_1 \Phi_{ij,1}^{kl} + \alpha_2 \Phi_{ij,2}^{kl} \\ &= \rho_{ij}^{kl} + T_{ij}^{kl} + \alpha_1 \lambda_1 N_{ij,1}^{kl} + \alpha_2 \lambda_2 N_{ij,2}^{kl} + \alpha_1 \varepsilon_{ij,1}^{kl} + \alpha_2 \varepsilon_{ij,2}^{kl}, \end{aligned} \tag{2.9}$$

where

$$\alpha_1 = \frac{f_1^2}{f_1^2 - f_2^2}, \quad \alpha_2 = -\frac{f_2^2}{f_1^2 - f_2^2} \tag{2.10}$$

and f_1 and f_2 are L1 and L2 frequencies, respectively. This ionosphere-free linear combination of phases can remove the influence of the ionospheric refraction, although there still remains a second-order effect. Contrary to the ionosphere-free linear combination, the ionosphere-only combination is useful for monitoring the behavior of the ionosphere or for cycle-slip detection. This combination can be obtained by differencing two phase ranges corresponding to two frequencies, that is, L1 and L2, thus, the geometric range term disappears, as can be seen in Eqs. (2.7) and (2.8) which give rise to Eq. (2.11):

$$\begin{aligned} \Phi_{ij,ion-only}^{kl} &= \Phi_{ij,1}^{kl} - \Phi_{ij,2}^{kl} \\ &= I_{ij}^{kl}\left(\frac{f_1^2 - f_2^2}{f_1^2 f_2^2}\right) + \lambda_1 N_{ij,1}^{kl} - \lambda_2 N_{ij,2}^{kl} + \varepsilon_{ij,1}^{kl} - \varepsilon_{ij,2}^{kl} . \end{aligned} \tag{2.11}$$

One thing that should be mentioned here is that the formulation of the differenced observations introduces correlations between the newly formed observations; thus, proper care should be taken of this correlation in the positioning algorithm. Since the differenced observations are considered as a multiplication of the differencing operator with the original observations, the law of error propagation must be applied to account for the correlation between the differenced observations.

2.1.5 Triple-Differencing Technique

It is true that most of the error sources are removed in the double-differenced GPS carrier phase observations, but there is still a challenge to resolve the integer ambiguities. As long as the integer ambiguities are fixed correctly, one can expect to have strong constraints for the positioning solution. In the real applications of the LEO orbit determination, however, since the baselines between the tracking stations and LEOs are normally very long (hundreds to thousands of kilometers), it is not easy to resolve the integer ambiguities due to the residual ionospheric effects (Byun and Schutz, 2001). The reported success rate of ambiguity resolution is at the level of about 40 %, based on fixing the wide-lane ambiguities, and about 18 % of the subsequent narrow-lane ambiguities (Švehla and Rothacher, 2003). In addition, the number of unknown ambiguities accounts for most of the unknown parameters in the dynamic POD using double-differenced observations.

In order to avoid the time-consuming and complicated ambiguity resolution process, the triple-differenced, ionosphere-free GPS carrier phase data are used as primary observations in this study. The triple-differencing technique for orbit determination of the

GPS satellites was first applied in a dynamic approach by Grejner-Brzezinska (1995), and to the LEO satellites in the kinematic application by Byun (1998 and 2003), Grejner-Brzezinska et al. (2001 and 2002), Kwon et al. (2002 and 2003), and by Bock (2003). In contrast, Eren (1986 and 1987) had used the triple-differenced observations for the geodetic network adjustment, and Byun and Schutz (2001) used them to get an *a priori* solution for the double-differenced approach. Also the triple-differenced carrier phase measurements were processed in a delayed-state Kalman filter for the baseline estimation of the ground stations (Remondi and Brown, 2000). It is well-known that the triple-differencing technique has the advantage of removing the unknown phase ambiguities; thus, the normal equations have a significantly reduced dimension. Schaffrin and Grafarend (1986) proved that, under certain range space conditions which can be easily fulfilled, the solution quality from the triple-differencing technique is equivalent to the double-difference float solution. Beside the removed nuisance parameters, the need to detect and correct the cycle slips is accommodated by removing data outliers during the estimation process using the residual cut-off (threshold) criterion.

The triple-differenced GPS carrier phase observations are given as follows (Grejner-Brzezinska, 1995):

$$\Phi_{ij,1,dt}^{kl} = \rho_{ij,dt}^{kl} + T_{ij,dt}^{kl} - \frac{I_{ij,dt}^{kl}}{f_1^2} + \varepsilon_{ij,1,dt}^{kl}, \tag{2.12}$$

$$\Phi_{ij,2,dt}^{kl} = \rho_{ij,dt}^{kl} + T_{ij,dt}^{kl} - \frac{I_{ij,dt}^{kl}}{f_2^2} + \varepsilon_{ij,2,dt}^{kl}, \tag{2.13}$$

where the notation follows the earlier explanation except for dt which now represents a difference between two consecutive double-differenced observations. In triple-differencing, however, the measurement noise is amplified, and the observations are further correlated on the epoch-by-epoch basis due to the differencing in time. In addition, the potentially strong constraints coming from the fixed integer ambiguities are lost. The correlation between consecutive epochs due to the time-differencing can be resolved by a simple and efficient algorithm, which decomposes the covariance matrix using the Cholesky factorization (Grejner-Brzezinska, 1995; Kwon, 1997; Byun, 1998; Kwon et al., 2003).

Assuming that the covariance matrix for all epochs of the triple-differenced observations is represented by

$$\Sigma_{all} = \begin{bmatrix} \Sigma_{11} & \Sigma_{12} & 0 & \cdots & \cdots & 0 \\ \Sigma_{21} & \Sigma_{22} & \Sigma_{23} & 0 & \cdots & \vdots \\ 0 & \Sigma_{32} & \Sigma_{33} & \Sigma_{34} & 0 & \vdots \\ \vdots & 0 & \ddots & \ddots & \ddots & 0 \\ \vdots & \cdots & 0 & \Sigma_{n-1,n-2} & \Sigma_{n-1,n-1} & \Sigma_{n-1,n} \\ 0 & \cdots & \cdots & 0 & \Sigma_{n,n-1} & \Sigma_{nn} \end{bmatrix}, \tag{2.14}$$

the algorithm for the recursive decorrelation of the covariance matrix can be summarized as follows:

1) Cholesky decomposition of the covariance matrix of the first epoch:
$\Sigma = \Sigma_{11} = L_{11} L_{11}^T$

2) Forward substitution to get the whitened design matrix $\overline{A}_1$, and observation vector $\overline{y}_1$ for epoch 1:
$L_{11}\left[\overline{A}_1 \quad \overline{y}_1\right] = \left[A_1 \quad y_1\right]$

3) Store the decomposed matrix, the whitened design matrix and observation vector
$L_{ii} \leftarrow L_{11}, \quad \overline{A}_i \leftarrow \overline{A}_1, \quad \overline{y}_i \leftarrow \overline{y}_1$

for any $i \in \{1, \cdots, n-1\}$

4) Read the design matrix, observation vector, covariance matrix for epoch $i+1$ as well as the cross-correlation matrix between epoch i and $i+1$:
$A_{i+1}, \; y_{i+1}, \; \Sigma_{i+1,i}, \; \Sigma_{i+1,i+1}$

5) Cholesky decomposition of the covariance matrix for two consecutive epochs (decomposition is to be done only for the lower two blocks):

$$\Sigma = \begin{bmatrix} L_{ii} L_{ii}^T & \Sigma_{i,i+1} \\ \Sigma_{i+1,i} & \Sigma_{i+1,i+1} \end{bmatrix} = \begin{bmatrix} L_{ii} & 0 \\ L_{i+1,i} & L_{i+1,i+1} \end{bmatrix} \begin{bmatrix} L_{ii} & 0 \\ L_{i+1,i} & L_{i+1,i+1} \end{bmatrix}^T$$

6) Forward substitution to get $\overline{A}_{i+1}, \overline{y}_{i+1}$ from:

$$L_{i+1,i+1}\left[\overline{A}_{i+1} \quad \overline{y}_{i+1}\right] = \left[A_{i+1} \quad y_{i+1}\right] - L_{i+1,i}\left[\overline{A}_i \quad \overline{y}_i\right]$$

7) Replace the Cholesky factor L_{ii} and the whitened $\overline{A}_i, \; \overline{y}_i$ by

$L_{i+1,i+1}, \; \overline{A}_{i+1}$, and $\overline{y}_{i+1}$.

8) Repeat steps 4) through 7) until the process is completed ($i+1=n$).

2.2 CHAMP

2.2.1 System Description

The German scientific satellite, CHAMP (CHAllenging Minisatellite Payload), was launched on July 15, 2000, into an almost circular, near-polar (i = 87°) orbit with an initial altitude of 454 km, completing one revolution period in 93.55 minutes. Due to the atmospheric drag, the altitude has decreased over the six-year mission. The primary science objectives of the mission are (http://www.gfz-potsdam.de/pb1/op/champ/index_CHAMP.html)

1) To provide highly precise global long-wavelength features of the static Earth gravity field and the temporal variations of this field;
2) To provide, with unprecedented accuracy, global estimates of the main and crustal magnetic field of the Earth and the space/time variability of these field components;
3) To provide a good global distribution of a large number of GPS signal refraction data caused by the atmosphere and ionosphere at the event of satellite occultation by the Earth atmosphere, which can be converted into temperature, water vapor and electron content profiles.

The atmospheric science objective mandates the availability of CHAMP orbits in near real-time, to enable the use of the occultation data in numerical weather modeling and forecasting.

The nominal attitude of the CHAMP satellite can be represented by the spacecraft's body-fixed system which has an origin at the center of mass of the spacecraft. Each component of the body-fixed system is described in Table 2.3 (CHAMP, 2002).

Axis	Description
$x_{S/C}$	aligned with the long side of the spacecraft towards the boom, in nominal attitude in flight direction (roll axis);
$y_{S/C}$	completing the triad (pitch axis);
$z_{S/C}$	nadir-looking, positive downward (yaw axis).

Table 2.3 The spacecraft's body-fixed system.

In order to meet the science mission objectives, CHAMP carries many instruments onboard, including a STAR accelerometer, TRSR-2 GPS receivers, a Laser Retro-Reflector and an Advanced Stellar Compass (CHAMP, 2005). The STAR accelerometer sensor is designed to measure all non-gravitational accelerations, such as atmospheric drag and solar radiation pressure, acting on the CHAMP satellite. The resolution of the linear acceleration is $3\times10^{-8} m/s^2$ for the x-axis and $3\times10^{-9} m/s^2$ for the y- and z-axis in the instrument-fixed frame of the accelerometer. The accelerometer-instrument-fixed frame is parallel to the spacecraft-body-fixed frame, but pointing in different directions, which is explained in CHAMP (2002). It should be mentioned here that, although the onboard accelerometer of CHAMP can measure all nonconservative forces in three directions (Kang et al., 2003), the total replacement of the nonconservative forces with the accelerometer data is not possible. This follows from the fact that the published accelerometer data are smoothed over the 10-second intervals, during which there still could be more dynamics or maneuvers (Boomkamp, 2004).

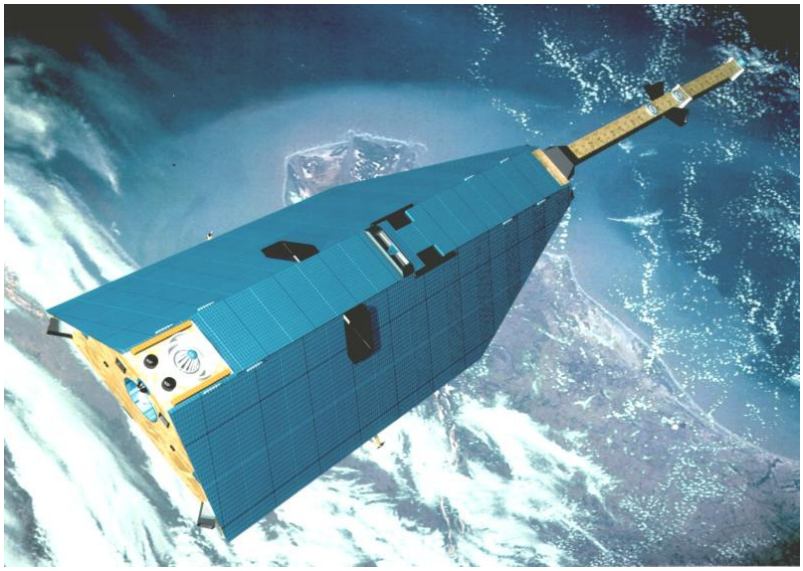

Figure 2.3 The CHAMP satellite. © Astrium

The CHAMP "BlackJack" GPS receiver, manufactured at NASA's Jet Propulsion Laboratory (JPL), serves as the main tool for high-precision orbit determination of the satellite. It has 16 channels and can track a maximum of 12 satellites simultaneously for POD with a sampling interval of 10 seconds. In the occultation mode the receiver can track up to four GPS satellites at 1/50 s sampling interval, which is much faster than that used for POD. The Laser Retro-Reflector (LRR) consists of four corner-cube prisms in an array which reflects short laser pulses back to a transmitting ground station. The measurements reflected by the LRR, a technique known as Satellite Laser Ranging (SLR), can be used to validate the GPS-based CHAMP orbit accuracy. The offset of the LRR with respect to the center of mass of the spacecraft is 250 mm in the positive z-axis of the

spacecraft-body-fixed frame. The Advanced Stellar Compass (ASC) provides high-precision attitude information for the instrument fixed to the spacecraft body. Another ACS is part of the magnetometry optical bench unit on the boom. Also, ASCs are used as sensors for the satellite attitude control system. The precision of the attitude determination by the ACS is considered as $\pm\frac{4}{3}$ arcsec.

2.2.2 The Principle of GPS Occultation

With the successful demonstration of GPS/Meteorology (GPS/MET) (König et al., 2002; GPS/MET, 2006), GPS radio-occultation is considered a valuable data source for numerical weather prediction and climate change studies. One of the important objectives of CHAMP is to provide atmospheric profiling with high vertical resolution, high accuracy, and global coverage in all weather. The GPS radio-occultation technique is based on precise dual-frequency phase measurements of a GPS receiver (http://www.gfz-potsdam.de/champ/science/limb_SCIENCE.html). The GPS occultation occurs when a LEO is tracking a setting or rising GPS satellite behind the Earth's atmospheric limb, which typically lasts about 1 minute. The excess phase path delay due to the atmosphere can become up to a few kilometers near the surface (Syndergaard, 2005). The derived excess phase for the occulting satellites can be converted to the bending angles (maximum of up to 2°). This bending angle is used to determine vertical profiles of the refractive index with the assumption of a spherically-symmetric atmosphere, and further converted to water vapor within the lower troposphere if adequate pressure and temperature data are available (Rocken et al., 1995). The vertical profiles of electron density can also be derived based on similar principles. The atmospheric profiles have to be made available within three hours in order to support weather predictions (König et al., 2002). Both CHAMP and GPS satellite orbits (position and velocity) should be known accurately and continuously to compute the GPS measurement path delay; thus, the precise orbit of CHAMP should be available within two hours. However, the CHAMP orbit is not currently published with a comparable latency, as mentioned in Chapter 1.

Figure 2.4 shows the concept of GPS radio-occultation in which double-differenced observations are assumed. The atmospheric profiling experiment onboard CHAMP began on February 11, 2001 (Wickert et al., 2004). Although CHAMP is used for GPS radio-occultation observation, it cannot provide temporally and spatially dense occultation measurements with global coverage. The recently launched COSMIC (Constellation Observing System for Meteorology, Ionosphere & Climate) satellites (COSMIC, 2006), on the other hand, will significantly increase the radio-occultation measurements on a global basis. Thus, it is expected to contribute to the scientific research on climate, especially providing a global self-calibrating data set for climate monitoring and model testing, and monitoring of the water vapor distribution (Anthes et al., 2000). Figure 2.5 shows the simulated radio-occultation measurements of COSMIC for 24 hours of an operational constellation which has 6 satellites orbiting in six different planes.

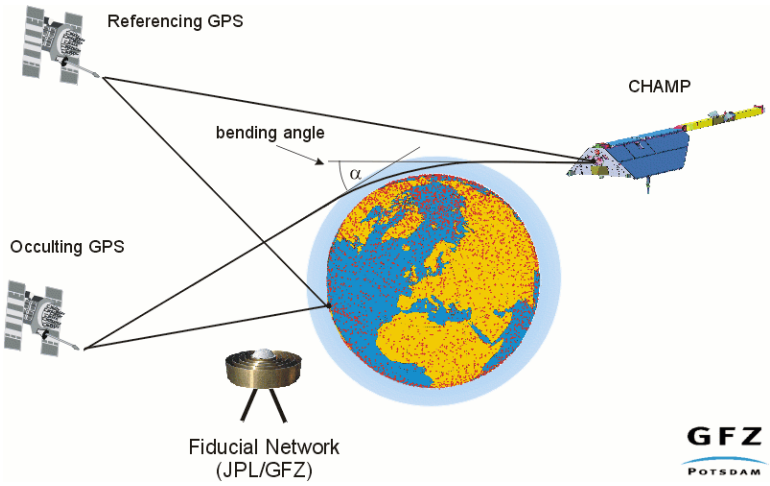

Figure 2.4 Double-difference geometry of GPS limb sounding with CHAMP (http://www.gfz-potsdam.de/champ/science/limb_SCIENCE.html).

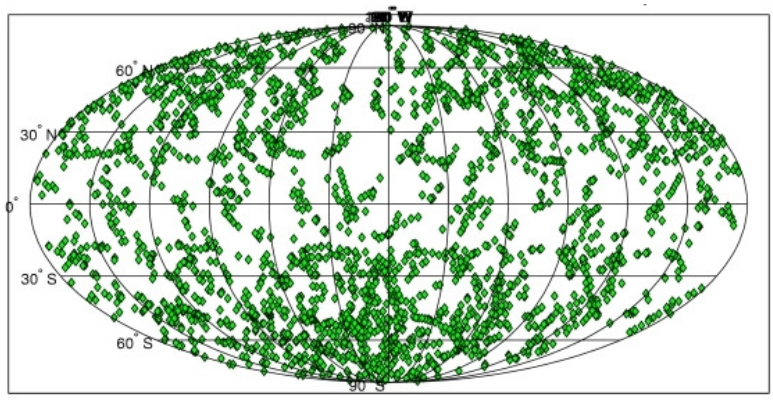

Figure 2.5 Sun-fixed occultation locations for COSMIC (6 spacecrafts, 24 hours) - simulated by Bill Schreiner (UCAR).

CHAPTER 3

ORBIT DETERMINATION TECHNIQUES

Orbit determination is a process of improving the *a priori* orbital elements by using a large set of tracking data (Montenbruck and Gill, 2001). Three different techniques that are widely used for precise orbit determination will be described in this chapter, namely, kinematic, dynamic, and reduced-dynamic approaches. As can be seen in Table 3.1, the dynamic models are still predominantly used in the CHAMP orbit comparison campaign. Notably, the adopted approach varies depending on the purpose of the application as well as on the characteristics of the target satellite.

Analysis Center	Kinematic	Reduced-Dynamic	Dynamic	Mixed
CSR			✓	
TUM		✓		
GFZ			✓	
GRGS		✓		
NCL				✓
DEOS			✓	
JPL				✓
AIUB		✓		
CNES		✓		
ESA	✓			
UNB	✓			
UCAR	✓			✓

Table 3.1 Orbit determination techniques used for the CHAMP orbit comparison campaign (Boomkamp, 2003).

3.1 Adjustment Theory

Generally the orbit determination problem is characterized by nonlinear relations between the observations and the describing parameters. Thus, it is necessary to linearize the measurement equations with respect to the nominal reference orbit (which is reasonably close to the true trajectory) to benefit from linear estimation theory.

Assuming the increments (meaning the differences from the *a priori* orbits) in the linearized system to be small enough, the weighted least-squares adjustment technique can be used. The solution, called the LEast-Squares Solution (LESS), provides estimates of the unknown parameter increments by minimizing the weighted sum of squared deviations or inconsistencies. The linearized Gauss-Markov model is generally represented by

$$y = A\xi + e, \quad e \sim \mathcal{N}(0, \sigma_0^2 P^{-1}), \tag{3.1}$$

where y is an $n\times 1$ random vector of measurement increments, A is an $n\times m$ design matrix of rank $q \le m$, ξ is an $m\times 1$ non-random (incremental) parameter vector, e is an $n\times 1$ random error vector with zero mean and cofactor matrix of P^{-1}. The variance component, σ_0^2, which may or may not be known, can usually be determined in the estimation process. Once the *a priori* information of the parameters is available, it is often used in form of stochastic constraints to this model as follows:

$$z_0 = K\xi + e_0, \quad e_0 \sim \mathcal{N}(0, \sigma_0^2 P_0^{-1}), \tag{3.2}$$

where z_0 is an $l\times 1$ vector of constraints, K is an $l\times m$ matrix of known coefficients, and e_0 is an error vector for the constraints with the (suitably scaled) weight matrix, P_0. In addition, the constraints are usually assumed to satisfy the conditions of

$$C\{e, e_0\} = 0, \tag{3.3}$$

$$rk\begin{bmatrix} A \\ K \end{bmatrix} = m. \tag{3.4}$$

The weighted LESS within the Gauss-Markov model with stochastic constraints can be obtained by minimizing the Lagrange target function

$$J = e^T Pe + e_0^T P_0 e_0 + 2\lambda^T (y - A\xi - e) + 2\nu^T (z_0 - K\xi - e_0), \tag{3.5}$$

where λ and ν are vectors of Lagrange multipliers. The solution within the Gauss-Markov model with stochastic constraints is given by

$$\hat{\xi} = \left(N + K^T P_0 K\right)^{-1} \left(c + K^T P_0\, z_0\right), \tag{3.6}$$

where

$$N = A^T PA, \quad c = A^T Py. \tag{3.7}$$

The dispersion matrix of the estimates is represented by

$$D\{\hat{\xi}\} = \sigma_0^2 \left(N + K^T P_0 K\right)^{-1}, \tag{3.8}$$

and the optimal unbiased estimate of the variance component can be computed as

$$\hat{\sigma}_0^2 = \frac{y^T P y + z_0^T P_0\, z_0 - \hat{\xi}^T (c + K^T P_0\, z_0)}{n - m + l}. \tag{3.9}$$

The detailed derivation of the solution is given by Schaffrin (2002). For an alternative approach, based on a generalized Lagrange target function, see Schaffrin (1995).

3.1.1 Batch Filtering

In case of the dynamic POD approach, the batch filter uses all data in the arc to estimate the unknown ("state") parameters at the certain epoch. It is not necessarily the first epoch, but, for convenience, the first epoch is assumed hereafter. Therefore, all the measurements should be mapped backwards to the first epoch and processed simultaneously to obtain an estimate of the state vector at that epoch. State estimates at future times are obtained by propagating the estimated epoch state forward using the satellite equations of motion. Since the batch filter fits the state vector epoch-wise to the entire data span, it is susceptible to dynamic model errors and the assumption of constant measurement biases.

In the general orbit determination problem, the measurements have a nonlinear relation to the unknown state vector:

$$\boldsymbol{Y}_k = G(\boldsymbol{X}_k, t_k) + \boldsymbol{v}_k, \quad \boldsymbol{v}_k \sim \mathcal{N}(0, \sigma_0^2 R_k), \tag{3.10}$$

where $\boldsymbol{Y}_k$ and $\boldsymbol{X}_k$ are the observation vector and the unknown state vector at time, t_k, respectively, and with the observation error, $\boldsymbol{v}_k$, that has zero bias and cofactor matrix R_k. Once the reference trajectory, which is supposed to be reasonably close to the true trajectory, is available, the nonlinear observation equations can be linearized using a Taylor's series expansion. Let $\boldsymbol{X}_k^*$ be the reference trajectory (or reference state vector), serving as the Taylor's series approximation point. Then the observation equations can be linearized as follows:

$$\begin{aligned} \boldsymbol{Y}_k &= G(\boldsymbol{X}_k, t_k) + \boldsymbol{v}_k \\ &= G(\boldsymbol{X}_k^*, t_k) + \left[\frac{\partial G}{\partial \boldsymbol{X}^T}\right]_{\boldsymbol{X}_k^*} \left(\boldsymbol{X}_k - \boldsymbol{X}_k^*\right) + \boldsymbol{v}_k \ , \end{aligned} \tag{3.11}$$

where higher order terms are neglected. This can be abbreviated further to yield the form of Eq. (3.1), provided that the reference orbit is considered to be nonrandom:

$$\boldsymbol{y}_k = H_k \boldsymbol{x}_k + \boldsymbol{v}_k, \tag{3.12}$$

where the following substitution of terms is made:

$$\begin{aligned} \boldsymbol{y}_k &= \boldsymbol{Y}_k - G(\boldsymbol{X}_k^*, t_k) \ , \\ H_k &= \left[\frac{\partial G}{\partial \boldsymbol{X}^T}\right]_{\boldsymbol{X}_k^*} \ , \\ \boldsymbol{x}_k &= \boldsymbol{X}_k - \boldsymbol{X}_k^* \ . \end{aligned} \tag{3.13}$$

In order to estimate the state vector at the reference epoch, say t_0, the design matrix should be mapped to the reference epoch. Hence,

$$\begin{aligned} \boldsymbol{y}_k &= H_k \boldsymbol{x}_k + \boldsymbol{v}_k \\ &= H_k \Phi(t_k, t_0) \boldsymbol{x}_0 + \boldsymbol{v}_k \ , \end{aligned} \tag{3.14}$$

where $\Phi(t_k, t_0)$ denotes the state transition matrix from t_0 to t_k. Thus, all the measurements are expressed in terms of the state vector at the reference epoch ($\boldsymbol{x}_0 = \xi$) where the least-squares adjustment solution, as given by Eq. (3.6), can be used in the

event that the stochastic constraints, Eq. (3.2), for the reference epoch are available. The state transition matrix $\Phi(t_k, t_0)$ in Eq. (3.14) can be obtained by integrating the dynamic equations numerically. Details of which follow in the next section.

In contrast, since there is no dynamic model involved in the kinematic approach, the state vectors at different epochs cannot be connected by the state transition matrix. Therefore, the state vector of each epoch becomes part of the unknown parameter vector which then should be estimated in the adjustment. In this case the observation model follows the first form of Eq. (3.14).

3.1.2 Wave Filter

The estimated orbit error resulting from the dynamic approach generally shows an error behavior of wave-like structure, notably it can be represented by different shapes of waves depending on the size of the segment. Since the statistical representation of the process noise requires an average over a substantial length of arc, it might be advantageous to model the process noise instead as a wave process. The wave process replaces the process noise as a linear combination of known basis functions with unknown coefficients (Salychev and Schaffrin, 1992; Salychev, 1998). The coefficients used for the wave algorithm are assumed to be piecewise constant.

A wave process can be expressed by (Salychev, 1998, p. 144)

$$w(t) = c_1 f_1(t) + c_2 f_2(t) + \cdots + c_n f_n(t) \tag{3.15}$$

with

$f_1(t), f_2(t), \cdots, f_n(t)$: the chosen basis functions;

$c_1, c_2, \cdots, c_n$: the unknown coefficients which vary from one instant to the next.

The basis functions used in Eq. (3.15) can be piecewise constant, linear or exponential functions. The choice of the basis functions should be determined from an analysis of the process noise before they are introduced into the system description. In the orbit determination problem, the orbit error expresses periodic behavior at different frequencies; thus, it may be best to describe its orbit error as a linear wave function.

The basic idea of the wave filter is that the entire arc is divided into sub-arcs called "cycles," and each estimation cycle should be chosen to ensure the convergence of the state vector. The estimates after each cycle are propagated to the following epochs to represent the total state vector behavior. Although the length of one cycle can be different from another, it would be convenient to deal with equal cycle lengths in the absence of knowledge of their behavior. Instead of estimating the unknown coefficients as given in

Eq. (3.15), Dirac functions with unknown intensity can be introduced as well, resulting in zero initial conditions. This means that an unknown intensity vector of Dirac functions can be added to the state equation, leading to

$$\dot{\boldsymbol{x}}(t) = A(t)\boldsymbol{x}(t) + \boldsymbol{n}\,, \tag{3.16}$$

where $\boldsymbol{n}$ is the Dirac impulse function vector with unknown intensities. Again Eq. (3.16) can be discretized to give:

$$\boldsymbol{x}_{k+1} = \Phi(t_{k+1}, t_k)\boldsymbol{x}_k + \boldsymbol{n}_k\,. \tag{3.17}$$

Assuming that the nonzero impulse appears once every cycle, the process noise modeling takes the form of an impulse sequence. Therefore, the impulse vector is only applied to the first epoch of each cycle and propagated as time proceeds.

The state vector along with the measurement vectors within the cycle can be represented by

$$\begin{bmatrix} \boldsymbol{y}_1 \\ \boldsymbol{y}_2 \\ \vdots \\ \boldsymbol{y}_k \\ \phi_0\tilde{\boldsymbol{x}}_0 \end{bmatrix} = \begin{bmatrix} H_1 \\ H_2\phi_1 \\ \vdots \\ H_k\phi_{k-1}\cdots\phi_1 \\ I_m \end{bmatrix} \boldsymbol{x}_1 - \begin{bmatrix} 0 \\ 0 \\ \vdots \\ 0 \\ I_m \end{bmatrix} \boldsymbol{n}_0 + \begin{bmatrix} \boldsymbol{v}_1 \\ \boldsymbol{v}_2 \\ \vdots \\ \boldsymbol{v}_k \\ \phi_0\boldsymbol{v}_0^0 \end{bmatrix}, \tag{3.18}$$

$$D\{\boldsymbol{v}_0^0\} = \Sigma_0^0\,, \tag{3.19}$$

where ϕ_k denotes the state transition matrix from t_k to t_{k+1}, *i.e.*, $\phi_k = \Phi(t_{k+1}, t_k)$, and $\tilde{\boldsymbol{x}}_0$ and Σ_0^0 are the state vector of *a priori* values of the estimate and its corresponding mean square error matrix at the initial epoch, respectively. It should be mentioned that Eqs. (3.18) and (3.19) represent a model for one cycle, and this can be repeated for each cycle.

For the near real-time processing of the wave algorithm, Eq. (3.18) can be expressed with the zero initial condition of the state vector ($\tilde{\boldsymbol{x}}_0 = 0$, random zero), as mentioned earlier. Thus, the model of Eq. (3.18) can be rephrased as

$$\boldsymbol{x}_1 = \phi_0\tilde{\boldsymbol{x}}_0 + \boldsymbol{n}_0 - \phi_0\boldsymbol{v}_0^0 = \boldsymbol{n}_0 - \phi_0\boldsymbol{v}_0^0\,, \tag{3.20}$$

$$\begin{aligned} \boldsymbol{y}_k &= H_k \boldsymbol{\phi}_{k-1} \cdots \boldsymbol{\phi}_1 \boldsymbol{n}_0 - H_k \boldsymbol{\phi}_{k-1} \cdots \boldsymbol{\phi}_1 \boldsymbol{\phi}_0 \boldsymbol{v}_0^0 + \boldsymbol{v}_k \\ &= H_k \boldsymbol{x}_k + \boldsymbol{v}_k \,. \end{aligned} \tag{3.21}$$

Therefore, a recursive filter form can be represented, until the next impulse, as

$$\hat{\boldsymbol{x}}_k^{(j)-} = \Phi(t_k, t_{k-1}) \hat{\boldsymbol{x}}_{k-1}^{(j)}, \tag{3.22}$$

$$P_k^{(j)-} = \Phi(t_k, t_{k-1}) P_{k-1}^{(j)} \Phi^T(t_k, t_{k-1}), \tag{3.23}$$

$$\hat{\boldsymbol{x}}_k^{(j)} = \hat{\boldsymbol{x}}_k^{(j)-} + K_k \left(\boldsymbol{y}_k - H_k \hat{\boldsymbol{x}}_k^{(j)-} \right), \tag{3.24}$$

$$P_k^{(j)} = (I - K_k H_k) P_k^{(j)-}, \tag{3.25}$$

where the superscript $^{(j)}$ represents the cycle *j*, and the proper gain matrix is given by

$$K_k = P_k^{(j)-} H_k^T \left(H_k P_k^{(j)-} H_k^T + R_k \right)^{-1}. \tag{3.26}$$

It should be mentioned here that although the initial values of the state vector can be obtained from the estimates of the previous cycle, they are assumed to have a randomness; therefore, its mean square error matrix should be reinitialized with the nominal values at the first epoch of each cycle, namely,

$$P_0^{(j)} = P_N^{(j-1)} + D\{\boldsymbol{v}_0^0\}, \tag{3.27}$$

where N denotes the length of the cycle.

Once the terminal state vector at each cycle is estimated, the smoothing procedure should be performed backward in time in order to re-estimate the state vector, $\boldsymbol{x}_k$, based on all measurements in the cycle:

$$\hat{\boldsymbol{x}}_k^N = \Phi(t_k, t_{k+1}) \hat{\boldsymbol{x}}_{k+1}^N \tag{3.28}$$

because there is no process noise within the cycle, as can be taken from Eqs. (3.17) and (3.18). It should be noticed that the superscript $^{(j)}$ denoting the cycle is omitted in

Eq. (3.28) for convenience.

3.1.3 Sequential Filtering

Contrary to batch filtering, sequential filtering, assumed to be of Kalman type in this study, updates the estimates at subsequent measurement epochs. Kalman sequential filtering (hereafter, Kalman filtering), was originally developed for real-time applications such as navigation, and has also been applied to GPS orbit determination (Chadwell, 1995). It can be considered as two step procedure; the first being the *time update* which predicts the state vector at a subsequent time using the system dynamics model, followed by the *measurement update* that estimates the state vector at the current time based on the measurements and the prior information from the first step.

It is worth noting that, in this context, the state vector has random character. Let the linear dynamics of the system at discrete time, t_k, be modeled by (Brown and Hwang, 1997)

$$\boldsymbol{x}_k = \Phi(t_k, t_{k-1})\boldsymbol{x}_{k-1} + \boldsymbol{w}_k \,, \quad \boldsymbol{w}_k \sim \mathcal{N}(0, \sigma_0^2 Q_k) \,, \tag{3.29}$$

with:

$\boldsymbol{x}_k$: the $m \times 1$ random state vector at t_k;

$\Phi(t_k, t_{k-1})$: the $m \times m$ state transition matrix, assumed to be constant over the time interval $\Delta t = t_k - t_{k-1}$;

$\boldsymbol{w}_k$: the $m \times 1$ Gaussian, zero-mean, white noise process vector with the cofactor matrix of Q_k.

Let $\hat{\boldsymbol{x}}_k^-$ and $\hat{\boldsymbol{x}}_k$ be the estimates of the state vector before and after the inclusion of the measurement at time t_k, respectively. Then, Kalman filtering can be explained in a Dynamic Linear Model which is composed of the observation equation, Eq. (3.12), and the state equation, Eq. (3.29), along with the initial condition equation of

$$\hat{\boldsymbol{x}}_{k-1} = \boldsymbol{x}_{k-1} + \boldsymbol{v}_{k-1}^0 \,, \quad \boldsymbol{v}_{k-1}^0 \sim \mathcal{N}(0, \sigma_0^2 P_{k-1}) \,, \tag{3.30}$$

where P_{k-1} denotes the cofactor matrix of the error for $\hat{\boldsymbol{x}}_{k-1}$, and the superscript ^{0} indicates the initial condition.

It is generally assumed that there are no correlations between the equations of the

Dynamic Linear Model; this means:

$$C\{\boldsymbol{v}_k, \boldsymbol{w}_k\} = 0, \quad C\{\boldsymbol{v}_k, \boldsymbol{v}_{k-1}^0\} = 0, \quad C\{\boldsymbol{w}_k, \boldsymbol{v}_{k-1}^0\} = 0 \quad \text{for all } k, \tag{3.31}$$

and no correlation is assumed between epochs:

$$C\{\boldsymbol{w}_k, \boldsymbol{w}_j\} = 0, \quad C\{\boldsymbol{v}_k, \boldsymbol{v}_j\} = 0 \quad \text{for } j \neq k. \tag{3.32}$$

Note that, strictly speaking, the matrix H_k in Eq. (3.13) would here be random which is, however, neglected in the following. It should also be mentioned that there is no redundancy in the state equation and the initial condition equation; therefore, all the redundancy comes from the observation equation.

In order to estimate the state vector at t_k, the Dynamic Linear Model can be solved by the least-squares adjustment. Combining Eqs. (3.29) and (3.30) produces the following equation (neglecting the time identifiers on the state transition matrix, for convenience):

$$\begin{aligned} \hat{\boldsymbol{x}}_k^- &= \Phi\, \hat{\boldsymbol{x}}_{k-1} \\ &= \boldsymbol{x}_k - \left(\boldsymbol{w}_k - \Phi\, \boldsymbol{v}_{k-1}^0\right). \end{aligned} \tag{3.33}$$

The first equality of Eq. (3.33) comes from the fact that the best estimates at time t_k without the measurements can be represented by taking the conditionally expected value of the state vector which is propagated from the given state vector, $\hat{\boldsymbol{x}}_{k-1}$, at the previous time based on the linear dynamics model as taken from Eq. (3.29):

$$\begin{aligned} \hat{\boldsymbol{x}}_k^- &= E\{\boldsymbol{x}_k \,|\, \hat{\boldsymbol{x}}_{k-1}\} \\ &= \Phi(t_k, t_{k-1}) E\{\boldsymbol{x}_{k-1} \,|\, \hat{\boldsymbol{x}}_{k-1}\} + E\{\boldsymbol{w}_k\} \\ &= \Phi(t_k, t_{k-1}) \hat{\boldsymbol{x}}_{k-1}, \end{aligned} \tag{3.34}$$

where the conditionally expected value of the state vector at time t_{k-1} is the best estimate at that epoch with the measurement update, $\hat{\boldsymbol{x}}_{k-1}$, itself and the noise process was assumed to have a zero-mean.

From Eqs. (3.12) and (3.33), the model turns into a condition equation as follows:

$$\begin{aligned} \boldsymbol{y}_k - H_k \hat{\boldsymbol{x}}_k^- &= \boldsymbol{v}_k + H_k \left(\boldsymbol{w}_k - \Phi \boldsymbol{v}_{k-1}^0 \right) \\ &= \begin{bmatrix} I & H_k & -H_k \Phi \end{bmatrix} \begin{bmatrix} \boldsymbol{v}_k \\ \boldsymbol{w}_k \\ \boldsymbol{v}_{k-1}^0 \end{bmatrix}. \end{aligned} \tag{3.35}$$

The least-squares solution of Eq. (3.35) can be expressed by (Schaffrin, 2002)

$$\begin{bmatrix} \tilde{\boldsymbol{v}}_k \\ \tilde{\boldsymbol{w}}_k \\ \tilde{\boldsymbol{v}}_{k-1}^0 \end{bmatrix} = \begin{bmatrix} R_k \\ Q_k H_k^T \\ -P_{k-1} \Phi^T H_k^T \end{bmatrix} \left[R_k + H_k \left(Q_k + \Phi P_{k-1} \Phi^T \right) H_k^T \right]^{-1} \left(\boldsymbol{y}_k - H_k \hat{\boldsymbol{x}}_k^- \right). \tag{3.36}$$

Therefore, the estimated state vector with measurement update at t_k can be obtained from Eqs. (3.33) and (3.36), resulting in the following equation:

$$\begin{aligned} \hat{\boldsymbol{x}}_k &= \hat{\boldsymbol{x}}_k^- + \left(\tilde{\boldsymbol{w}}_k - \Phi \tilde{\boldsymbol{v}}_{k-1}^0 \right) \\ &= \hat{\boldsymbol{x}}_k^- + \left(Q_k + \Phi P_{k-1} \Phi^T \right) H_k^T \left[R_k + H_k \left(Q_k + \Phi P_{k-1} \Phi^T \right) H_k^T \right]^{-1} \left(\boldsymbol{y}_k - H_k \hat{\boldsymbol{x}}_k^- \right) \\ &= \hat{\boldsymbol{x}}_k^- + K_k \left(\boldsymbol{y}_k - H_k \hat{\boldsymbol{x}}_k^- \right), \end{aligned} \tag{3.37}$$

where the so-called Kalman gain matrix is given by

$$K_k = P_k^- H_k^T \left(H_k P_k^- H_k^T + R_k \right)^{-1}, \tag{3.38}$$

and P_k^- denotes the cofactor matrix of the error for $\hat{\boldsymbol{x}}_k^-$, which can be easily derived from Eq. (3.33):

$$P_k^- = Q_k + \Phi P_{k-1} \Phi^T. \tag{3.39}$$

Since the mean squared prediction error (MSPE) of $\hat{\boldsymbol{x}}_k$ can be computed by

$$
\begin{aligned}
MSPE\{\hat{\boldsymbol{x}}_k\} &= D\{\hat{\boldsymbol{x}}_k - \boldsymbol{x}_k\} \\
&= D\{(\hat{\boldsymbol{x}}_k - \hat{\boldsymbol{x}}_k^-) - (\boldsymbol{x}_k - \hat{\boldsymbol{x}}_k^-)\} \\
&= D\{\hat{\boldsymbol{x}}_k - \hat{\boldsymbol{x}}_k^-\} - C\{\hat{\boldsymbol{x}}_k - \hat{\boldsymbol{x}}_k^-, \boldsymbol{x}_k - \hat{\boldsymbol{x}}_k^-\} \\
&\quad -C\{\boldsymbol{x}_k - \hat{\boldsymbol{x}}_k^-, \hat{\boldsymbol{x}}_k - \hat{\boldsymbol{x}}_k^-\} + D\{\boldsymbol{x}_k - \hat{\boldsymbol{x}}_k^-\},
\end{aligned}
\tag{3.40}
$$

the cofactor matrix P_k of the error for the estimated state vector $\hat{\boldsymbol{x}}_k$ can be derived from Eqs. (3.33), (3.37), and (3.39):

$$
\begin{aligned}
P_k &= (I - K_k H_k) P_k^- \\
&= (I - K_k H_k) P_k^- (I - K_k H_k)^T + K_k R_k K_k^T .
\end{aligned}
\tag{3.41}
$$

The optimal unbiased estimate of the variance component is given as

$$
\hat{\sigma}_0^2 = \frac{\tilde{\boldsymbol{v}}_k^T R_k \tilde{\boldsymbol{v}}_k + \tilde{\boldsymbol{w}}_k^T Q_k \tilde{\boldsymbol{w}}_k + (\tilde{\boldsymbol{v}}_{k-1}^0)^T P_{k-1} \tilde{\boldsymbol{v}}_{k-1}^0}{n}.
\tag{3.42}
$$

This Kalman filtering procedure can be propagated through time from the given initial state vector and the cofactor matrix of the errors on the initial information, $\hat{\boldsymbol{x}}_0$ and P_0, respectively.

Depending on the strategy of the state vector update, the Kalman filtering can be divided into two variants: the Linearized Kalman Filter (LKF) and the Extended Kalman Filter (EKF). While only one initial value problem is solved in LKF, the state vector in EKF is updated at every measurement epoch; thus, the integration process needs to be reinitialized for each measurement epoch (Montenbruck and Gill, 2001). Note that Kalman filtering produces the batch filter of Chapter 3.1.1 if Q_k is set to 0 for all k.

3.1.4 Smoothing

Since the state vector is estimated in Eq. (3.37) based on the measurements up to t_k only, the measurements after this time epoch are not used in the estimation. Therefore, the smoothing problem in the Kalman filtering requires obtaining the optimal estimates of the state vector at each epoch (Davis, 1996). The smoothing method filters the data in reverse time order, with the state vector estimate and its error covariance matrix at the last epoch (that were estimated from the forward filtering) as *a priori* information. Thus, after the smoothing procedure, that is, after forward and backward filtering, all the estimated state vectors and the covariance matrices of the corresponding errors are derived on the basis of the data within the entire arc.

Let $\hat{\boldsymbol{x}}_k^l$ and P_k^l be the estimated state vector and the cofactor matrix of the errors for the corresponding estimates at time t_k, respectively, based on all measurements in the interval, say $[t_0, t_l]$. The estimates of the state vector and the cofactor matrix of the errors for the corresponding estimates based on the measurements up to t_k (*i.e.*, $\hat{\boldsymbol{x}}_k^k$ and P_k^k) are computed from the Kalman forward filter as given in Eqs. (3.37) to (3.41). Then the same filtering technique can be performed, but backwards in time right from the epoch t_N, resulting in $\hat{\boldsymbol{x}}_k^N$ and P_k^N. The smoothing algorithm can also be explained in a Gauss-Markov model with stochastic constraints:

$$\hat{\boldsymbol{x}}_{k+1}^N = \Phi(t_{k+1}, t_k)\boldsymbol{x}_k + \boldsymbol{w}_{k+1}, \quad \boldsymbol{w}_{k+1} \sim \mathcal{N}(0, \sigma_0^2 Q_{k+1}), \tag{3.43}$$

$$\hat{\boldsymbol{x}}_k^k = \boldsymbol{x}_k + \boldsymbol{v}_k^0, \quad \boldsymbol{v}_k^0 \sim \mathcal{N}(0, \sigma_0^2 P_k^k), \quad C\{\boldsymbol{w}_{k+1}, \boldsymbol{v}_k^0\} = 0. \tag{3.44}$$

Therefore, the weighted LESS can be derived by differentiating the Lagrange target function with respect to $\boldsymbol{x}_k$, and setting these derivatives to zero:

$$\begin{aligned} J &= \boldsymbol{w}_{k+1}^T Q_{k+1}^{-1} \boldsymbol{w}_{k+1} + \left(\boldsymbol{v}_k^0\right)^T \left(P_k^k\right)^{-1} \boldsymbol{v}_k^0 \\ &= \left(\hat{\boldsymbol{x}}_{k+1}^N - \Phi(t_{k+1}, t_k)\boldsymbol{x}_k\right)^T Q_{k+1}^{-1} \left(\hat{\boldsymbol{x}}_{k+1}^N - \Phi(t_{k+1}, t_k)\boldsymbol{x}_k\right) \\ &\quad + \left(\hat{\boldsymbol{x}}_k^k - \boldsymbol{x}_k\right)^T \left(P_k^k\right)^{-1} \left(\hat{\boldsymbol{x}}_k^k - \boldsymbol{x}_k\right). \end{aligned} \tag{3.45}$$

$$\frac{1}{2}\frac{\partial J}{\partial x_k} = 0. \tag{3.46}$$

From Eqs. (3.45) and (3.46), the resulting solution can be obtained as

$$\begin{aligned} \hat{\boldsymbol{x}}_k^N &= \left[\left(P_k^k\right)^{-1} + \Phi^T Q_{k+1}^{-1} \Phi\right]^{-1} \left[\left(P_k^k\right)^{-1} \hat{\boldsymbol{x}}_k^k + \Phi^T Q_{k+1}^{-1} \hat{\boldsymbol{x}}_{k+1}^N\right] \\ &= \hat{\boldsymbol{x}}_k^k + S_k \left(\hat{\boldsymbol{x}}_{k+1}^N - \Phi\, \hat{\boldsymbol{x}}_k^k\right), \end{aligned} \tag{3.47}$$

where

$$
\begin{aligned}
S_k &= \left[\left(P_k^k \right)^{-1} + \Phi^T Q_{k+1}^{-1} \Phi \right]^{-1} \Phi^T Q_{k+1}^{-1} \\
&= P_k^k \Phi^T \left(\Phi P_k^k \Phi^T + Q_{k+1} \right)^{-1} \\
&= P_k^k \Phi^T \left(P_{k+1}^k \right)^{-1} .
\end{aligned}
\tag{3.48}
$$

The cofactor matrix of the error for the corresponding smoothed estimates is given by

$$
P_k^N = P_k^k + S_k \left(P_{k+1}^N - P_{k+1}^k \right) S_k^T . \tag{3.49}
$$

A more detailed derivation is given by Tapley et al. (2004, Chapter 4.15).

3.2 Kinematic Positioning

Kinematic orbit determination, known also as the geometric approach, is accomplished by using GPS measurements only, and is a viable alternative to the dynamic POD. It requires neither dynamic force models nor the physical properties of the LEO. Consequently, there are no dynamic modeling errors, the result of which is a procedure that is simple and computationally efficient. However, the quality and the continuity of the kinematic orbit determination are strongly dependent on the available GPS data and the observational geometry involved in the measurements (Kwon et al., 2003; Grejner-Brzezinska et al., 2004). Therefore, strengthening the constellation geometry and developing robust data screening techniques that remove weak observations are some of the critical steps in the kinematic approach. However, since a LEO (such as CHAMP, analyzed here) moves very fast (about two times faster than the GPS satellites) and in a much lower orbit, the geometry changes rapidly; thus, it is virtually impossible to obtain good continuous results with the kinematic approach (Kuang et al., 2001) with the current GPS constellation. However, there will be numerous satellites available, making future kinematic POD much more reliable, with the growing constellation of Russian GLONASS (GLObal NAvigation Satellite System, http://www.glonass-ianc.rsa.ru) and the upcoming GNSS systems, such as Galileo (http://www.esa.int/esaNA/galileo.html), EGNOS (European Geostationary Navigation Overlay Satellite Service, http://www.esa.int/ esaNA/egnos.html), Japanese MTSAT (Multi-functional Transport Satellite, http://www.jma.go.jp/ jma/jma-eng/satellite/) and QZSS (Quasi-Zenith Satellite System, http://qzss.jaxa.jp/), Chinese Beidou (http://www.astronautix.com/craft/beidou.htm), and Indian GAGAN (GPS-Aided Geo-Augmented Navigation, http://www.isro.org/) and IRNS (Indian Regional Navigation System, http://www.isro.org/pressrelease/Jul04_2006.htm).

Figure 3.1 shows the schematic diagram of the data processing for kinematic POD. This procedure can be similarly applied to the dynamic and reduced-dynamic approaches, except for some modifications of the estimation filter in the main procedure.

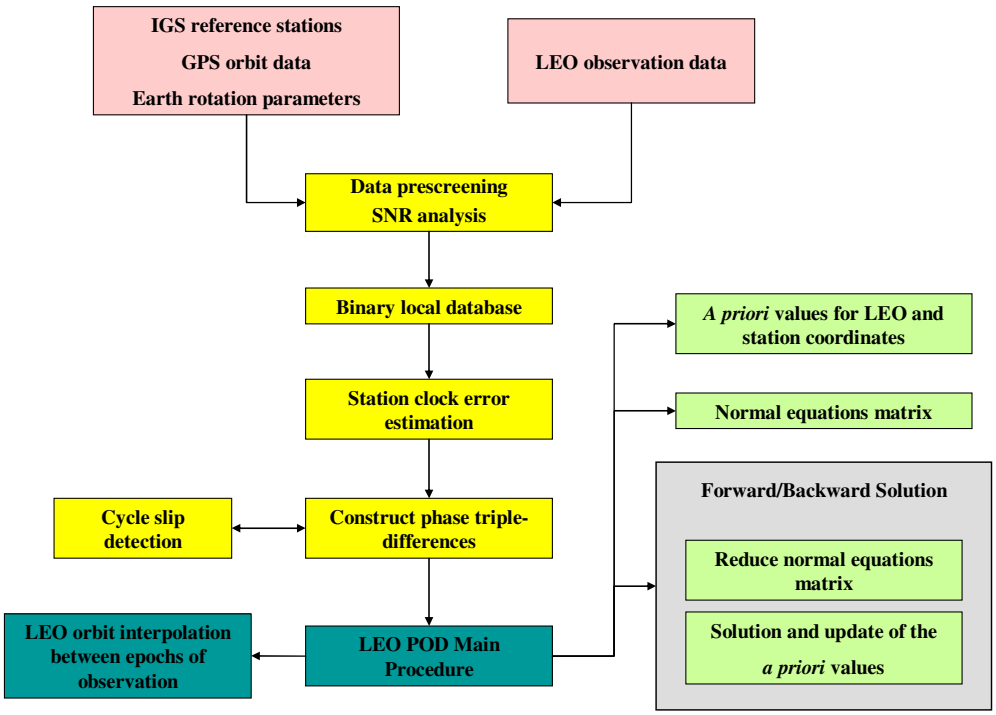

Figure 3.1 Procedures of LEO kinematic precise orbit determination.

3.2.1 Data Preprocessing

As mentioned above, the kinematic method has a strong dependence on the data quality and availability; thus, the preprocessing (especially cycle slip detection) is important for the precise orbit determination in the kinematic approach. A cycle slip is defined as a jump in the instantaneous accumulated phase by an integer number of cycles. This can be caused by signal blocking, low Signal-to-Noise Ratio (SNR), and a failure in the receiver software (Hofmann-Wellenhof et al., 2004). A cycle slip affects only a single epoch in triple-differenced observations; thus, it can just be removed from the database instead of attempting to determine its magnitude in order to fix it, which is a time-consuming and difficult task.

A cycle slip can be detected by the testing quantities which are generally composed of measured carrier phases and code ranges. Many algorithms have been developed to get the testing quantities (Blewitt, 1990; Bisnath and Langley, 2001; Bae et al., 2002), and two of them are considered here. The first method is based on the wide-lane ambiguity

and the ionospheric residuals. Expressing the code and phase measurement equation in cycle units of the corresponding carrier and neglecting the initial fractional phases as well as the interchannel bias, the following equations can be obtained:

$$\begin{aligned}\frac{\Phi_1 - P_1}{\lambda_1} &= -\frac{2I}{cf_1} + N_1 + \frac{\varepsilon_1 - e_1}{\lambda_1}, \\ \frac{\Phi_2 - P_2}{\lambda_2} &= -\frac{2I}{cf_2} + N_2 + \frac{\varepsilon_2 - e_2}{\lambda_2},\end{aligned} \tag{3.50}$$

where sub- and superscripts are omitted. By subtracting these two equations, one can arrive at

$$\frac{\Phi_w}{\lambda_w} - \frac{P_1}{\lambda_1} + \frac{P_2}{\lambda_2} = \frac{2I}{c}\left(\frac{1}{f_2} - \frac{1}{f_1}\right) + N_w + \frac{\varepsilon_1 - e_1}{\lambda_1} - \frac{\varepsilon_2 - e_2}{\lambda_2}, \tag{3.51}$$

where

$$\begin{aligned}N_w &= N_1 - N_2, \\ \lambda_w &= \frac{\lambda_1 \lambda_2}{\lambda_2 - \lambda_1}, \\ \Phi_w &= \lambda_w \left(\frac{\Phi_1}{\lambda_1} - \frac{\Phi_2}{\lambda_2}\right).\end{aligned} \tag{3.52}$$

Similarly, by subtracting the code ranges (in distance unit) after dividing by the speed of light, the testing quantity for the wide-lane ambiguity is composed as

$$\hat{N}_w = \frac{\Phi_w}{\lambda_w} - \frac{f_1 - f_2}{f_1 + f_2}\left(\frac{P_1}{\lambda_1} + \frac{P_2}{\lambda_2}\right), \tag{3.53}$$

neglecting the random error part. This can be used to determine the cycle slip along with the ionospheric residual given by

$$\frac{1}{\lambda_1}(\Phi_1 - \Phi_2) = \left(N_1 - \frac{\lambda_2}{\lambda_1} N_2\right) - \frac{I}{\lambda_1 f_1^2}\left(1 - \frac{f_1^2}{f_2^2}\right). \tag{3.54}$$

Once the test quantity is available, cycle slips can be detected by differencing the

values at two consecutive epochs, which amplifies the effect of a cycle slip to make the detection easy. It should be noted that, although Eq. (3.53) is independent of the baseline length and the ionospheric effects, it is still affected by the multipath in a different way for the carrier phase and code. In addition, CHAMP moves very fast in the middle of the ionospheric layer; thus, since Eq. (3.54) is based on the assumption of a quality pseudo-range measurement and a normal ionospheric condition, it may not work very reliably even on moderately active ionospheric days.

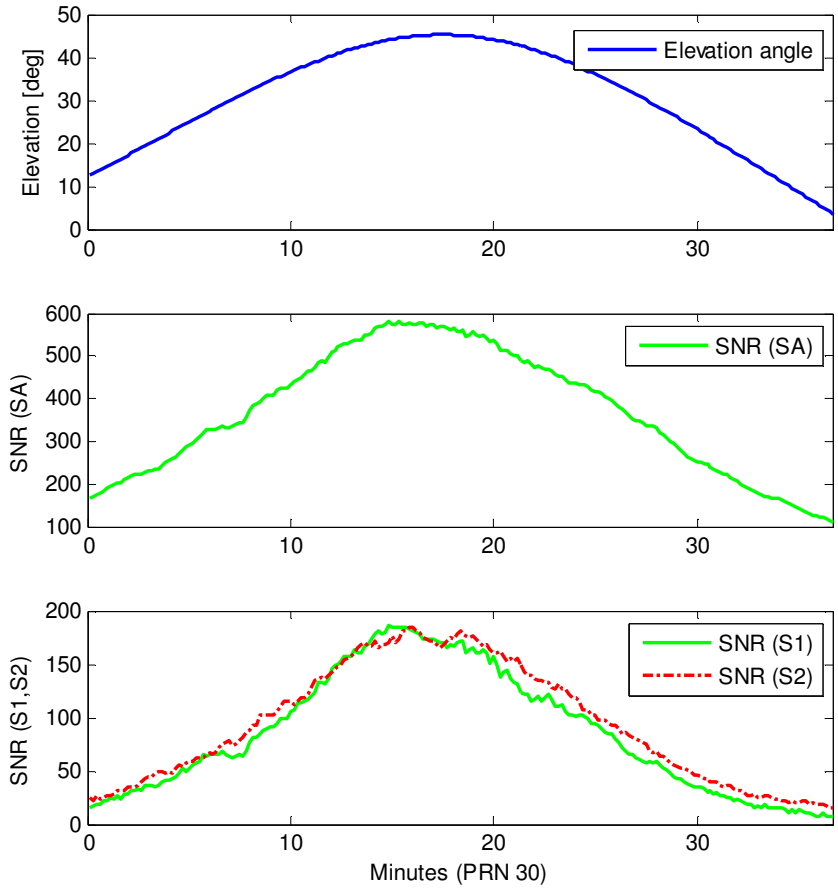

Figure 3.2 SNR variation of CHAMP with respect to the elevation angle.

Another method, useful in cycle slip detection, is analyzing the Signal-to-Noise ratio (SNR). The low-rate CHAMP SST (Satellite-to-Satellite Tracking) data provide three types of SNR data: S1 and S2 which correspond to the L1 and L2 channels, respectively, and SA for the C/A channel. The SNR generally changes its amplitude according to the elevation angles of the GPS satellites (Figure 3.2), which is the reason why the low elevation data are generally not used in the processing. Under the low SNR condition, there is a greater chance of cycle slip occurrence.

The challenge for the cycle slip detection when using the SNR data lies in the proper selection of the SNR threshold. One possibility is to perform the preliminary analysis on the cycle slips. This analysis can be done by checking the triple-differenced least-squares residuals, based on a good *a priori* orbit (for example, the published Rapid Science Orbit), followed by a comparison with the SNR values. Once the cycle slips are identified, they can be removed from the database because, as mentioned earlier, the cycle slip affects only a single epoch in triple-differenced observations.

The objective of this study, however, is to provide the near real-time orbit solution, thus, it should be independent of the *a priori* orbit. Fortunately, the triple-differenced observations are not very sensitive to the data quality, and the cycle slips are usually identified as data outliers (indicated by large residuals of the measurements) without any external orbit solutions, as demonstrated in Chapter 5.

3.2.2 Mathematical Model

As can be seen in the equation of the triple-differenced ionosphere-free carrier phase observations which is written as

$$\Phi_{ij,dt,ion-free}^{kl} = \rho_{ij,dt}^{kl} + T_{ij,dt}^{kl} + \alpha_1 \varepsilon_{ij,1,dt}^{kl} + \alpha_2 \varepsilon_{ij,2,dt}^{kl}, \tag{3.55}$$

only the geometric and tropospheric terms (with the exception of the random errors) are left in the equation. Assuming that the GPS satellite orbits and the coordinates of the ground stations are available and the tropospheric effect is modeled, then the coordinates of the LEO satellite are the only remaining unknowns. After the linearization of Eq. (3.55), the observation equations are given by

$$\begin{aligned} &\Phi_{ij,dt,ion-free}^{kl} - \left[\rho_{ij,dt}^{kl}\right]^0 - \left[T_{ij,dt}^{kl}\right]^{\text{model}} \\ &\quad = \left[-\left(\frac{\mathbf{r}_i - \mathbf{r}^k}{\rho_i^k} - \frac{\mathbf{r}_i - \mathbf{r}^l}{\rho_i^l} \right)_{t_1} \;\middle|\; \left(\frac{\mathbf{r}_i - \mathbf{r}^k}{\rho_i^k} - \frac{\mathbf{r}_i - \mathbf{r}^l}{\rho_i^l} \right)_{t_2} \right]^0 \begin{bmatrix} d\mathbf{r}_{t_1} \\ d\mathbf{r}_{t_2} \end{bmatrix} + e_{ij,dt,ion-free}^{kl}, \end{aligned} \tag{3.56}$$

where $\mathbf{r}$ denotes the position vector and the superscript ^{0} represents an evaluation with the approximate values. The rest of the notation is the same as in Chapter 2. The observation equations can be accumulated during the batch and solved for the LEO orbit in a batch processor. Since the triple-differenced observations contain only the relative information between the consecutive epochs, it is necessary to introduce the datum reference at the specific epoch, usually the first epoch of the batch. Stochastic constraints for all epochs can also be used to eliminate the rank deficiency. It should be noted, however, that the fixed datum reference can introduce a bias in the orbit solution because

of an inaccuracy of the datum (Kwon et al., 2003). Therefore, one may have to run a backward filter by fixing the coordinates of the last epoch from the forward filter to reduce the effect of this bias.

As can be seen in Eq. (3.56), the only term to be taken care of, except for the geometric range, is the tropospheric delay. The tropospheric effect is generally accurately modeled for the dry component. Most of the model error, however, comes from the modeling of the wet component because of the difficulties in the water vapor modeling (Hofmann-Wellenhof et al., 2004). The modified Hopfield model by Goad and Goodman (1974), one of the widely used tropospheric models, was empirically derived from the global data as a function of range from the station to the satellite and the elevation angle (equivalently the zenith angle). Thus, the mapping function is already included in the model, and the dry and wet path delays can be computed separately. One of the recent models is UNB3, developed at the University of New Brunswick for the Wide Area Augmentation System (WAAS) program (Leandro et al., 2006). This model uses the Saastamoinen zenith delay models, Niell mapping functions, and a look-up table for temperature, pressure and water vapor pressure, varying with respect to latitude and height. This look-up table uses an annual mean and the amplitude of a cosine function to facilitate interpolation of the meteorological parameters for a particular latitude and day of year. However, it is noteworthy to mention that these data can usually experience and/or exhibit sudden changes. Moreover, this model is validated by the stations in North America only; therefore, the modified Hopfield model is used in this study. The details of the modified Hopfield model technique can be found in Goad and Goodman (1974) or Hofmann-Wellenhof et al. (2004).

The deficiency in the tropospheric model can usually be compensated for by estimating the scaling factor for each site and session. In LEO POD, however, the LEO position is generally the only concern; thus, the scaling factors to compensate the tropospheric model error are not estimated, since the GPS measurements from the ground stations are involved only when they have common visibility with the LEO satellite, in case the differenced observations are used. Fortunately, in the triple-differenced observations, the impact of the biases in the tropospheric model is not significant because the tropospheric condition is almost identical between the measurement intervals (30 seconds in this study); therefore, the biases are removed by differencing in time.

3.2.3 Augmentation of the Positioning Satellites

The most difficult problem to be overcome in the kinematic approach is that of a data gap which will result in the singularity in the system of normal equations. Once the singularity occurs, the orbit determination procedure should be restarted with a new segment. Other than the data gaps, the quality and continuity of kinematic orbit determination can be improved by augmenting the positioning satellites. Augmentation can be made possible in many ways: 1) by incorporating other GNSS satellites, such as those of the upcoming Galileo system (http://www.esa.int/esaNA/galileo.html); 2) by

placing pseudolite (PL) transceivers on the ground; 3) by placing the PLs on other LEOs. The PL transceivers can transmit and receive GPS compatible signals. The concept of PLs is similar to DORIS (Doppler Orbitography and Radio positioning Integrated by Satellite) which measures the Doppler count emitted by ground beacons (Willis et al., 2005). Some practical problems, however, need to be considered for the application of PLs (Grejner-Brzezinska et al., 2004).

A simulation study was performed to verify how much improvement can be expected from the GPS augmentation. Considering the fact that the kinematic approach is highly dependent on the geometry of the positioning satellites, the simulation can be focused on the measure of geometric strength, which is represented by the geometric dilution of precision (GDOP). Two revolutions of CHAMP data on February 15, 2003 were selected for the simulation. The GPS and Galileo orbits were propagated from the almanac data, and the PL transceivers were located on the 40 IGS ground stations.

As can clearly be seen in Figures 3.3 and 3.4, the largest effect comes from the incorporation of the Galileo constellation, while the PLs also contribute to the overall geometric strength. Of course, the benefits of the modernized GPS signal, discussed in Chapter 2, can further contribute to the improvement of the kinematic approach. However, a problem of coverage from PLs still exists since the LEO orbits are at very low altitude compared to the GPS altitude. Therefore, the configuration of PLs as well as the ground stations must be optimally distributed, the relevant issues of which will be discussed in Chapter 4.

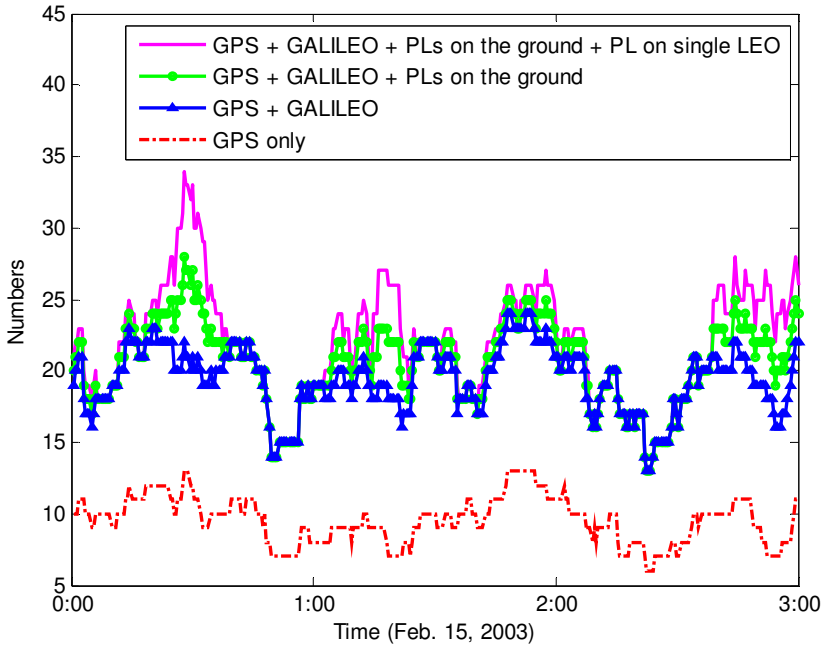

Figure 3.3 The number of range measurements.

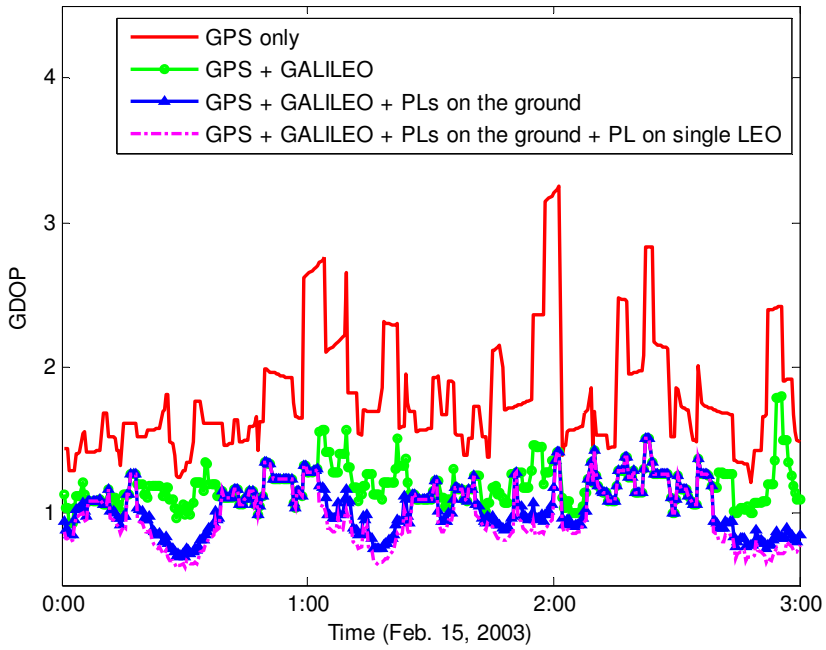

Figure 3.4 The geometric dilution of precision (GDOP).

3.3 Dynamic Precise Orbit Determination

Unlike the kinematic POD, in the dynamic POD method all forces acting on the satellite are computed and integrated numerically to estimate the initial state vector (position and velocity) and other unknown parameters, such as the scaling factors for the solar radiation pressure and atmospheric drag (Schutz et al., 1994; Grejner-Brzezinska, 1995; Bock, 2003). These parameters are connected to the GPS measurements via the variational partials; therefore, the final orbit solution can be improved by estimating these unknown parameters together with the initial state vector. Once the initial state vector and other dynamic parameters are estimated, the state vector for the following epochs can be propagated using the force models used in the estimation process, and as a result, the errors in the dynamic approach will grow as the arc length increases. Sometimes, pseudo-stochastic pulses are set up at pre-determined epochs to introduce the velocity change in a pre-determined direction (Švehla and Rothacher, 2003; Bock, 2003), similarly to the earlier "wave filter" of Salychev and Schaffrin (1992). Given that the reduced-dynamic approach tends to be classified based on the inclusion of additional process noise to absorb the unmodeled forces, the practice of including the empirical forces in the dynamic approach makes it difficult to differentiate decisively between the dynamic and reduced-dynamic techniques of POD.

As already mentioned in Chapter 2, the CHAMP accelerometer data cannot reflect accurately all nonconservative forces acting on the satellite. In addition, the preliminary test results done in this study show that the bias of the accelerometer data in along-track component amounts to 0.06 mGal (1 mGal = $10^{-5} m/s^2$). Therefore, the nonconservative forces, which are dominated by the atmospheric drag forces, must be modeled and improved in the dynamic orbit determination process.

3.3.1 Dynamic Force Models

The equation of motion of the satellite is generally expressed in the Earth Centered Inertial (ECI) frame as follows (Hugentobler et al., 2001):

$$\ddot{\mathbf{r}} = -\frac{kM}{r^3}\mathbf{r} + \mathbf{a}(t, \mathbf{r}, \dot{\mathbf{r}}, \mathbf{p}), \tag{3.57}$$

with

- $\mathbf{r}$: the 3×1 satellite position vector in the inertial frame at time t;
- $\dot{\mathbf{r}}$: the velocity of the satellite at time t;
- $\ddot{\mathbf{r}}$: total acceleration of the satellite at time t;
- kM : the product of the gravitational constant and the mass of the Earth;
- r : the magnitude of the position vector $\mathbf{r}$;
- $\mathbf{a}$: total perturbing forces;
- t : time, at which the acceleration is calculated;
- $\mathbf{p}$: the dynamic parameter vector which induces the perturbing acceleration.

The sum of all perturbing forces, $\mathbf{a}$, represents the third-body gravitational forces, atmospheric drag, solar radiation pressure and/or some empirical force terms which normally account for all unmodeled forces, including the nonspherical part of the Earth's gravity field. These perturbing forces as well as the Keplerian accelerations are computed at each epoch and then numerically integrated to get the position and velocity of the satellite in the next epoch. The obtained position and velocity of the satellite are used to validate the measurements from GPS satellites at the same epoch, and finally update the unknown parameter vector including the initial state vector, as was mentioned earlier.

Table 3.2 shows the summary of the models and the conventions, which are related to the perturbing forces and are used in this study. EIGEN2 is the geopotential model, maximum degree and order up to 140, which is generated from six months of CHAMP data only.

Model	Standard
Geopotential	EIGEN2 (140×140)
Earth orientation parameters	IERS Bulletin B
Solid Earth tides	IERS Conventions (2003)
Ocean tides	CSR 3.0
Atmospheric density	NRLMSISE-00
Third body	Moon and Sun
Conventional inertial system	J2000.0
Terrestrial reference frame	ITRF2000 (velocity applied)
Precession/Nutation	IAU 2000A
Planetary ephemerides	JPL DE405
Relativistic correction	IERS Conventions (2003)
Tidal displacement of stations	IERS Conventions (2003)
Reference ellipsoid	CHAMP reference ellipsoid

Table 3.2 Summary of the strategies for the dynamic precise orbit determination.

Solid Earth tides are implemented for both the temporal variation of the geopotential coefficients and the displacement of the IGS ground stations based on IERS Conventions (2003); see McCarthy and Petit (2003). It should be mentioned here that since EIGEN2 geopotential model is the "conventional tide-free" model, the permanent part (zero frequency) of the tidal effects can be taken care of by the full tidal model given by IERS Conventions (2003). For the ocean tides, the CSR 3.0 model obtained from the analysis of TOPEX/POSEIDON altimeter data is used. Only the Moon and the Sun are considered for the third-body perturbations. The equation of motion can be solved by any numerical integration method in the inertial frame; therefore, all the coordinates and the force components computed in the terrestrial frame should be transformed into the inertial frame. For this transformation, the new IAU 2000A resolutions are used for the precession/nutation model (see Appendix C), based on the reference origin at J2000.0. Since the atmospheric and empirical force modeling is critical in dynamic orbit determination of a LEO, these models, along with other perturbing forces, are described in detail in the next section.

3.3.1.1 Gravitational Acceleration

CHAMP experiences significant perturbations from the nonspherical gravitational potential because of its very low altitude above the Earth. Let V be the gravitational potential, then it can generally be represented in the form of spherical harmonics (see Heiskanen and Moritz (1967), Eq. (2-39)), including the Keplerian term (central part of

the Earth gravity field):

$$V = \frac{kM}{r} \sum_{n=0}^{n_{\max}} \sum_{m=0}^{n} \left(\frac{R}{r} \right)^n \left(\bar{C}_{nm} \cos m\lambda + \bar{S}_{nm} \sin m\lambda \right) \bar{P}_{nm}(\cos\theta) \tag{3.58}$$

with

V : the gravitational potential;
kM : the product of the gravitational constant and the mass of the Earth;
R : the mean radius of the Earth;
r : the radial distance from the center of the Earth;
θ, λ : the geocentric co-latitude and longitude, respectively;
$\bar{P}_{nm}$: the fully normalized associated Legendre functions;
n, m : the degree and order of $\bar{P}_{nm}$, respectively;
$n_{\max}$: the maximum degree;
$\bar{C}_{nm}, \bar{S}_{nm}$: the spherical harmonic coefficients corresponding to $\bar{P}_{nm}$.

Since the force vector is just the gradient vector of the scalar-valued potential function *V*, the gravitational perturbing forces can be obtained by taking derivatives of the potential with respect to the position vector:

$$\ddot{\mathbf{r}} = \nabla V = \left(\frac{\partial V}{\partial x} \quad \frac{\partial V}{\partial y} \quad \frac{\partial V}{\partial z} \right)^T . \tag{3.59}$$

As can be seen in Eq. (3.58), the potential is expressed as a function of the spherical coordinates, (r, θ, λ) . Similarly, the partial derivatives can be evaluated in this coordinate system, and then transformed into the Cartesian coordinates of the Earth-centered and Earth-fixed (ECF) frame. Afterwards, it should be transformed again into the inertial frame to be combined with other perturbing forces. The detailed partial derivatives of the geopotential with respect to the spherical coordinates are given in Appendix A.

The fully normalized associated Legendre functions are easier and more convenient to handle as compared to the unnormalized ones, thus, the former is more widely used.

Many efforts were directed towards developing an efficient method to compute the fully normalized associated Legendre functions (Colombo, 1981; Tscherning et al., 1983; Jekeli, 1996), and these are given in Appendix B.

3.3.1.2 Third-body Attraction

The acceleration of a satellite by a point mass, M, can be computed by the following equation (Montenbruck and Gill, 2001):

$$\ddot{\mathbf{r}} = -kM\left(\frac{\mathbf{r}-\mathbf{s}}{|\mathbf{r}-\mathbf{s}|^3}+\frac{\mathbf{s}}{|\mathbf{s}|^3}\right), \tag{3.60}$$

where k is the gravitational constant, and $\mathbf{s}$ represents the geocentric coordinates of the perturbing mass (*i.e.*, the position vector of the Moon and the Sun, respectively, in this study). The partial derivatives of the acceleration with respect to the satellite position vector are represented by

$$\frac{\partial \ddot{\mathbf{r}}}{\partial \mathbf{r}^T} = -kM\left(\frac{1}{|\mathbf{r}-\mathbf{s}|^3}I_3 - 3\frac{(\mathbf{r}-\mathbf{s})(\mathbf{r}-\mathbf{s})^T}{|\mathbf{r}-\mathbf{s}|^5}\right), \tag{3.61}$$

where I_3 represents the 3×3 identity matrix.

In this study, the attractions from the Moon and the Sun are considered. The recommended planetary ephemerides is DE405 developed by JPL (McCarthy and Petit, 2003). DE405 provides the relative position and velocity between Sun, Moon and nine planets in three-dimensional space, as well as some constants for the ephemerides. DE405 is based on the ICRF (International Celestial Reference Frame), and the time-independent input variable is TDB (Barycentric Dynamic Time) in fractional Julian days. The description and software to compute the coordinates of the planet can be found at ftp://ssd.jpl.nasa.gov/pub/eph/export/.

3.3.1.3 Solar Radiation Pressure

Solar radiation pressure is the perturbation due to the photons coming from the Sun. Therefore, it is dependent on the mass and surface area of the satellite, as well as on the geometry of the satellite with respect to the Earth and the Sun. This perturbing force is very difficult to model because of the irregular shape of the spacecraft and the highly complex properties of the surface materials. Contrary to the GPS satellites, there is no recommended model for the CHAMP satellite; thus, the simple area-to-mass ratio or

"cannonball" model is generally used together with the estimation of the scaling factor to compensate for any model error.

Solar radiation pressure acting on the spacecraft can be computed from the simplified equation of

$$\ddot{\mathbf{r}} = -4.56\times10^{-6} C_r \frac{A}{m} \frac{\mathbf{r}_\odot}{r_\odot^3} (AU)^2, \tag{3.62}$$

with

$\mathbf{r}_\odot$: the vector from the satellite to the Sun;
$r_\odot$: the magnitude of the vector $\mathbf{r}_\odot$;
C_r: the scaling factor for the solar radiation pressure;
A/m: the area-to-mass ratio;
AU: Astronomical Unit.

The partial derivatives of the acceleration with respect to the satellite position vector are given by

$$\frac{\partial \ddot{\mathbf{r}}}{\partial \mathbf{r}^T} = +4.56\times10^{-6} C_r \frac{A}{m} (AU)^2 \left(\frac{1}{|\mathbf{r}-\mathbf{s}|^3} I_3 - 3\frac{(\mathbf{r}-\mathbf{s})(\mathbf{r}-\mathbf{s})^T}{|\mathbf{r}-\mathbf{s}|^5} \right), \tag{3.63}$$

where I_3 represents the 3×3 identity matrix as before, and $\mathbf{s}$ represents the geocentric position vector of the Sun. The partial derivative of the acceleration with respect to the solar radiation scaling factor, C_r, is simply obtained from Eq. (3.62).

Due to the estimated scaling factor, the solar radiation pressure can be accounted for with high accuracy without knowing the details of the structure, orientation and reflectivity of the spacecraft (Montenbruck and Gill, 2001).

3.3.1.4 Atmospheric Drag Forces

As mentioned earlier, since the atmospheric effect is significant at the LEO altitude, the acceleration due to atmospheric drag must be properly evaluated in the LEO POD process. The orbit error, for example, reaches approximately ±1000 m after two revolutions without proper modeling of the atmospheric drag (Bae, 2005b). It is difficult, however, to model the atmosphere accurately because the physical properties of the atmosphere (particularly the density of the upper atmosphere) are not sufficiently known.

Moreover, a detailed knowledge of the interaction of neutral gases as well as charged particles with the different spacecraft surfaces is required. In addition, the varying attitude of nonspherical satellites with respect to the atmospheric particle flux makes its modeling even more difficult (Montenbruck and Gill, 2001). Numerous atmospheric models have been published and are currently in use. Among these models, the most recently published NRLMSISE-00 model is used in this study.

The NRLMSISE-00 (NRL Mass Spectrometer, Incoherent Scatter Radar Extended Model) was developed based on the satellite mass spectrometer and ground-based incoherent scatter data, and provides a single analytic model for calculating temperature and density profiles (Hedin, 1991; MSIS, 2004). This model is a function of many different variables, including local time, latitude, annual/semiannual, and longitude variations. It is expanded in terms of the lower-order spherical harmonics and the Fourier series with the parameters of the temperature profile and density boundary conditions at 120 km. This model allows for easy determination of temperature and density profiles for specific geographic and solar/magnetic parameters. The official release of the FORTRAN code for the NRLMSISE-00 atmospheric model can be found at http://uap-www.nrl.navy.mil/models_web/msis/NRLMSISE-00.DIST17.TXT. This subroutine requires time, location, solar radio flux at 10.7 cm in units of 10^{-22} W/(m^{2}Hz) and the magnetic activity index as input variables, and provides the atmospheric densities as well as total mass density and temperature at the desired altitude. The actual solar flux and the magnetic index data with their formats are available at ftp://ftp.ngdc.noaa.gov/STP/GEOMAGNETIC_DATA/ INDICES/KP_AP/.

Figure 3.5 represents the total mass density variation along the CHAMP trajectory using the NRLMSISE-00 atmosphere model on February 15, 2003. It should be noted that the atmospheric density repeats itself for every orbit with a slight change; therefore, the selection of the time interval for the estimation of the coefficients is an important issue for the precision orbit determination.

With the assumption that the atmosphere co-rotates with the Earth, the atmospheric drag forces can be computed by

$$\ddot{\mathbf{r}} = -\frac{1}{2} C_D \frac{A}{m} \rho \, v_r \mathbf{v}_r , \tag{3.64}$$

$$\mathbf{v}_r = \mathbf{v} - \boldsymbol{\omega} \times \mathbf{r} , \tag{3.65}$$

where ρ is the atmospheric density at satellite position and $\mathbf{v}_r$, which has a magnitude of v_r, represents the relative velocity of the satellite with respect to the atmosphere. The Earth angular velocity vector $\boldsymbol{\omega}$ is given as

$$\boldsymbol{\omega} = \begin{bmatrix} 0 & 0 & \omega_e \end{bmatrix}^T \tag{3.66}$$

with the nominal value of $\omega_e = 7.292115\times10^{-5}$ rad/sec. The dimensionless quantity, C_D, is an unknown parameter to be estimated in the orbit determination procedure; it compensates the atmosphere model error.

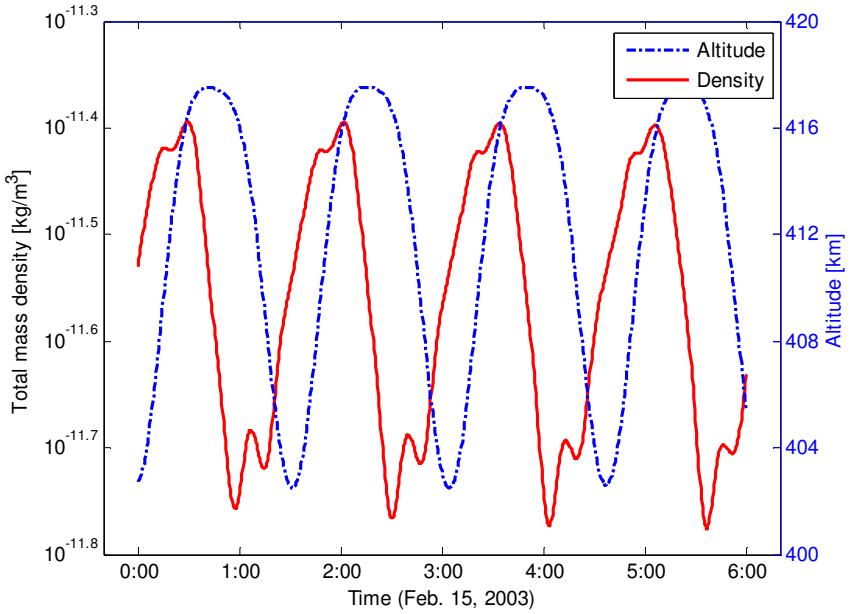

Figure 3.5 Total mass density along the CHAMP trajectory.

The partial derivatives of the acceleration with respect to the drag coefficient, C_D, can be computed as follows:

$$\frac{\partial \ddot{\mathbf{r}}}{\partial C_D} = \frac{\partial \ddot{\mathbf{r}}}{\partial C_D} + \frac{\partial \ddot{\mathbf{r}}}{\partial \mathbf{r}^T}\frac{\partial \mathbf{r}}{\partial C_D}. \tag{3.67}$$

The first term on the right side of Eq. (3.67) represents the explicit component of the partial derivatives, which can easily be computed from Eq. (3.64). The second term, however, is an implicit part of the partial derivatives, which requires more careful attention. The partial derivatives of the position vector with respect to the drag coefficient can be obtained by numerical integration of Eq. (3.67) up to the current epoch. The partial derivatives of the acceleration with respect to the position vector can be derived analytically as follows:

$$\frac{\partial \ddot{\mathbf{r}}}{\partial \mathbf{r}^T} = -\frac{1}{2} C_D \frac{A}{m} v_r \mathbf{v}_r \frac{\partial \rho}{\partial \mathbf{r}^T} + \frac{1}{2} C_D \frac{A}{m} \rho \left(\frac{1}{v_r} \mathbf{v}_v \mathbf{v}_v^T + v_r I_3 \right) [\boldsymbol{\omega}\times], \tag{3.68}$$

where I_3 represents the 3×3 identity matrix and, from Eq. (3.66),

$$[\boldsymbol{\omega}\times] = \begin{bmatrix} 0 & -\omega_e & 0 \\ \omega_e & 0 & 0 \\ 0 & 0 & 0 \end{bmatrix}. \tag{3.69}$$

The partial derivatives of the acceleration with respect to the velocity vector can also be derived as

$$\frac{\partial \ddot{\mathbf{r}}}{\partial \mathbf{v}^T} = -\frac{1}{2} C_D \frac{A}{m} \rho \left(\frac{1}{v_r} \mathbf{v}_r \mathbf{v}_r^T + v_r I_3 \right). \tag{3.70}$$

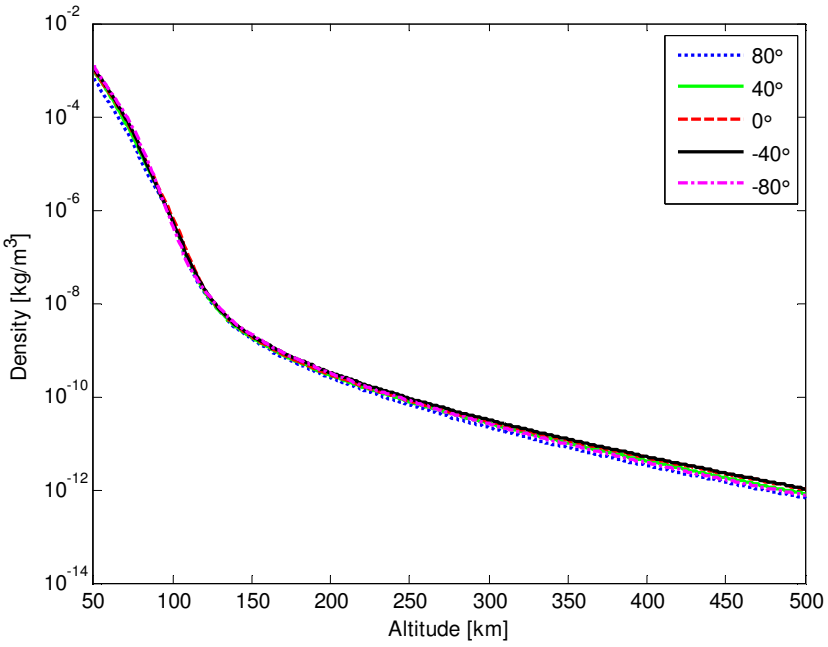

Figure 3.6 Density variation with altitude for different latitudes (longitude is 0°).

It should be mentioned that the partial derivative of the density with respect to the

position vector cannot be easily computed analytically. This is so because the atmospheric density models are very complex and, thus, difficult to be expressed as simple analytical functions. Therefore, this partial derivative should be computed by numerical differentiation (Montenbruck and Gill, 2001). The test results indicate that the numerical differentiation of the density for different positional variations makes only an insignificant difference (submillimeter level). This is so because the magnitude of density is small as compared to the magnitude of the position vector (see the ratio $\partial\rho/\partial\mathbf{r}^T$ in Eq. (3.68)) and it changes very smoothly at CHAMP altitude (see Figure 3.6); thus, it is not so sensitive to the position changes.

3.3.1.5 Empirical Forces

While the atmospheric modeling and estimation in the orbit determination procedure can considerably reduce the orbital errors, there still remain significant contributions of unmodeled forces; (in practice, there is no model that provides a totally correct description of a phenomenon that it represents). Therefore, a number of empirical functions can be used to absorb the variability of the nonconservative forces. A better approach is to estimate the pseudo-stochastic parameters which represent the magnitude of the frequent, instantaneous velocity changes as originally introduced as "wave filters" by Salychev and Schaffrin (1992). However, the empirical force modeling can also absorb the high-frequency effects, such as thrusters firing, during the orbit determination process. Since the radial direction is dynamically coupled with the along-track direction, it is not explicitly modeled in the orbit determination process to avoid the ill-conditioning of the system (Colombo, 2002; Boomkamp, 2004). Therefore, only the along-track and cross-track once-per-revolution components are estimated together with other parameters. The constant bias and the twice-per-revolution terms can also be modeled, depending on the type of satellites considered.

The periodic properties of the nonconservative (predominantly once-per-revolution and twice-per-revolution) forces can be clearly seen in Figures 3.7 and 3.8. Thus, the empirical force model can be expressed as a sum of sine and cosine terms in each direction:

$$\begin{aligned} \ddot{r}_{cross} &= C_c \cos(u) + S_c \sin(u) \\ \ddot{r}_{along} &= C_a \cos(u) + S_a \sin(u), \end{aligned} \tag{3.71}$$

with

C_c, S_c, C_a, S_a : the coefficients of sine and cosine in each direction;

u : the argument of latitude of the satellite.

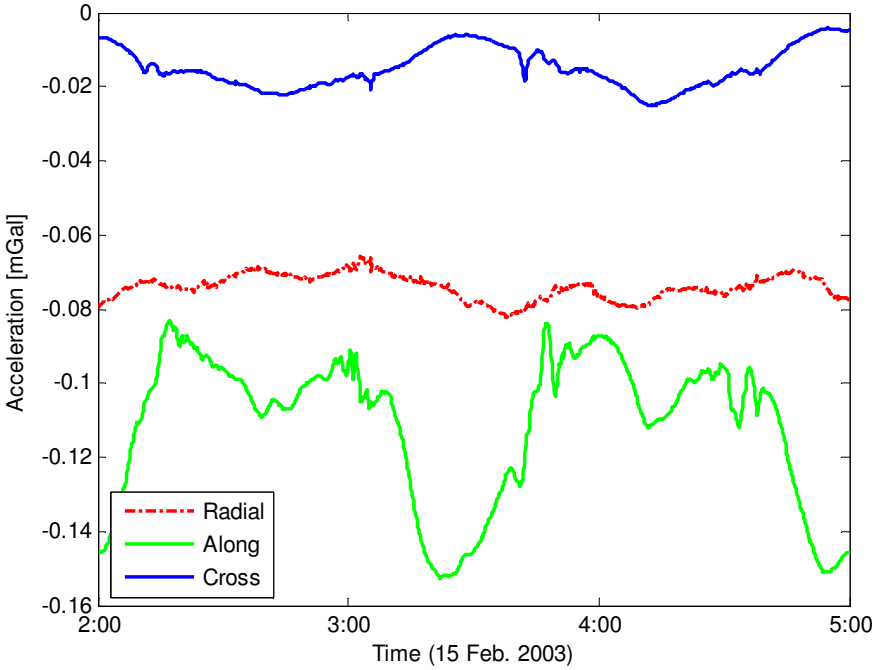

Figure 3.7 STAR accelerometer data of CHAMP (two revolutions).

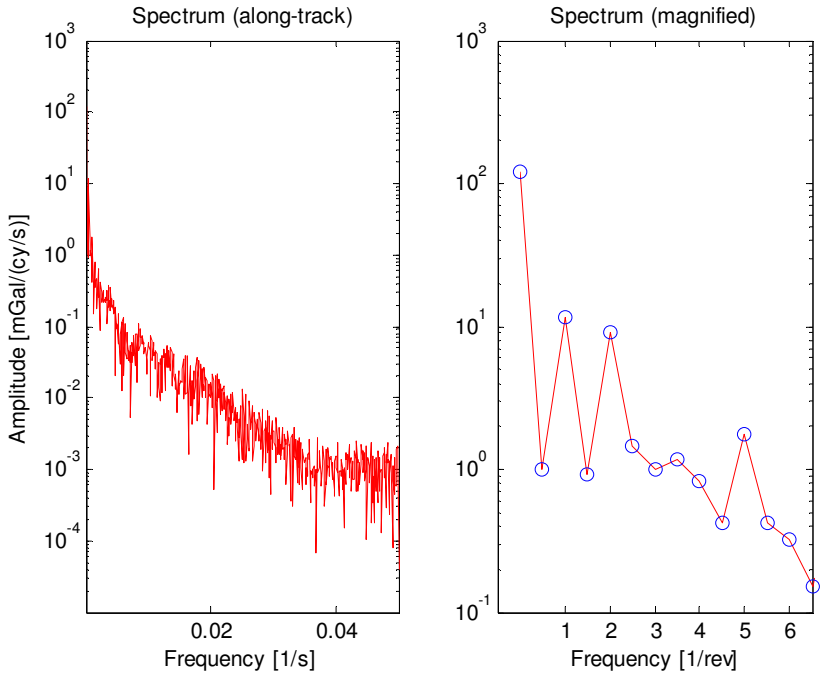

Figure 3.8 Fourier spectrum of STAR accelerometer data for CHAMP (along-track).

Since the empirical forces are modeled in the RTN (Radial/Transverse/Normal) frame, they should be transformed into an inertial frame to be combined with other accelerations. Assuming that the attitude of the spacecraft remains in the nominal in-flight direction (*i.e.*, the z-axis is nadir-looking and positive downward, the x-axis is aligned with the long side of the spacecraft towards the boom, and the y-axis completes the triad), the transformation matrix can be computed using the satellite inertial position and velocity, which is given as follows:

$$\ddot{\mathbf{r}}_{inertial} = \begin{bmatrix} \ddot{x} \\ \ddot{y} \\ \ddot{z} \end{bmatrix} = \begin{bmatrix} N_1 & T_1 & R_1 \\ N_2 & T_2 & R_2 \\ N_3 & T_3 & R_3 \end{bmatrix} \begin{bmatrix} \ddot{r}_{cross} \\ \ddot{r}_{along} \\ 0 \end{bmatrix}, \tag{3.72}$$

where the symbols are defined as

$$\mathbf{R} = \begin{bmatrix} R_1 & R_2 & R_3 \end{bmatrix}^T = \mathbf{r} / |\mathbf{r}|, \tag{3.73}$$

$$\mathbf{N} = \begin{bmatrix} N_1 & N_2 & N_3 \end{bmatrix}^T = \mathbf{v} \times \mathbf{R}, \tag{3.74}$$

$$\mathbf{T} = \begin{bmatrix} T_1 & T_2 & T_3 \end{bmatrix}^T = \mathbf{R} \times \mathbf{N} \tag{3.75}$$

with the position vector, $\mathbf{r}$, and the velocity vector, $\mathbf{v}$, of the satellite in an inertial frame. The partial derivatives of the acceleration with respect to the unknown coefficients are easily derived from Eq. (3.71) in the RTN frame, and these can be transformed into the inertial frame using the same matrix as given in Eqs. (3.72)-(3.75).

3.3.2 Parameter Estimation

As mentioned earlier, the initial state vector (position and velocity at the first epoch) and other dynamic parameters are estimated in the dynamic orbit determination. Since all measurements can be used to estimate these unknown parameters, it is justified to use the batch filter solution for the dynamic approach. Once the *a priori* information on the unknown parameters is available, for example, from the previous day estimation, the forces and the variational partials can be computed and integrated numerically to be propagated to the next epoch. This process continues to the last epoch of the batch, and the position and velocity as well as the integrated variational partials can then be stored in a file using a tabulated form.

The propagated position vector is used to evaluate the design matrix, H_k, at time t_k in Eq. (3.13), and it should be mapped back to the initial epoch of the batch using the

state transition matrix in order to parameterize the initial state vector. The state transition matrix is also obtained by numerical integration as explained in the next section. Let G be the range measurement between GPS satellite and the receiver onboard the LEO; it is represented by

$$G = \sqrt{(x^s - x_r)^2 + (y^s - y_r)^2 + (z^s - z_r)^2}\ , \tag{3.76}$$

where s and r indicate the GPS satellite and the receiver, respectively. Then the mapping of the design matrix back to the initial epoch can be represented by

$$\begin{aligned} O - G &= \frac{\partial G}{\partial \mathbf{r}_k^T}\frac{\partial \mathbf{r}_k}{\partial \mathbf{r}_0^T}d\mathbf{r}_0 + \frac{\partial G}{\partial \mathbf{r}_k^T}\frac{\partial \mathbf{r}_k}{\partial \dot{\mathbf{r}}_0^T}d\dot{\mathbf{r}}_0 + \frac{\partial G}{\partial \mathbf{r}_k^T}\frac{\partial \mathbf{r}_k}{\partial \mathbf{p}^T}d\mathbf{p} + \boldsymbol{v}_k \\ &= \frac{\partial G}{\partial \mathbf{r}_k^T}\begin{bmatrix} \dfrac{\partial \mathbf{r}_k}{\partial \mathbf{r}_0^T} & \dfrac{\partial \mathbf{r}_k}{\partial \dot{\mathbf{r}}_0^T} & \dfrac{\partial \mathbf{r}_k}{\partial \mathbf{p}^T} \end{bmatrix}\begin{bmatrix} d\mathbf{r}_0 \\ d\dot{\mathbf{r}}_0 \\ d\mathbf{p} \end{bmatrix} + \boldsymbol{v}_k\ , \end{aligned} \tag{3.77}$$

where O denotes a measurement, G represents a computed measurement using the known GPS position and the propagated LEO position at this time epoch. $\mathbf{r}$ and $\dot{\mathbf{r}}$ denote position and velocity vector, $\mathbf{p}$ is a dynamic parameter vector as before, and $\boldsymbol{v}_k$ is the random measurement error. The partial derivatives of the position vector at time t_k with respect to the unknown parameters (that is, $\partial \mathbf{r}_k / \partial \mathbf{r}_0^T$, $\partial \mathbf{r}_k / \partial \dot{\mathbf{r}}_0^T$, $\partial \mathbf{r}_k / \partial \mathbf{p}^T$) can be computed by integrating the following equations numerically to the next epoch, t_k:

$$\frac{\partial \ddot{\mathbf{r}}_{k-1}}{\partial \mathbf{r}_0^T} = \frac{\partial \ddot{\mathbf{r}}_{k-1}}{\partial \mathbf{r}_{k-1}^T}\frac{\partial \mathbf{r}_{k-1}}{\partial \mathbf{r}_0^T},\quad \frac{\partial \ddot{\mathbf{r}}_{k-1}}{\partial \dot{\mathbf{r}}_0^T} = \frac{\partial \ddot{\mathbf{r}}_{k-1}}{\partial \mathbf{r}_{k-1}^T}\frac{\partial \mathbf{r}_{k-1}}{\partial \dot{\mathbf{r}}_0^T},\quad \frac{\partial \ddot{\mathbf{r}}_{k-1}}{\partial \mathbf{p}^T} = \frac{\partial \ddot{\mathbf{r}}_{k-1}}{\partial \mathbf{r}_{k-1}^T}\frac{\partial \mathbf{r}_{k-1}}{\partial \mathbf{p}^T}, \tag{3.78}$$

where the first term on the right hand side of each equation (that is, $\partial \ddot{\mathbf{r}}_{k-1} / \partial \mathbf{r}_{k-1}^T$) is given in Chapter 3.3.1 (the partial derivatives for all forces should be summed up), and the second terms are being propagated from the initial conditions as will be explained in detail in the next section. Eq. (3.77) is further simplified into the form of a batch filter given in Eq. (3.14). The vector of the partial derivatives, $\partial G / \partial \mathbf{r}_k^T$, can be found in many references; see, e.g., Hofmann-Wellenhof et al. (2004, Chapter 9.4).

3.4 Reduced-Dynamic Modeling

The reduced-dynamic approach, which was initially developed at the Jet Propulsion Laboratory (Yunck et al., 1990 and 1994; Wu et al., 1991; Bertiger et al., 1994; Kuang et

al., 2001), resolved the weakness of the kinematic approach by combining the user dynamics with the geometric information and an appropriate weighting scheme according to the dynamic model quality while preserving the kinematic solution. The term "reduced-dynamic" was derived from the reduced susceptibility of the sequential process noise filter to dynamic model errors in comparison to the classical batch filter (Davis, 1996). The basic idea here is to introduce the kinematic components to the dynamic force models in the form of the process noise parameters (fictitious "accelerations" that compensate for the perturbations that are missing from the dynamic model); they are controlled by the *a priori* uncertainty, the steady-state uncertainty, and the correlation time. Thus, it is considered as a fast and efficient method, especially for real-time applications.

In the post-processed reduced-dynamic approach, the dynamic parameters are estimated first, and then the state vector is estimated again using the Kalman sequential filter along with the stochastic process noise which is usually modeled as first-order Gauss-Markov process. The process noise level and the correlation time can be chosen from the analysis of the overlapping orbit solutions in the process of filter tuning (Kuang et al., 2001). This operation must be "customized" for each satellite or constellation separately. According to Wu et al. (1991), the satellites at altitudes 400 km to 2000 km will receive the greatest benefit from the reduced-dynamic approach.

While the dynamic orbit is generally estimated by the batch least-squares adjustment methods, the reduced-dynamic approach is based on the Kalman sequential filtering algorithm. In this method, the estimates are propagated using the state transition matrix, and then the propagated estimates are updated by the measurement at each epoch; thus, this method is usually chosen for (near) real-time applications. In order to bring the Kalman sequential filtering technique into practice, one must assume that the estimated system state vector $\tilde{\boldsymbol{x}}_k$ contains all the information accumulated by the system up to the time epoch t_k (Jekeli, 2001). This means that, once the current state vector is known (estimated), the system state cannot be improved by any state vector prior to this epoch, which can be expressed by

$$\mathcal{P}\left(\boldsymbol{x}_{k+1} \mid \tilde{\boldsymbol{x}}_k, \tilde{\boldsymbol{x}}_{k-1}, \cdots, \tilde{\boldsymbol{x}}_0\right) = \mathcal{P}\left(\boldsymbol{x}_{k+1} \mid \tilde{\boldsymbol{x}}_k\right), \tag{3.79}$$

where $\mathcal{P}$ denotes the conditional probability density. Moreover, the statistics of the observation vector at the current epoch, $\boldsymbol{y}_k$, are independent of all the previous observations in the case where the current state vector is given:

$$\mathcal{P}\left(\boldsymbol{y}_k \mid \tilde{\boldsymbol{x}}_k, \boldsymbol{y}_{k-1}, \cdots, \boldsymbol{y}_1\right) = \mathcal{P}\left(\boldsymbol{y}_k \mid \tilde{\boldsymbol{x}}_k\right). \tag{3.80}$$

3.4.1 Error Dynamics Equation

Let $\mathbf{r}_{3\times1} = \begin{bmatrix} x & y & z \end{bmatrix}^T$, $\mathbf{v}_{3\times1} = \begin{bmatrix} v_x & v_y & v_z \end{bmatrix}^T$ be the position and velocity vector of a satellite at an arbitrary epoch, respectively, and $\mathbf{p}_{r\times1} = \begin{bmatrix} p_1 & p_2 & \cdots & p_r \end{bmatrix}^T$ be the vector of dynamic parameters, for example, the atmospheric drag coefficients. Then, the total error dynamics as a set of the first-order linear differential equations can be represented by

$$\frac{d}{dt}\begin{bmatrix} \delta\mathbf{r} \\ \delta\mathbf{v} \\ \delta\mathbf{p} \end{bmatrix} = \begin{bmatrix} \mathbf{0}_{3\times3} & I_3 & \mathbf{0}_{3\times r} \\ \left[\frac{\partial\ddot{\mathbf{r}}}{\partial\mathbf{r}^T}\right]_{3\times3} & \left[\frac{\partial\ddot{\mathbf{r}}}{\partial\mathbf{v}^T}\right]_{3\times3} & \left[\frac{\partial\ddot{\mathbf{r}}}{\partial\mathbf{p}^T}\right]_{3\times r} \\ \mathbf{0}_{r\times3} & \mathbf{0}_{r\times3} & \mathbf{0}_{r\times r} \end{bmatrix}\begin{bmatrix} \delta\mathbf{r} \\ \delta\mathbf{v} \\ \delta\mathbf{p} \end{bmatrix}, \tag{3.81}$$

with

δ: the differential operator (assuming that the operators δ and d/dt are interchangeable);
I_3: the 3×3 identity matrix;
$\mathbf{0}_{n\times m}$: the $n\times m$ matrix of zeros;
$\ddot{\mathbf{r}}_{3\times1}$: the acceleration vector of the satellite at the chosen epoch.

The partial derivatives of the satellite acceleration with respect to the position, velocity and other dynamic parameters (*i.e.*, $\partial\ddot{\mathbf{r}}/\partial\mathbf{r}^T$, $\partial\ddot{\mathbf{r}}/\partial\mathbf{v}^T$ and $\partial\ddot{\mathbf{r}}/\partial\mathbf{p}^T$) can be formulated by the variational partials with the inclusion of the explicit part for the velocity and the dynamic parameters (same as in the dynamic approach).

The total error dynamics equation can be further simplified as

$$\dot{\boldsymbol{x}}(t) = A(t)\boldsymbol{x}(t), \tag{3.82}$$

where $A(t)$ is the coefficient matrix for the dynamics equation, and $\boldsymbol{x}(t)$ is the incremental state deviation vector which is given by the difference between the true trajectory, $\boldsymbol{X}(t)$, and the reference trajectory, $\boldsymbol{X}^*(t)$, that is,

$$
\begin{aligned}
\boldsymbol{x}(t) &= \begin{bmatrix} \delta\mathbf{r}^T & \delta\mathbf{v}^T & \delta\mathbf{p}^T \end{bmatrix}^T \\
&= \boldsymbol{X}(t) - \boldsymbol{X}^*(t) \\
&= \begin{bmatrix} \left(\mathbf{r}-\mathbf{r}^*\right)^T & \left(\mathbf{v}-\mathbf{v}^*\right)^T & \left(\mathbf{p}-\mathbf{p}^*\right)^T \end{bmatrix}^T .
\end{aligned} \tag{3.83}
$$

The general solution of Eq. (3.82) for a given initial vector $\boldsymbol{x}_k = \boldsymbol{x}(t_k)$ can be represented by

$$
\boldsymbol{x}(t) = \Phi(t, t_k)\boldsymbol{x}_k , \tag{3.84}
$$

where $\boldsymbol{x}_k$ is the state vector at time t_k, and the matrix $\Phi(t, t_k)$, known as the state transition matrix, connects the state vectors between the two time epochs t_k and t. Some useful properties of the state transition matrix can easily be shown via Eqs. (3.82) and (3.84):

$$
\begin{aligned}
&\Phi(t_i, t_i) = I \\
&\Phi(t_k, t_i) = \Phi(t_k, t_j)\Phi(t_j, t_i) \\
&\Phi(t_k, t_i) = \Phi^{-1}(t_i, t_k) \\
&\frac{d}{dt}\left[\Phi^{-1}(t_k, t_i)\right] = -\Phi^{-1}(t_k, t_i)A(t_k) .
\end{aligned} \tag{3.85}
$$

For the computation of the state transition matrix $\Phi(t, t_k)$, one can combine Eqs. (3.82) and (3.84) to obtain the following condition:

$$
\dot{\boldsymbol{x}}(t) = \dot{\Phi}(t, t_k)\boldsymbol{x}_k = A(t)\Phi(t, t_k)\boldsymbol{x}_k , \tag{3.86}
$$

which should be satisfied for any state vector at time t_k. Thus, the following differential equation for $\Phi(t, t_k)$ can be arrived at:

$$
\dot{\Phi}(t, t_k) = A(t)\Phi(t, t_k) \tag{3.87}
$$

with the initial conditions

$$
\Phi(t_k, t_k) = I . \tag{3.88}
$$

Expressing Eq. (3.87) element-wise demonstrates that the columns of the

derivatives of the state transition matrix are independent of each other in that the first column of $\dot{\Phi}(t,t_k)$ does not contain elements of $\Phi(t,t_k)$ from the second column (Lundberg, 1984; Tapley et al., 2004). In other words, the coefficient matrix for the dynamics equation (see Eq. (3.81)) can be simplified to

$$A=\begin{bmatrix}\mathbf{0}_{3\times3} & I_3 & \mathbf{0}_{3\times r}\\ B_{3\times3} & C_{3\times3} & D_{3\times r}\\ \mathbf{0}_{r\times3} & \mathbf{0}_{r\times3} & \mathbf{0}_{r\times r}\end{bmatrix} \tag{3.89}$$

by renaming the blocks in the second row. Also, the state transition matrix can be partitioned into sub-matrices of the same dimension as A:

$$\Phi=\begin{bmatrix}\phi_1 & \phi_2 & \phi_3\\ \phi_4 & \phi_5 & \phi_6\\ \phi_7 & \phi_8 & \phi_9\end{bmatrix}. \tag{3.90}$$

Then Eq. (3.87) becomes

$$\begin{bmatrix}\dot{\phi}_1 & \dot{\phi}_2 & \dot{\phi}_3\\ \dot{\phi}_4 & \dot{\phi}_5 & \dot{\phi}_6\\ \dot{\phi}_7 & \dot{\phi}_8 & \dot{\phi}_9\end{bmatrix}=\begin{bmatrix}\phi_4 & \phi_5 & \phi_6\\ B\phi_1+C\phi_4+D\phi_7 & B\phi_2+C\phi_5+D\phi_8 & B\phi_3+C\phi_6+D\phi_9\\ 0 & 0 & 0\end{bmatrix}. \tag{3.91}$$

From Eq. (3.91), three components ϕ_7, ϕ_8 and ϕ_9 are constant at all times, a result equivalent to the initial condition in Eq. (3.88) where, $\phi_7=\phi_8=0$ and $\phi_9=I$. The upper two rows of Eq. (3.91) can be represented by three second-order differential equations:

$$\begin{aligned}\ddot{\phi}_1&=B\phi_1+C\phi_4,\\ \ddot{\phi}_2&=B\phi_2+C\phi_5,\\ \ddot{\phi}_3&=B\phi_3+C\phi_6+D,\end{aligned} \tag{3.92}$$

for which the initial conditions are obtained from Eq. (3.88)

$$\begin{bmatrix} \phi_1 & \phi_2 & \phi_3 \\ \dot{\phi}_1 & \dot{\phi}_2 & \dot{\phi}_3 \end{bmatrix} = \begin{bmatrix} I & 0 & 0 \\ 0 & I & 0 \end{bmatrix} \tag{3.93}$$

with the relation of $\phi_4 = \dot{\phi}_1$, $\phi_5 = \dot{\phi}_2$ and $\phi_6 = \dot{\phi}_3$.

Therefore, the numerical integrator solves the second-order differential equation of the forces acting on the satellite for the position and velocity of the satellite and, at the same time, the second-order differential equation of Eq. (3.92) is used to obtain the state transition matrix between epochs. The position and velocity obtained from the numerical integrator are again used to evaluate the coefficient matrix, $A(t)$, as seen in Eq. (3.81).

3.4.2 Numerical Considerations

As can be seen in Eq. (3.41), the *a posteriori* mean squared error matrix is always smaller than that of the *a priori* mean squared error matrix (notice that a positive-definite matrix is subtracted there), no matter what observations are used. This could mean that the estimation procedure finally becomes insensitive to further measurements. In this case, the filter diverges due to the dynamic model errors. The process noise, as implemented in this study, plays the role of overcoming this problem. Other types of process noise modeling, such as Dynamic Model Compensation (DMC), for instance, are also used in the orbit determination problem (Tapley and Ingram, 1973; Davis, 1996; Cruickshank, 1998).

The first expression of Eq. (3.41) can fail to yield a symmetric positive-definite matrix; thus, the second equation is sometimes used instead. Even if the symmetric form of the mean squared error matrix is used, it is worth forcing its computed version to be symmetric by replacing it with its "symmetric kernel" as follows:

$$P_k^- = \frac{1}{2}\left(P_k^- + (P_k^-)^T\right), \quad P_k = \frac{1}{2}\left(P_k + P_k^T\right). \tag{3.94}$$

While the numerical stability will be similar for both the batch and the sequential filtering, multiple iterations are needed for the system convergence in the batch filtering, because of the nonlinearity between the measurements and the state parameters. The Kalman sequential filter, however, generally does not need to iterate because the reference solution is changed with each new observation. It should be kept in mind that there could be a problem in the case of large deviations between the *a priori* state and the actual state, as well as in the case of a poor management of the mean squared errors. Also, if the covariance matrix for the process noise is too large, it will allow larger measurement errors to be accepted.

CHAPTER 4

NETWORK OPTIMIZATION

Kinematic orbit determination of LEO satellites, as pointed out in Chapter 3, can only be guaranteed by the quality and continuity of GPS data, and the geometry between the GPS satellites and the LEO. Therefore, a pseudolite transceiver network is proposed as one of the methods to strengthen the constellation geometry of the positioning satellites. Although the PL hardware can theoretically be installed onboard LEOs, the optimization problem of the network is restricted only to the ground stations. The issue addressed here concerns the definition and implementation of an optimal configuration of the ground stations where the PLs should be located. Since it can be assumed that the LEO satellite orbits the Earth almost uniformly (a repeat period of ~15 days), the problem can be redefined as "*How does one optimally design the PL station network independent of the position of LEO satellites?*" Of course, this network optimization problem can be applied to both the augmentation of PLs and the selection of the ground stations for GPS differential positioning. In an ideal case, it is a matter of determining the position where the network stations should be. However, since most of the Earth surface is covered by water, a totally uniform design is impossible, and the existing ground stations, such as the IGS stations, should be selected for convenience.

4.1 Optimization Theory

4.1.1 Optimal Network Design

The optimal network criteria can be composed of three components, *i.e.*, *precision*, *reliability*, and *costs*. Since these three components are related to each other, this problem can be handled as a multi-purpose optimization problem as discussed in Schaffrin (1985):

$$\alpha_p \cdot (precision) + \alpha_r \cdot (reliability) + \alpha_c \cdot (costs)^{-1} = \max., \tag{4.1}$$

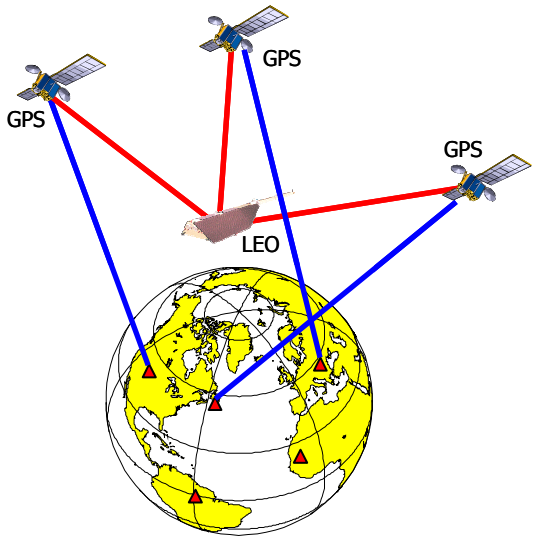

Figure 4.1 Constellation geometry of the positioning satellites, LEO, and ground tracking stations.

where α_p, α_r and α_c are chosen weight coefficients. However, this approach is not very effective because it depends on the choice of the weight coefficients. Therefore, it is generally recommended that one deals with precision, while keeping reliability and costs under control.

Grafarend (1972) proposed the requirements of the ideal network; *homogeneity* and *isotropy* of its point errors. Homogeneity means that there is invariance with respect to a translation in space, and isotropy represents the invariance with respect to a rotation. Under these properties, a uniform quality of the network can be achieved, resulting in circular/spherical local error ellipses/ellipsoids of equal size. A variance-covariance matrix which is homogeneous and isotropic in an ideal network (called a "criterion matrix") possesses the Taylor-Karman structure (TK-structure), which defines the covariance of the phenomenon (point errors) between two points. The TK-structure will be discussed in detail in the next section. Also, since the measurement type is not specified, this criterion matrix is independent of any linear models with specific rank-deficiency.

An optimal design problem can be considered as a process on the cofactor matrix. This can be categorized into four approaches: Zero Order Design (ZOD), First Order Design (FOD), Second Order Design (SOD), and Third Order Design (TOD) (Grafarend, 1974; Schaffrin, 1985). ZOD optimizes the cofactor matrix by varying the datum choice based on the best possible similarity to the chosen criterion matrix. FOD uses the varying design matrix, which is valid only in the domain of linearization. SOD determines the weights of the measurements to generate optimal results; therefore, this will be emphasized in this study. TOD is similar to the SOD except that the weights of additional

measurements are sought for the improvement of the existing cofactor matrix.

4.1.2 Taylor-Karman Structure

The Taylor-Karman structure defines the auto- and cross-covariances of a phenomenon between two points in the network. The distance between two points P_i and P_j is defined as

$$s := \left|\mathbf{r}_i - \mathbf{r}_j\right| = \sqrt{(x_i - x_j)^2 + (y_i - y_j)^2 + (z_i - z_j)^2}\,, \tag{4.2}$$

where $\mathbf{r}_i = (x_i, y_i, z_i)^T$ and $\mathbf{r}_j = (x_j, y_j, z_j)^T$ represent the Cartesian coordinates of P_i and P_j, respectively. Following Grafarend (1972), the general expression for the TK-structured criterion matrix between P_i and P_j is given by

$$C_{ij} := \begin{bmatrix} \Sigma_m(s) & 0 & 0 \\ 0 & \Sigma_m(s) & 0 \\ 0 & 0 & \Sigma_m(s) \end{bmatrix}_{3\times 3} + \left[\Sigma_l(s) - \Sigma_m(s)\right] \cdot \frac{1}{s^2}\left[(\mathbf{r}_i - \mathbf{r}_j)(\mathbf{r}_i - \mathbf{r}_j)^T\right]_{3\times 3}, \tag{4.3}$$

where C_{ij} denotes the ideal cofactor matrix of the estimated network points P_i and P_j, $\Sigma_l(s)$ and $\Sigma_m(s)$ represent the longitudinal- and cross-covariance functions, respectively. If the points P_i and P_j coincide, the two covariance functions have the same value, *i.e.*,

$$\Sigma_m(0) = \Sigma_l(0) = \sigma^2, \tag{4.4}$$

where σ^2 is the expected or desired variance of the estimated coordinates of the network (1 dm^2 is used here). The correlation function of an autoregressive process of the first order is given by (Grafarend and Schaffrin, 1979; Schaffrin, 1985)

$$\Sigma(s) = \frac{1}{2}\left[\Sigma_m(s) + \Sigma_l(s)\right] = \sigma^2 \cdot \left(\frac{s}{d}\right) \cdot K_1\left(\frac{s}{d}\right), \tag{4.5}$$

where K_1 is the modified Bessel function of the second kind and first order, s is the distance between two points, and d is the characteristic distance of the network, which has not yet been determined clearly. Two feasible choices for the characteristic distance

are suggested:

1) d should be chosen smaller than the minimum baseline in the network (Schmitt, 1980);
2) the maximum distance of the network is an upper bound for 10d (Wimmer, 1982).

For the "potential type," additional conditions are required to distinguish the longitudinal- and cross-covariance functions

$$\Sigma_l(s) = \frac{d}{ds}\Sigma_m(s), \qquad \Sigma_m(s) = \frac{2}{s^2}\int_0^s x\Sigma(x)\,dx\,. \tag{4.6}$$

In order to calculate the covariance functions, Eq. (4.6) should be evaluated in advance, which is somewhat complicated. Instead, by assuming a 2-D Markov process of the first order, Grafarend and Schaffrin (1979) provided analytical formulas for the two covariance functions, namely,

$$\frac{1}{\sigma^2}\Sigma_l(s) = -\frac{4d^2}{s^2} + 2K_0(s/d) + \frac{4d}{s}K_1(s/d) + 2\frac{s}{d}K_1(s/d)\,, \tag{4.7}$$

$$\frac{1}{\sigma^2}\Sigma_m(s) = +\frac{4d^2}{s^2} - 2K_0(s/d) - \frac{4d}{s}K_1(s/d)\,, \tag{4.8}$$

with

K_0: the modified Bessel function of the second kind and zero order;
K_1: the modified Bessel function of the second kind and first order.

Figure 4.2 illustrates the longitudinal- and cross-covariance functions. The covariance functions are mostly decreasing with the distance between two points. As s/d gets closer to 10 (*i.e.*, as the baseline length approaches ten times that of the characteristic distance), the two points become almost decorrelated. That is the basic idea as suggested by Wimmer (1982).

Once the criterion matrix is designed, the weights of each measurement between stations can be computed from the SOD approach. In the SOD the difference between the cofactor matrix of the estimated point coordinates in $\hat{\xi}$, that is, $Q_{\hat{\xi}}$, and an ideal criterion matrix (e.g., with TK-structure), C, will be minimized by varying the weights:

$$\left\| Q_{\hat{\xi}} - C \right\| = \min\,. \tag{4.9}$$

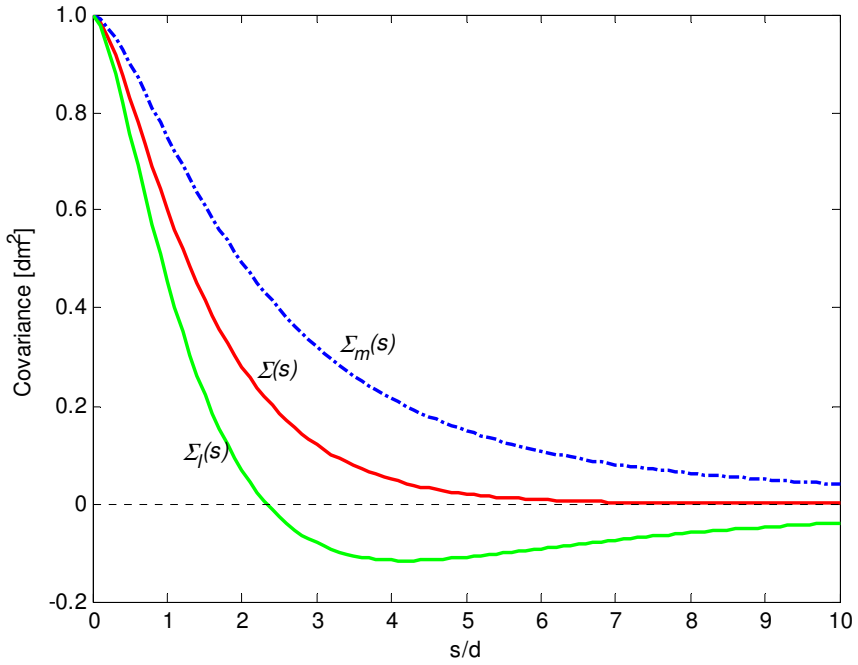

Figure 4.2 Longitudinal- and cross-covariance functions.

Assuming uncorrelated observations in a Gauss-Markov model, $y = A\xi + e,\ e \sim (0, \sigma_0^2 P^{-1})$, this condition can be transformed into

$$\left\| A^T PA - C^{-1} \right\| = \min_{P:=diag\,\mathbf{p}}, \tag{4.10}$$

where C is a criterion matrix with TK-structure and $\mathbf{p}$ is the vector of diagonal elements of the weight matrix P. Using an appropriate operator and a weighted l^2-norm, Eq. (4.10) becomes

$$\left\| (A^T \odot A^T)\mathbf{p} - vecC^{-1} \right\|^2_{C\otimes C} = \min_{\mathbf{p}=vecdiagP}, \tag{4.11}$$

where *vecdiag* represents an operator which vectorize the diagonal elements of a matrix. The symbol $\odot$ denotes the *Khatri-Rao product* which is defined as

$$\underbrace{A \odot B}_{nl\times m} = [\alpha_1 \otimes \beta_1, \quad \cdots, \quad \alpha_m \otimes \beta_m], \tag{4.12}$$

for two matrices $A_{n\times m} = [\alpha_1, \quad \cdots, \quad \alpha_m]$ and $B_{l\times m} = [\beta_1, \quad \cdots, \quad \beta_m]$ with the same

number of columns, while $\otimes$ denotes the *Kronecker-Zehfuss product* defined by

$$\underset{n\times m}{G}\otimes\underset{p\times q}{H}=[g_{ij}\cdot H]_{pn\times qm}. \tag{4.13}$$

After some manipulation of Eq. (4.11), the normal equations for the weights are given by

$$\left[(A^T\odot A^T)^T(C\otimes C)(A^T\odot A^T)\right]\hat{\mathbf{p}}=(A^T\odot A^T)^T\underbrace{(C\otimes C)vecC^{-1}}_{vecC}, \tag{4.14}$$

and finally by

$$(ACA^T*ACA^T)\hat{\mathbf{p}}=vecdiag(ACA^T), \tag{4.15}$$

where the symbol $*$ now defines the *Hadamard product* of matrices with equal size, namely,

$$\underset{k\times l}{G}*\underset{k\times l}{H}=[g_{ij}\cdot h_{ij}]_{k\times l}. \tag{4.16}$$

For more details concerning the above matrix products, see Schaffrin (1985, Appendix 2).

4.1.3 Sequential Algorithm for Finding the Optimal Network Configuration

In order to find optimal stations from the candidate group, the algorithm starts from one station and keeps adding one station at a time, which satisfies the optimality criterion at each selection step. The first station could be anywhere in the network, and the final set of stations will be different depending on the first station. However, the resulting set should always satisfy the requirements, *i.e.*, be approximately homogeneous and isotropic. The station selection procedure can be summarized as follows (see Figure 4.3):

1) Choose one station from the stations list as the 1st station of the network. Although different choices of the 1st station will provide different resulting sets, the error situation is expected to be approximately uniform.

2) Find the 2nd station, which has the maximum distance from the 1st station. This maximum distance will serve as an upper limit of the characteristic distance for the computation of the covariance functions. This also gives an optimal network for the case of two stations.

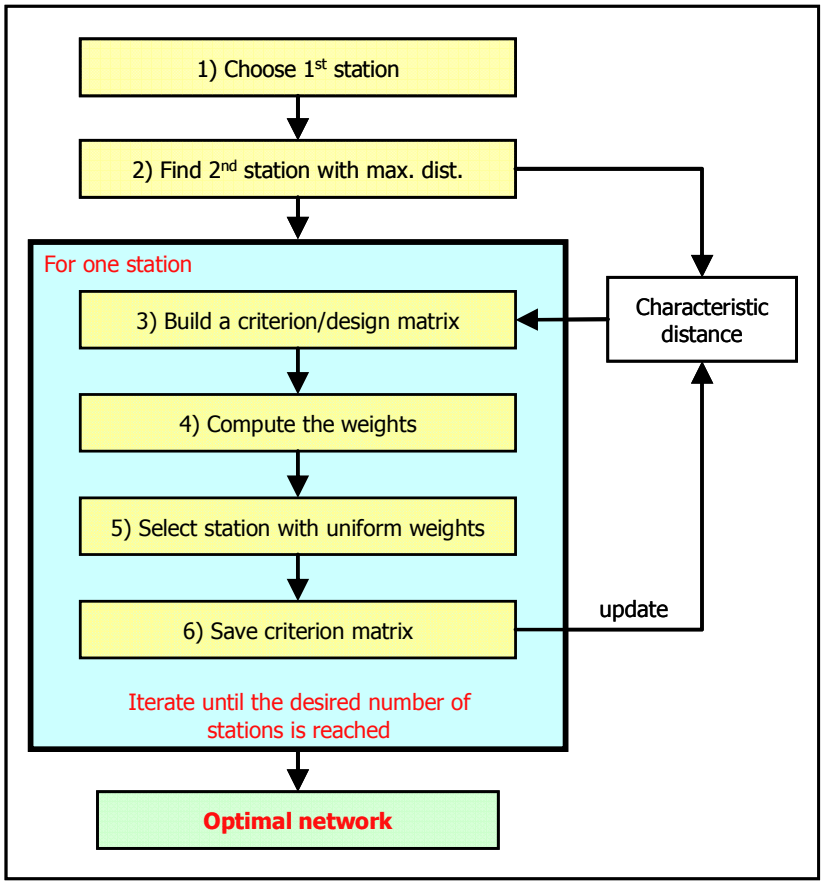

Figure 4.3 Flow chart of the algorithm for optimal network selection.

3) Build a criterion matrix for two network stations. This criterion matrix will be used in the next step of the selection process. It should be mentioned that a criterion matrix will be almost the identity matrix if the characteristic distance is smaller than the minimum baseline in the network, because the minimum baseline is quite small if compared to other baselines. Therefore, it would be better to use one tenth of the maximum baseline as an upper limit of the characteristic distance according to Wimmer (1982).

4) Compute the weights of all combinations of 'network-to-candidate station' baselines. This can be done using Eq. (4.15). The criterion matrix is continuously accumulated up to the last network station. For example, for the j^{th} network station, the $3(j-1)\times 3(j-1)$ criterion matrix will be reused for the $3j\times 3j$ criterion matrix of the current candidate station. The number of rows of the design matrix will be the same as the number of network stations because no further measurements between existing network stations are assumed.

5) Find the station that has the most uniform weights to all network stations by computing the Root Mean Square (RMS) deviations of weights. Since the weight of a short baseline is larger than that of a long baseline, and the stations need to be as wide-spread as possible for the optimal configuration, the station which has the minimum RMS deviation of weights is chosen as the next network station. Once a station is added to the network, it is removed from the candidate group.

6) Save the criterion matrix up to the newly chosen network station and update the maximum and characteristic distance in the network for the next step of the selection process.

7) Repeat steps 4)-6) until the desired number of stations is reached.

4.2 Network Optimization for LEO Orbit Determination

For the application of the optimal network design technique, as investigated in this study, a total of 269 IGS tracking network stations are prepared; see http://itrf.ensg.ign.fr/ITRF_solutions/2000/results/ITRF2000_GPS.SSC.txt. All coordinates are computed at epoch 2004.0 by applying the velocity information. As can be seen in the figure illustrating the network stations (Figure 4.4), the distribution of stations is denser in North America and Western Europe, while fewer stations are available in Africa, South America and Antarctic area.

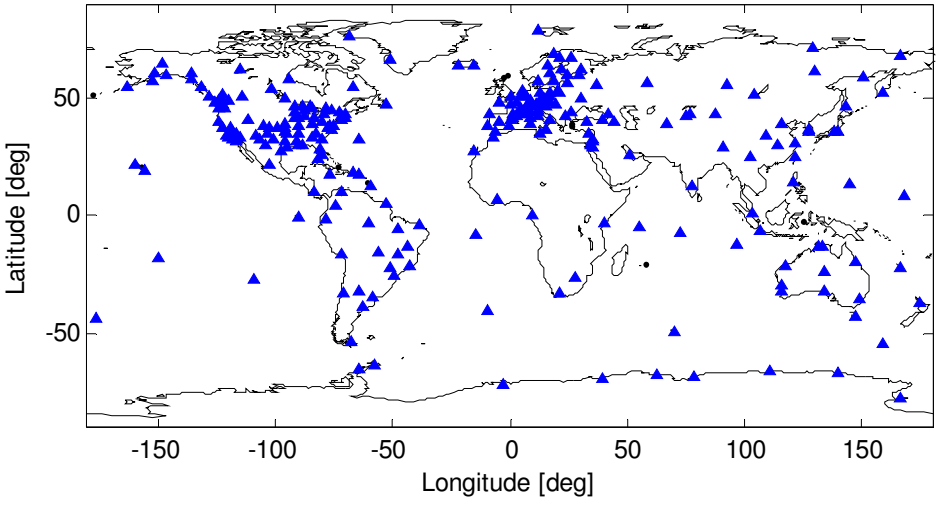

Figure 4.4 IGS network stations used (269 stations).

It should be mentioned here that distance measurements between two stations are used as observations. Although any kind of measurement (direction, distance, distance ratio or angular observations, etc.) can be used, only distance measurements are introduced here for the optimal network design, because, in fact, GPS observations are used for the LEO orbit determination process. Without the loss of generality, it is possible to use different types of measurements for a network design for different purposes. It is assumed that only the measurements between one additional candidate station and the already selected network stations are considered, as only one candidate station is added at a time. Once a station is added to the network, this set of stations is optimal for the case of that specific number of stations.

Figure 4.5 shows the result of the optimized network. The numbers in the figure represent the sequence in the selection process. The first chosen station is ALBH in North America (marked as blue circle), and the 2nd one, KERG, is on the opposite hemisphere to station 1. Although a large number of stations are concentrated in North America and Western Europe, a few of them are chosen in the final result, ensuring generation of a network of greater uniformity.

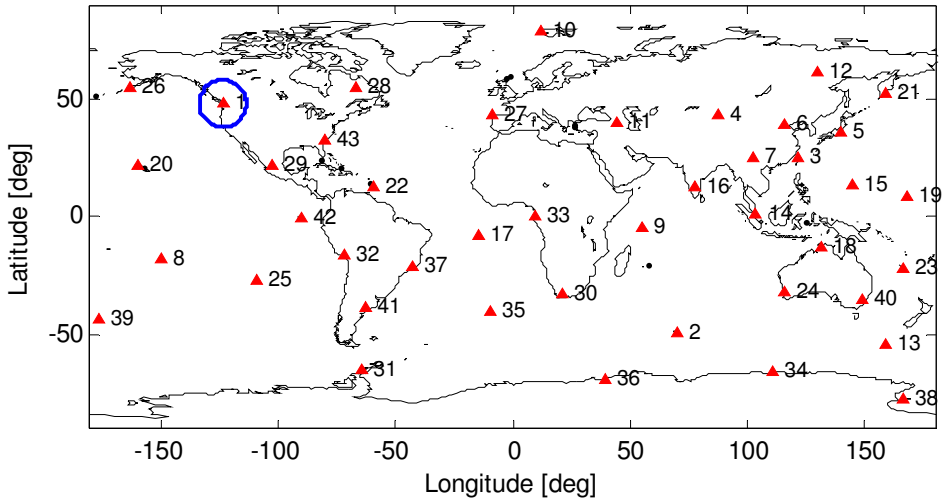

Figure 4.5 Selected stations using the optimal selection process (43 stations).

Since the goal of the optimal network design is to make the cofactor matrix of the estimated point coordinates, $Q_{\hat{\xi}}$, as close to the criterion matrix as possible, the cofactor matrix should be computed using the estimated weights for each baseline. However, in spite of numerous advantages of the Gauss-Markov model for geodetic networks, such as easily programmable computer calculation, the covariance matrix of the parameter estimates as a byproduct, and easily understandable results (Caspary, 1987), the conventional geodetic networks experience certain datum deficiencies. In 3-D networks with distance measurements, the rank deficiency is 6 (3 translations and 3 rotations).

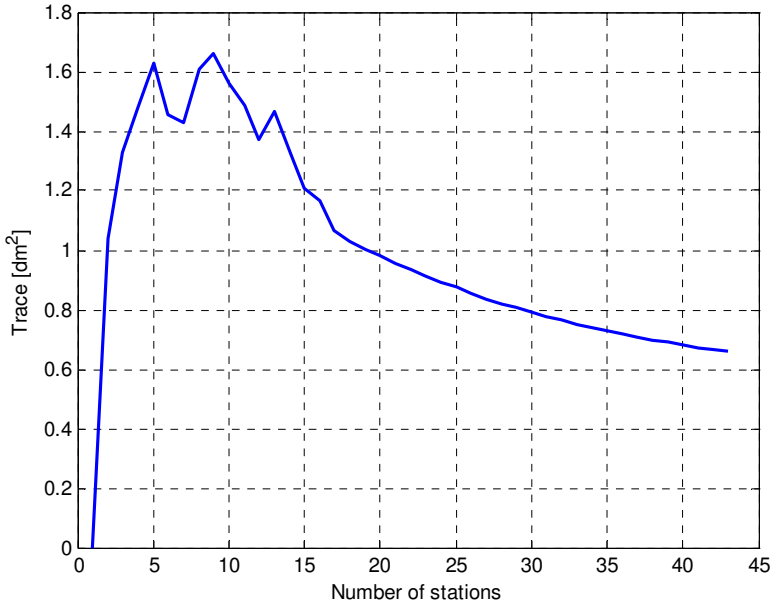

Figure 4.6 Relative trace of the cofactor matrix.

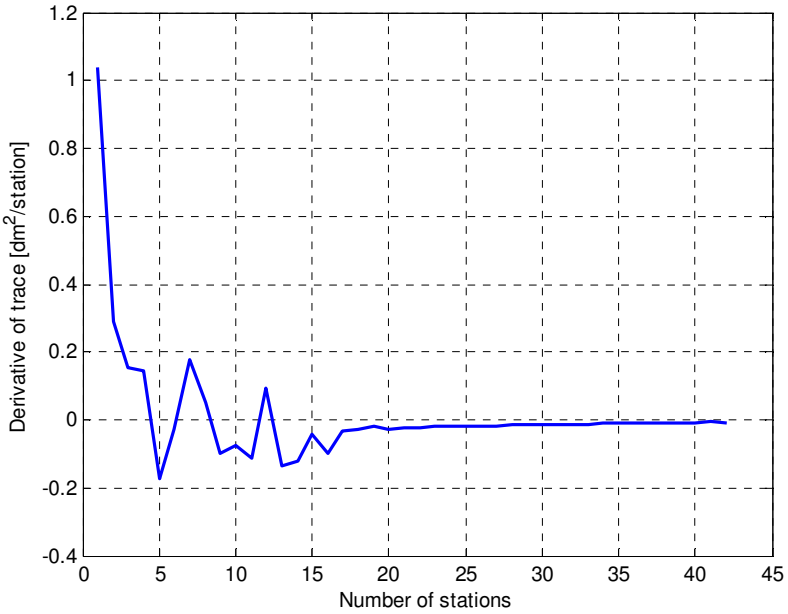

Figure 4.7 Derivative of the relative trace of the cofactor matrix.

Therefore, the resulting normal matrix also has a rank deficiency and the standard matrix inversion is not possible. Instead of a standard inversion, *the pseudoinverse* can be used for the computation of the cofactor matrix, for instance by using the Singular Value Decomposition (SVD) method (Strang and Borre, 1997).

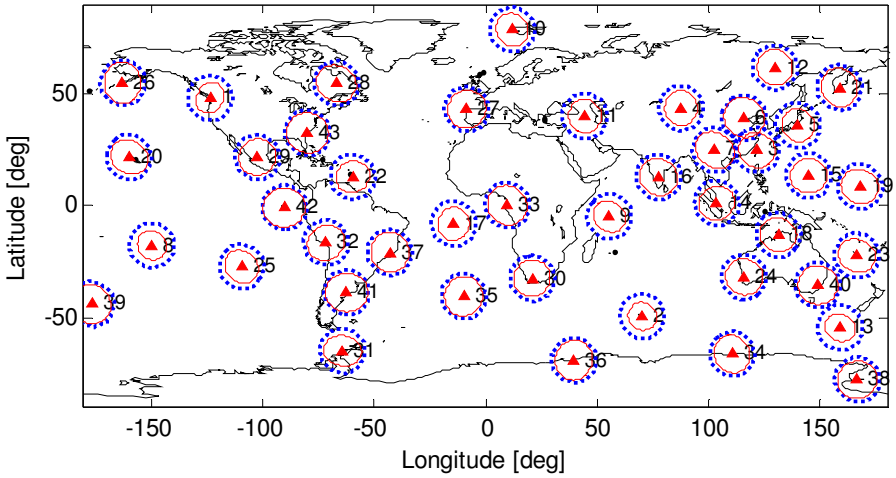

Figure 4.8 Error ellipses of the optimal network.

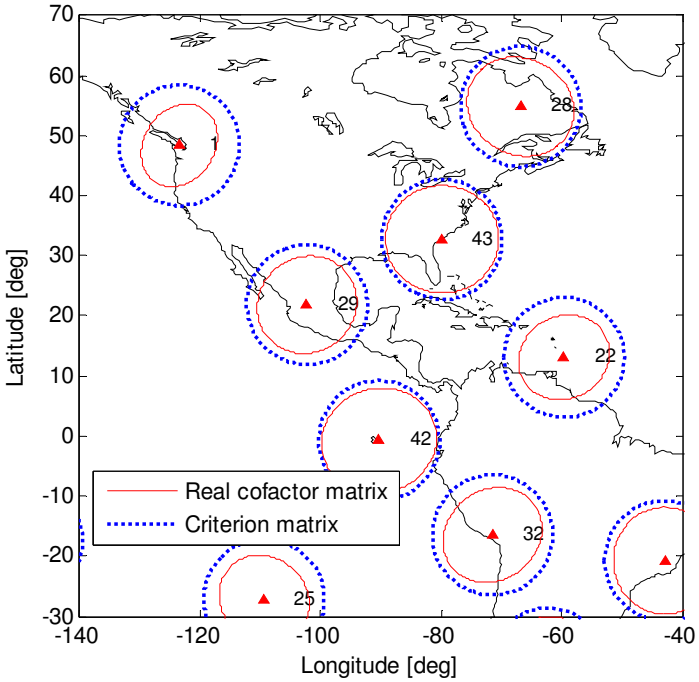

Figure 4.9 Error ellipses of the optimal network (magnified in North America).

Figures 4.6 and 4.7 show the measure of optimality. Figure 4.6 represents the scaled trace of the cofactor matrix, and Figure 4.7 is a finite "derivative" of Figure 4.6 by depicting the improvement of the trace per additional station. It should be mentioned that the trace of the cofactor matrix is averaged by the number of nonzero eigenvalues. As can be seen in Figure 4.7, there is practically no improvement beyond 40 stations.

Figures 4.8 and 4.9 illustrate the error ellipses in the local plane. These figures are plotted with the same scale in both latitude and longitude directions; thus, the requirements of the optimal network, *i.e.*, homogeneity and isotropy, can be clearly seen in the results.

To compute the error ellipses in the local plane, the cofactor matrix in the Cartesian coordinate system should be transformed into the local plane using the relation given by (Hofmann-Wellenhof et al., 2004)

$$\left(Q_{\hat{\xi}}\right)_{neu} = R\left(Q_{\hat{\xi}}\right)_{xyz} R^T, \tag{4.17}$$

where R is a rotation matrix from the Cartesian to the local-level system (North-East-Up), see Leick (1995):

$$\begin{bmatrix}\Delta n & \Delta e & \Delta u\end{bmatrix}^T = R \cdot \begin{bmatrix}\Delta x & \Delta y & \Delta z\end{bmatrix}^T, \tag{4.18}$$

where R is defined by

$$R = \begin{bmatrix} -\sin\varphi\cos\lambda & -\sin\varphi\sin\lambda & \cos\varphi \\ -\sin\lambda & \cos\lambda & 0 \\ \cos\varphi\cos\lambda & \cos\varphi\sin\lambda & \sin\varphi \end{bmatrix} \tag{4.19}$$

with the latitude (φ) and longitude (λ) given as the geodetic station coordinates.

Table 4.1 explains how well the result follows the requirements of the optimal network. $\lambda_{\max}$ and $\lambda_{\min}$ represent the semi-major and semi-minor axes of the error ellipses, respectively, the square of which corresponds to the maximum and minimum eigenvalues. The difference between the maximum and minimum values in each direction is on average less than 10 %, as compared to the mean value of $\lambda_{\max}$ or $\lambda_{\min}$. Also, the ratio of the semi-major to semi-minor axis has a mean value of 1.10, which means that they create almost circular ellipses. Even the largest value of the ratio is less than 1.3. The standard deviation of the semi-major or semi-minor axis is about ±0.77 (less than 10 %

compared to the corresponding mean values), which is an evidence that the error ellipses are almost equal size.

	λ_{max} [cm]	λ_{min} [cm]	$\lambda_{max} - \lambda_{min}$ [cm]	$\lambda_{max} / \lambda_{min}$
Mean	8.40	7.66	0.75	1.10
Std.	±0.76	±0.77	±0.37	±0.05
Max.	9.60	8.93	1.77	1.26
Min.	6.56	5.83	0.13	1.02

Table 4.1 Statistics for the error ellipses.

Figure 4.10 illustrates the eigenvalues of the criterion matrix and the actual cofactor matrix in decreasing order. Since the estimates and the corresponding variance-covariance matrix are not invariant quantities of the model (as they depend on the geodetic datum choice), the eigenvalues of the cofactor matrix can be used as a measure of accuracy in certain (hyper-)dimensions defined by the corresponding eigenvectors.

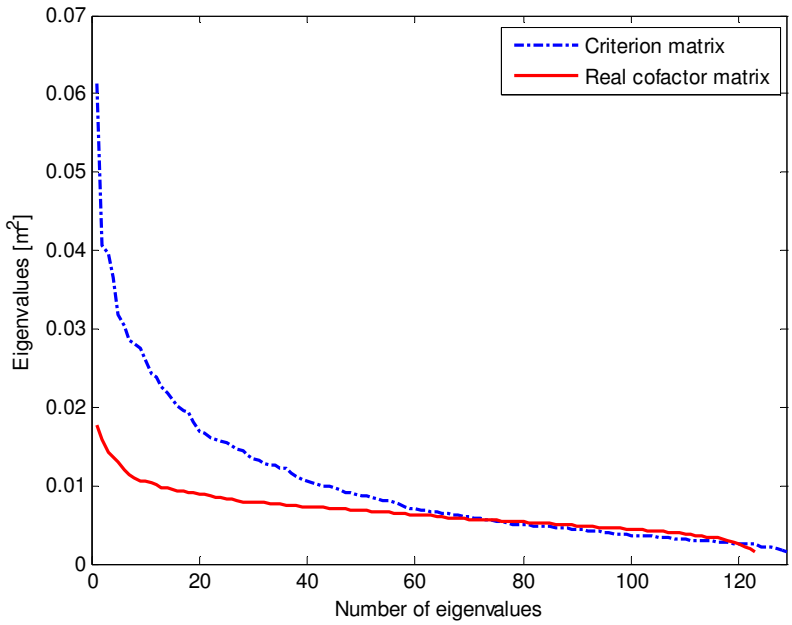

Figure 4.10 Eigenvalues of criterion and actual cofactor matrix.

In order to test the stability of the algorithm, another case of different starting station is tested. As can be seen in Figure 4.4, the IGS stations are clustered in North America

and Western Europe; thus, it is difficult to regenerate the network stations with different starting station. In other words, stations which are close to each other do not make any practical difference in the network optimization process, but the actual choice within the cluster can be different depending on the starting station. Therefore, in order to demonstrate that optimal station selection is repeatable regardless of the first station selection, 63 IGS stations are pre-selected based on the data availability and the distance to the neighboring stations. As shown in Figure 4.11, the station clusters from Figure 4.4 were practically replaced with single stations; notice that this pre-selection is still out of balance in terms of station distribution (Figure 4.11). Figures 4.12 and 4.13 illustrate the cases where different starting stations were used, namely, ALBH in North America and TIDB in Australia. As can be seen in the figures, both cases generate network stations almost uniformly, and more than 88 % of selected stations (38 out of 43 stations) coincide. Further testing of 63 cases with different starting station shows a consistency of 36 stations on average and its standard deviation is 2.2.

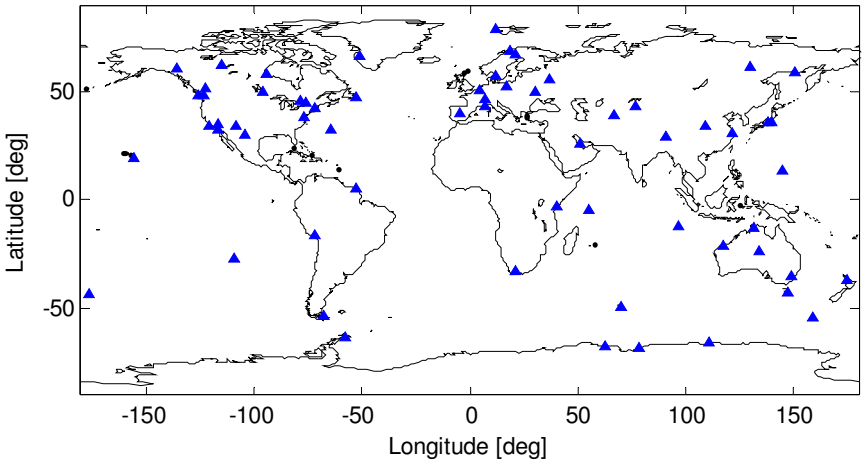

Figure 4.11 IGS network stations (63 pre-selected stations).

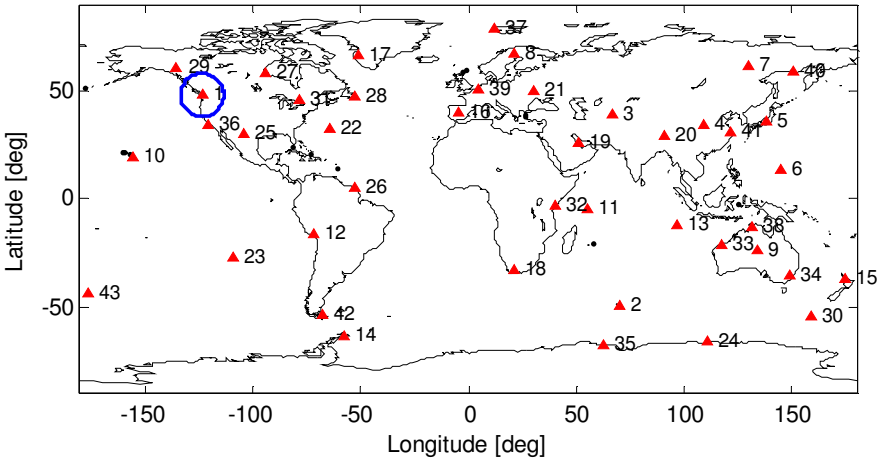

Figure 4.12 Optimal network stations from the pre-selected stations (starting from ALBH in North America).

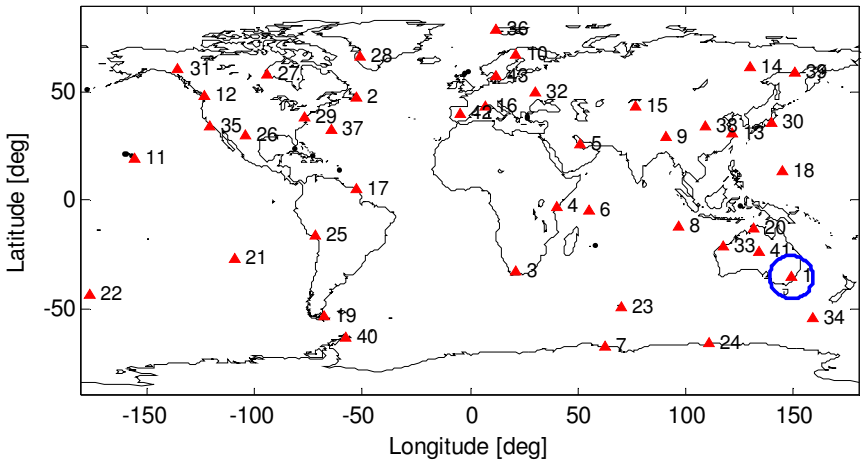

Figure 4.13 Optimal network stations from the pre-selected stations (starting from TIDB in Australia).

CHAPTER 5

ANALYSIS OF THE ORBIT ERRORS

Once the estimated orbit is available, its error should be evaluated as accurately and reliably as possible. Unfortunately, the true orbit can never be known, thus, the accuracy of the orbit solution can only be measured indirectly. The commonly used methods of evaluation include the comparison with other orbit solutions, internal consistency checks for the overlapping arcs of the solution, and independent validation with SLR (Satellite Laser Ranging) residuals or crossover data. In this chapter, the orbit solutions from different methods are analyzed in detail using the aforementioned methods. In the absence of the absolute reference orbit, the RSO is assumed to be the best orbit available to the public, thus, in this study the triple-difference based CHAMP orbits are compared to the RSO as an independent reference. It should be mentioned here that the dynamic solution of the CHAMP orbit, as computed in this study, is more thoroughly compared with the published RSO with regard to the consistency of the estimation methods.

5.1 Data Processing Strategy

To demonstrate the application of the techniques discussed in this study, the CHAMP data collected on 15 February 2003 are processed. Since the kinematic approach is practically dependent on the measurements and their geometry only, 24 hours of data are considered here as a sufficient sample. In the dynamic approach, however, it is a well-known strategy to estimate an additional arc before and after the main arc to reduce the edge effect of the orbit solution. Usually a 30-hour arc (24 hours of data plus 3 hours of data before and after each day) is used for the LEO dynamic POD, and the redundant parts, namely those, before and after the primary 24-hour arc, are usually discarded in the orbit solution. In this study, however, a decision was made to estimate 24 hours of arc for each day plus 2 extra hours of arc the next day, to facilitate computational efficiency. To be more specific, since the initial state vector is estimated using the observations of the entire arc, the orbit solution at the beginning of the 24-hour arc is sufficiently accurate. In

addition, the 30-hour arc produces a 24-hour primary arc, with only a negligible difference over the one derived from the 26-hour solution as shown in Figure 5.9 (see next section). The data arc for the reduced-dynamic orbit with the wave algorithm is the same as that coming from the dynamic approach.

The triple-differenced, ionosphere-free GPS phase observations are used in this study to compute the orbit solution in near real-time. Along with the processing efficiency, it is also important to satisfy the orbit accuracy to support GPS meteorology for atmospheric profiling. The triple-differenced observations can be obtained via epoch-by-epoch differencing of the consecutive double-differenced observations. The baseline is formed by a LEO and an IGS ground station at each end, respectively. The precise IGS orbits are used for the GPS satellites, and the ground station coordinates are referenced to ITRF2000. It should be mentioned that the published station coordinates are referenced to a specific epoch (for example, the position and velocity of ITRF2000 stations are given at 1997.0); thus, the velocity should be corrected to the measurement epoch to account for the plate tectonic motion of any station. Furthermore, the displacement of the stations due to the solid Earth tides and the polar motion should be applied to these coordinates (ocean tide loading effect is neglected here).

The elevation cutoff angles are set to 16 degrees for the 43 IGS ground stations and 10 degrees for the CHAMP satellite, which are rather conservative choices. Table 5.1 shows the relative percentage of observations for different elevation cutoff angles with respect to the case of 10° for CHAMP and 15° for the ground. Although it is possible to increase the number of observations up to 20 % by setting both cutoff angles to 5°, the quality of the observations might be poor due to the low antenna gain for low elevation angles. The impact of using observations from lower elevation cutoff angles needs to be investigated further, especially for the ground stations. It should be mentioned here that CHAMP has an altitude of more than 400 km, thus, there is no tropospheric effect on GPS measurements in this case, and it is set to zero in the data processing. While the GPS measurements from the CHAMP receiver are provided in 10-second intervals, data points at 30-second intervals are provided by the IGS stations; thus, the GPS triple-differenced measurements are formed every 30 seconds.

CHAMP / Stations	0°	5°	10°	15°
0°	125.07 %	123.34 %	116.69 %	104.67 %
5°	124.32 %	122.61 %	116.01 %	104.06 %
10°	118.95 %	117.31 %	110.99 %	99.51 %
15°	107.26 %	105.78 %	100.00 %	89.45 %

Table 5.1 Relative number of observations for different cutoff angles (with respect to the case of 10° for CHAMP and 15° for the ground stations).

Figure 5.1 illustrates the number of baselines and triple-differenced observations for the test data. There are data gaps in the latter part of the data and almost singular points around 6 o'clock. Also, it shows almost periodic changes of the geometry due to the near polar orbit of the CHAMP satellite.

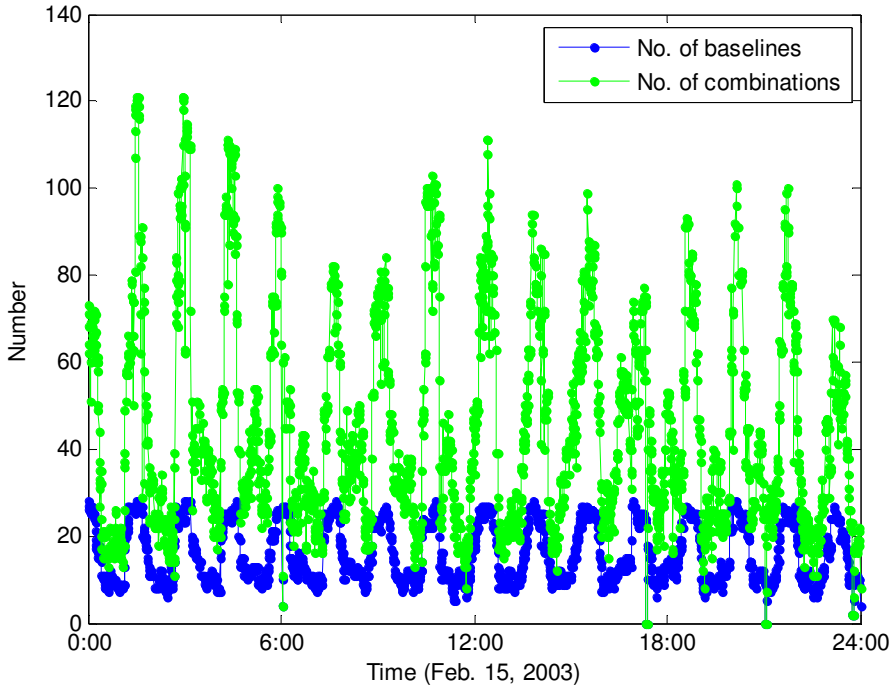

Figure 5.1 Number of baselines and triple-difference combinations (43 ground stations).

5.2 Analysis of Orbit Solutions

5.2.1 Kinematic Solution

The orbits estimated by the kinematic approach might suffer from the singularities caused by the lack of GPS data. The solution is also dependent on the satellite and baseline geometry and the data quality. Figure 5.2 shows the receiver clock offset computed from the absolute kinematic positioning. As can be seen in the figure, the CHAMP clock occasionally shows an unusually large correction, which is considered to be partially affected by the multipath errors in the aft-looking hemisphere due to cross-talk between the occultation antenna string and the primary POD antenna (Montenbruck and Kroes, 2003).

Figure 5.3 illustrates an orbit solution of absolute kinematic point positioning using pseudo-ranges. The overall accuracy compared to the RSO is ±26 meters in 3D RMS deviation after interpolating the epochs with data gaps (Table 5.2). This result is used as an initial approximation of the CHAMP satellite orbit for all kinematic solutions in this study.

	X [m]	Y [m]	Z [m]	3D [m]
Mean	1.074	-0.054	0.614	
Std.	±12.900	±13.173	±18.650	±26.225

Table 5.2 Statistics for the absolute kinematic positioning (24 hours).

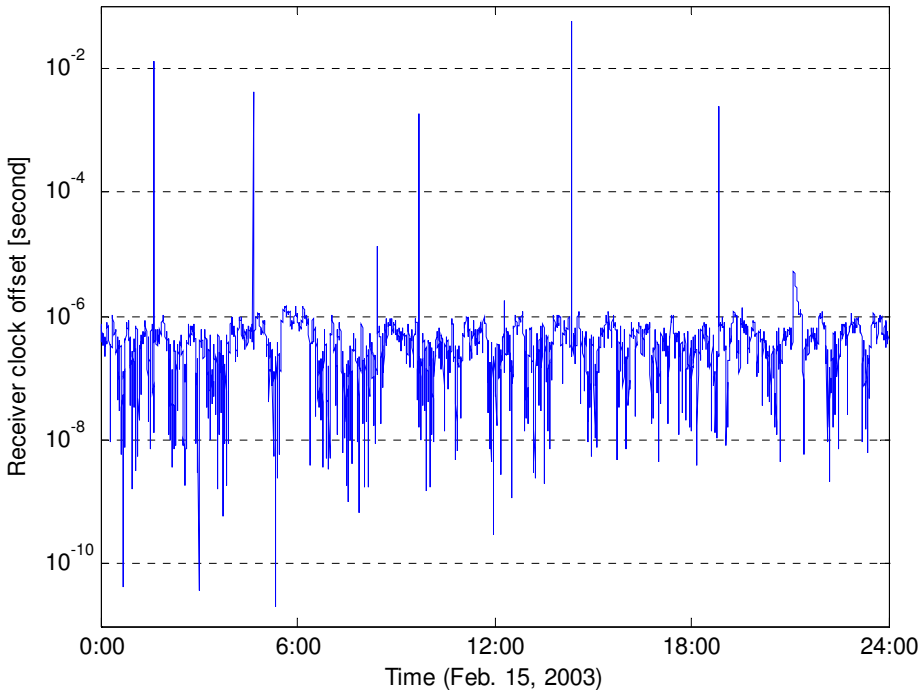

Figure 5.2 CHAMP receiver clock offset (24 hours).

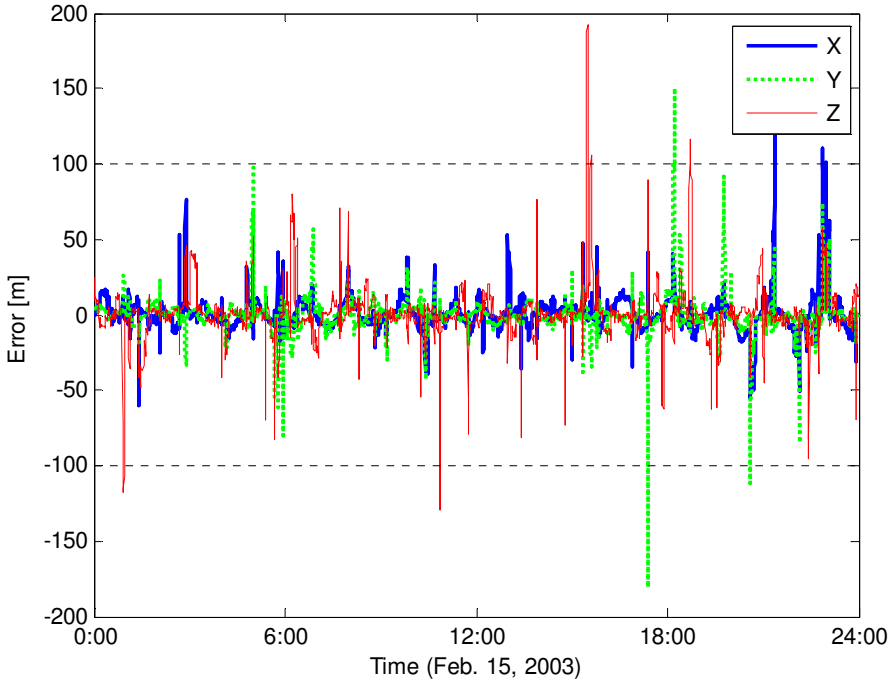

Figure 5.3 Comparison of the absolute kinematic orbit solution w.r.t. RSO.

It should be mentioned here that the term RMS deviation used in this study is defined as follows:

$$RMS(X) = \sqrt{Mean(X)^2 + Std(X)^2}\ , \tag{5.1}$$

$$3D\ RMS = \sqrt{RMS(X)^2 + RMS(Y)^2 + RMS(Z)^2}\ . \tag{5.2}$$

As mentioned earlier, the triple-differenced observations are not very sensitive to the data quality. Thus, the cycle slips are treated as data outliers, and excluded by pre-setting the threshold values in the data processing.

Since the triple-differenced observations contain the relative information only, namely, the position change between epochs, a datum should be provided in the adjustment model (Kwon et al., 2003). Thus, one can provide a fixed constraint at any epoch and estimate the unknowns of the remaining epochs. The adjustment with stochastic constraints for all epochs can also be applied, but the convergence is significantly slower and might result in a biased solution for the loose constraints (*ibid.*). Therefore, the position of the first epoch is fixed to estimate the LEO orbit and consequently, the number of unknowns is reduced by 3.

Fixing the initial position, however, will introduce errors to the solution at the subsequent epoch because the initial values are connected to the positions at all other epochs through their variance-covariance matrix. Therefore, because of these biases in the fixed initial orbit, the solution might not converge after the first epoch. In this case, both the forward and backward filtering should be applied in order to reduce the effect of the biased initial coordinates. Figure 5.4 represents the orbit solution of the forward filter for different sizes of the processing batch. It is clear from the figure that it takes about 300 epochs to converge, which means that the backward filtering is needed for the converged solution of all epochs.

The backward filtering can be performed by fixing the orbit solution from the forward filter at the last epoch, and then running the filter in the opposite direction. After the backward filtering, see Figure 5.5, most of the errors caused by the bias at the initial epoch is removed. It should be noted that the big jumps in the forward filter correspond to the epochs where the number of observed satellites drops.

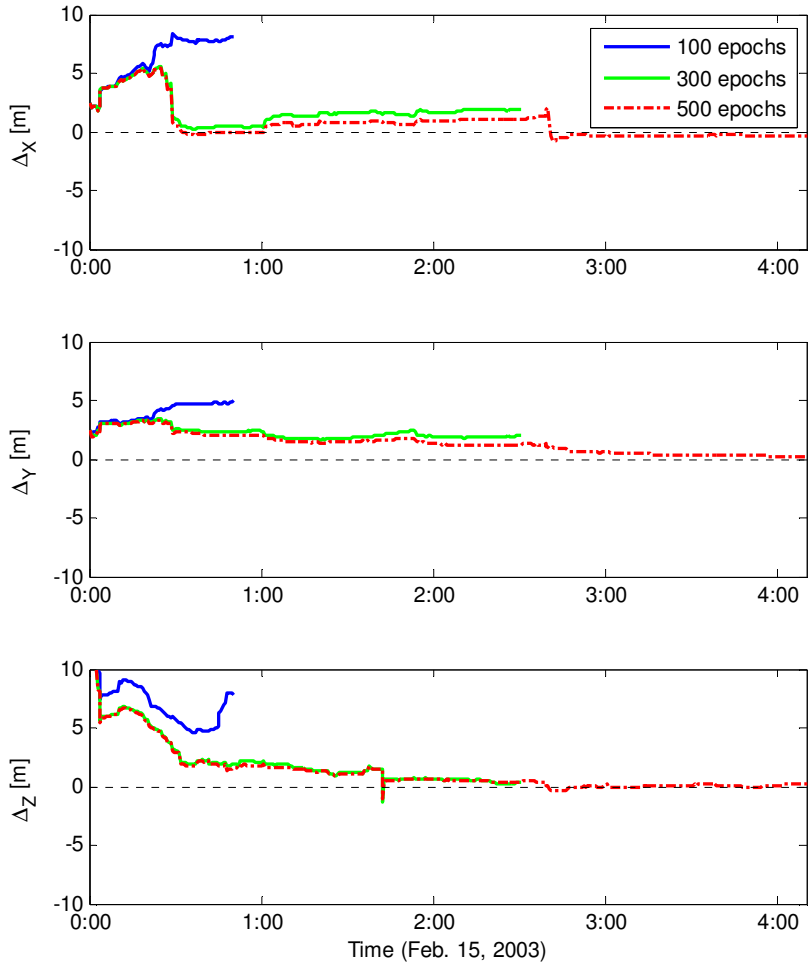

Figure 5.4 Effect of the batch size on the orbit solution (forward filter).

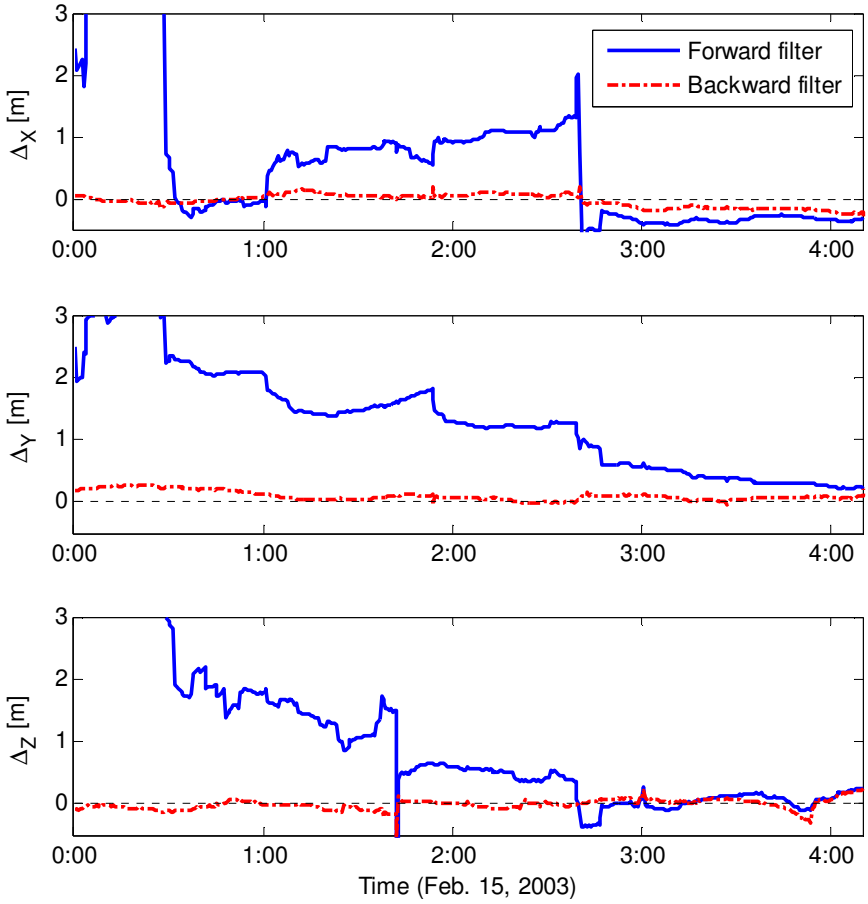

Figure 5.5 Forward and backward filter solutions (500 epochs).

Figure 5.6 shows the RMS orbit errors for different sizes of the batch. Usually the length of the batch is determined by the data gaps, cycle slips and large GDOP values which introduce singularities to the solution (Kwon et al., 2003). As can be seen in the figure, however, for a short length of arc, say, 300 epochs or less, the biases might not be sufficiently removed even by the backward filtering. In this case the iterative scheme is required until the solution converges. Three iterations of forward and backward filtering seem to be sufficient according to the tests done in this study, which can still be done in near real-time due to the short arc to be processed.

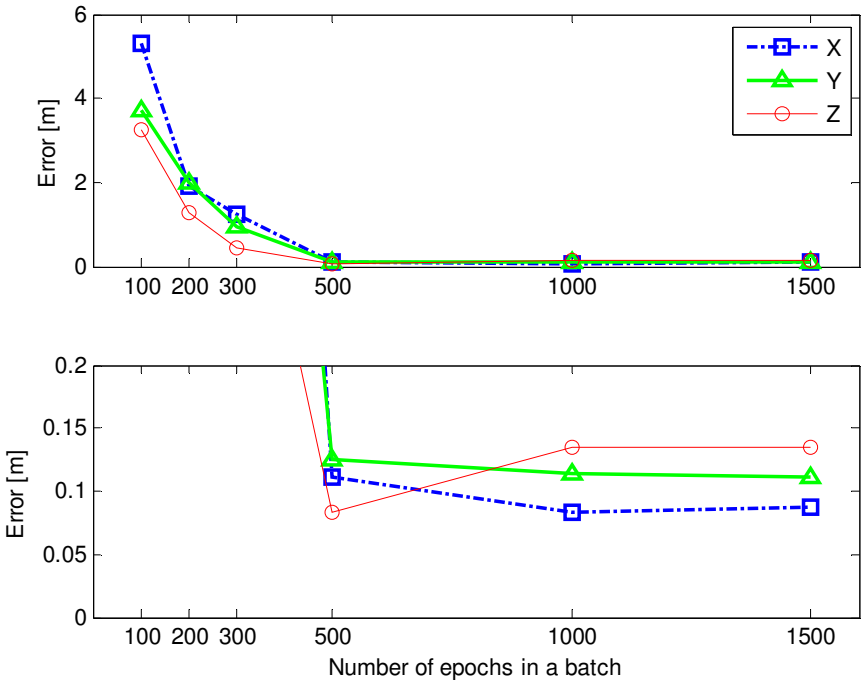

Figure 5.6 Orbit errors for different batch sizes (backward filter). Bottom figure is the magnification of top figure.

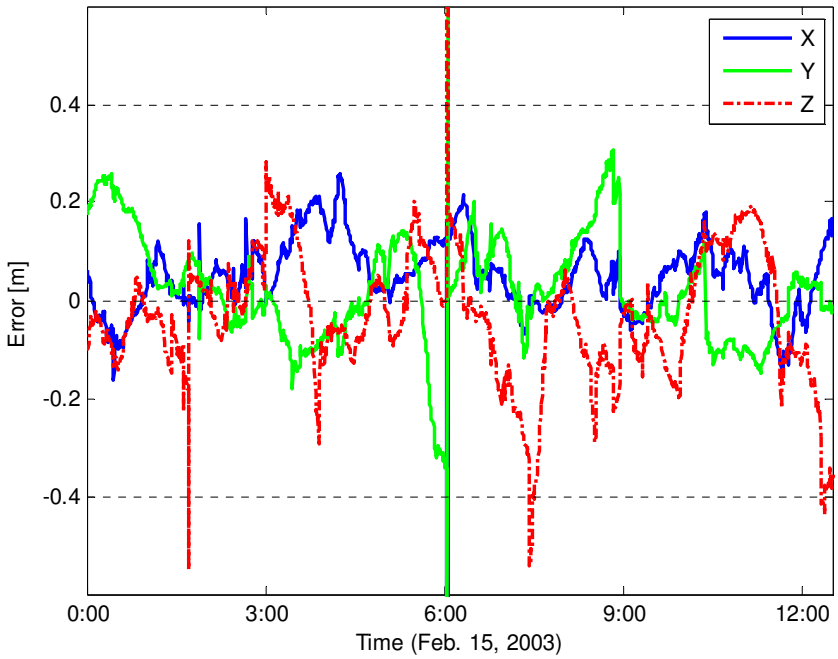

Figure 5.7 Backward filter solution (1500 epochs).

Figure 5.7 illustrates the kinematic orbit solution for 1500 epochs of data after backward filtering. This is almost the largest batch possible in this test data set because of a data gap beyond the final point of the processed arc. It should be noticed here that the singularity at some epochs cannot be overcome even when the backward filtering is applied; notice the peak around 6 o'clock in the figure. Based on this study, one can claim that the achievable accuracy of the kinematic approach is better than ±20 cm in 3D RMS deviation when compared to the reference RSO (Table 5.3) after removing the points with singularities. The processing time for the 1500 epochs of data in a batch solution takes about 1.7 hours for both forward and backward filtering on a 3 GHz PC platform.

	X [m]	Y [m]	Z [m]	3D [m]
Mean	0.049	0.021	-0.033	
Std.	±0.072	±0.109	±0.131	±0.185
RMS	±0.087	±0.111	±0.135	±0.195

Table 5.3 Statistics for the kinematic orbit solution (1500 epochs).

In order to demonstrate the achievable accuracy of the kinematic approach under good geometry, a 10-minute arc with the maximum number of observations was chosen from the simulation study (just before 2 o'clock; see Figure 3.3). As can be seen in Table 5.4, this solution, as compared to the RSO, gives less than ±1 cm of orbit differences in each component, except for a few-centimeter bias in Y and Z directions. Therefore, this clearly shows that the kinematic approach has a potential to provide much improved orbit solutions with the inclusion of the upcoming GNSS satellites (the reasonable tracking geometry of the ground stations is also required for the differenced observations).

	X [cm]	Y [cm]	Z [cm]	3D [cm]
Mean	-0.30	8.23	4.57	
Std.	±0.83	±0.75	±0.60	±1.27
RMS	±0.88	±8.26	±4.60	±9.50

Table 5.4 Statistics for the kinematic orbit solution for a 10-minute arc.

In her recent work, Bock (2003) reports that when the best zero-differenced kinematic solution using code and phase-difference observations is compared to the TUM (Technical University of Munich) solution, an RMS error per coordinate is obtained about ±10 cm after a Helmert transformation between the orbit solutions. Also, Bisnath (2004) shows an orbit difference of about ±32 cm in 3D RMS error for 24 hours of arc compared to the JPL solution, using single-receiver data and a geometric approach.

It should be mentioned that the POD procedure should be reset and a new segment created whenever a singularity occurs due to the lack or loss of the GPS signal. As mentioned in Chapter 2, an orbit error of ±30 cm is required to support the GPS atmospheric profiling. Therefore, the kinematic approach with triple-differenced observations is capable of supporting this requirement under a favorable geometry.

5.2.2 Dynamic Orbit

The primary unknowns in the dynamic approach are the initial states, which are composed of the position and velocity vectors at the first epoch of the arc, and some other dynamic parameters. The *a priori* values for the initial state vector can be obtained, for example, from the adjustment of the previous day. For this study, the uncertainties of the initial state vector are set to ±1 m and ±0.1 m/s for the position and velocity, respectively. A numerical integrator with a variable order and step size is used, and set to provide the output at a 30-second interval that corresponds to the time interval of the RSO solution and GPS measurements update from the ground stations. The tropospheric delay for the IGS ground stations was corrected using the modified Hopfield model (Goad and Goodman, 1974). The NRLMSISE-00 model is used for the atmospheric drag force modeling, with the area-to-mass ratio of the CHAMP satellite given as 0.00138 m^2/kg. For simplicity, the cannon ball model is used for the modeling of the satellite's body to compute both the atmospheric drag and the solar radiation pressure.

Parameters		Frequency	Number
Initial state vector	Position	-	3
	Velocity	-	3
Atmospheric drag		One per hour	26
Solar radiation		One per arc	1
Empirical force	Once/rev.	Every orbit	68
	Twice/rev.	Every four orbits	20
Total			121

Table 5.5 The parameters to be estimated in the "reference case."

The parameters to be estimated and the model used in this study (called the "reference case") are listed in the following, and summarized in Table 5.5:

- ✓ The initial state vector (position and velocity),
- ✓ The atmospheric drag coefficients (1 parameter/hour),
- ✓ The solar radiation scale factor (1 parameter/arc),
- ✓ The once-per-revolution empirical force parameters (every orbit),

- ✓ The twice-per-revolution empirical force parameters (every four orbits),
- ✓ Geopotential model (EIGEN2, degree/order 120×120),
- ✓ The arc length (26 hours).

It should be noted that only 121 parameters are estimated for one full day orbit since there are no ambiguity parameters. This is a significant computation load reduction, as compared to 13200 ambiguity parameters (from about 100 IGS ground stations) in the double-differenced dynamic POD (Švehla and Rothacher, 2003). Assuming GPS measurements from the IGS ground stations are ready for processing, the processing time to estimate the 121 parameters for the 26-hour arc is about 2.5 hours (30 minutes per iteration), on the same machine as mentioned in the previous section. Currently, the latency of the RSO daily solution is claimed at about 16 hours (not being published at this latency), and the JPL solution has similar latency (Kuang, 2006). The ground contact of CHAMP satellite for data downloading is done about every 86 minutes, and the RINEX files from the ground stations are transferred to the processing centers with a maximum time delay of 15 minutes (Wickert et al., 2004); thus, the time delay due to the data transfer can be neglected. The 3-hour arc solution, as the criterion for the "near" real-time, based on the technique presented in this study, can be obtained in about 20 minutes and shows a comparable accuracy to the 26-hour arc solution (Bae, 2005b).

Degree/order		N [cm]	T [cm]	R [cm]	3D [cm]
50×50	Mean	-1.50	2.49	-2.28	
	Std.	±17.66	±16.72	±10.33	±26.42
70×70	Mean	-0.86	1.59	-2.36	
	Std.	±4.99	±7.52	±3.92	±9.84
90×90	Mean	-0.89	0.54	-2.08	
	Std.	±4.33	±6.31	±3.57	±8.45
120×120	Mean	-0.76	1.39	-1.93	
	Std.	±3.80	±6.10	±3.33	±7.91
140×140	Mean	-0.73	1.38	-1.94	
	Std.	±3.77	±6.07	±3.30	±7.87

Table 5.6 Orbit differences for various choices of degree/order of the gravity model when compared with the RSO in the RTN frame.

Table 5.6 shows the dynamic-orbit solution for various choices of degree and order of the geopotential model used. The geopotential model used in this study, EIGEN2, has a maximum degree/order of 140. As can be expected, considering CHAMP's altitude, the CHAMP orbit is visibly sensitive to the degree/order up to 70, and only moderate, but

increasing improvement can be obtained for the higher degree/order.

It should also be noted here that the error in the along-track direction is almost twice as big as the other two components, especially in the case of the solutions with the gravity model developed to degree/order 120 and 140. This follows from the fact that the most dominant nonconservative force, which is the atmospheric drag, points in the opposite direction of the velocity component. In reality, the along-track component diverges the fastest if the atmospheric drag is not modeled appropriately.

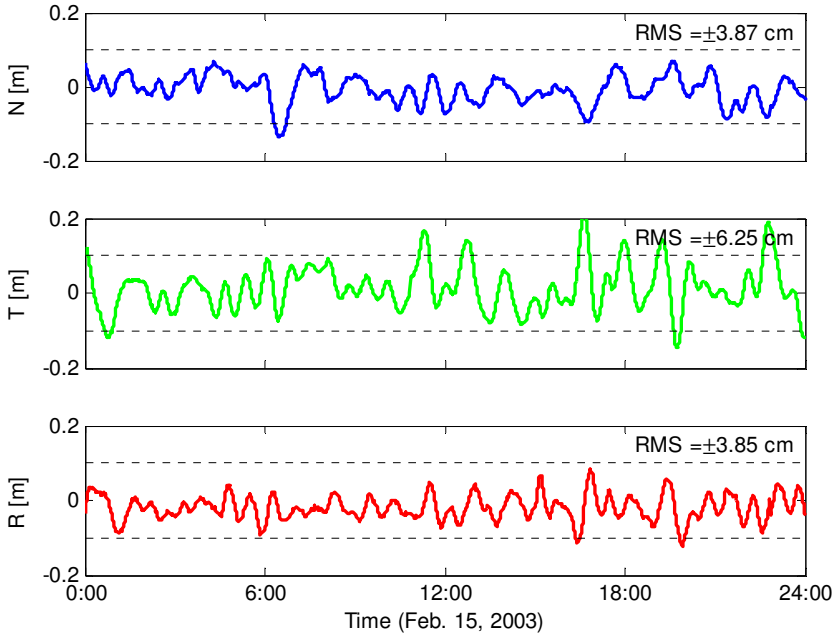

Figure 5.8 Orbit differences in the "reference case" when compared with the RSO in the RTN frame.

Figure 5.8 illustrates the orbit difference in the RTN frame in the "reference case" after 5 iterations of the batch filter, with the geopotential developed to degree/order 120 and with a 1-hour interval for the atmospheric drag parameter estimation. The result is plotted for the 24-hour span, although it converged for the entire 26 hours of arc.

Another orbit accuracy assessment can be made by performing the internal consistency check of the overlapping arcs. Figure 5.9 shows the 24-hour orbit difference between the "reference case" and the 30-hour arc, which extends 3 hours before and after one full day. As can be seen in the figure, the two orbit solutions are close to each other, except for the first few epochs. The results show differences of less than ±1.3 cm of RMS error in each direction, and ±2 cm in 3D deviation (not shown in this figure). The difference at the beginning of the arc is due to the fact that the coordinates at the first

epoch were unknown in the "reference case," and no epochs prior to the first epoch were used in the processing. The frequent fluctuations in the along-track and radial components are considered as phase shift in the empirical force modeling.

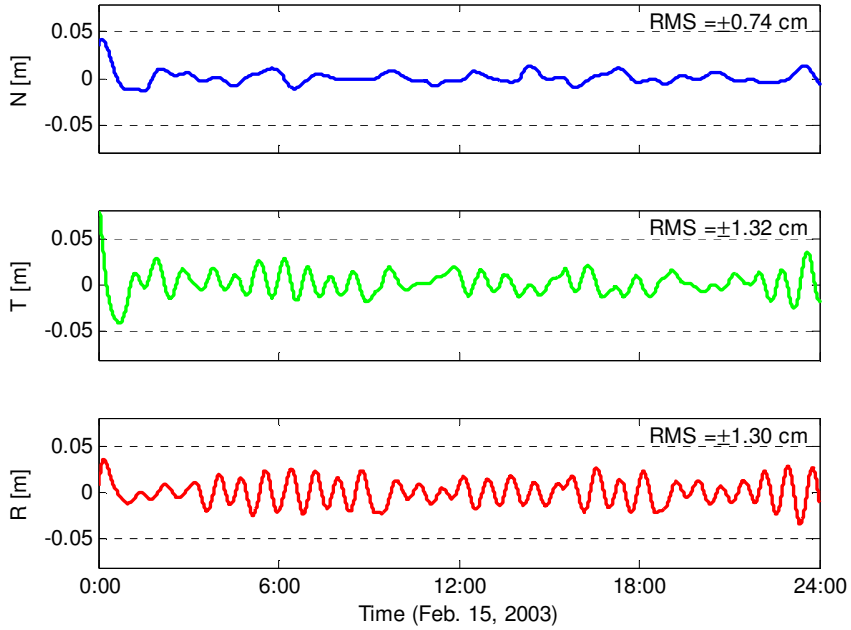

Figure 5.9 Internal consistency of the orbit solution;
the "reference case" vs. 30 hours of arc.

As discussed earlier, the force modeling of the satellite dynamics is not accurate enough for precise orbit determination. Therefore, the empirical force parameters can be included in the state vector to improve the orbit solution. A closer look at the STAR accelerometer data reveals the periodic properties of the once- and twice-per-revolution nonconservative forces (see Figure 3.8), which are predominantly in the along-track component. Figure 5.10 shows the orbit solution of the "reference case" after these empirical parameters has been modeled in the dynamic POD. Apparently, once- and twice-per-revolution components are significantly reduced in the Fourier spectrum of the orbit error in the along-track direction. It should be mentioned here that the along-track and radial components are estimated for the twice-per-revolution empirical forces, which gives better results than in the other case (*i.e.*, estimating the cross- and along-track components). The reason for this is not clearly understood and should be investigated further.

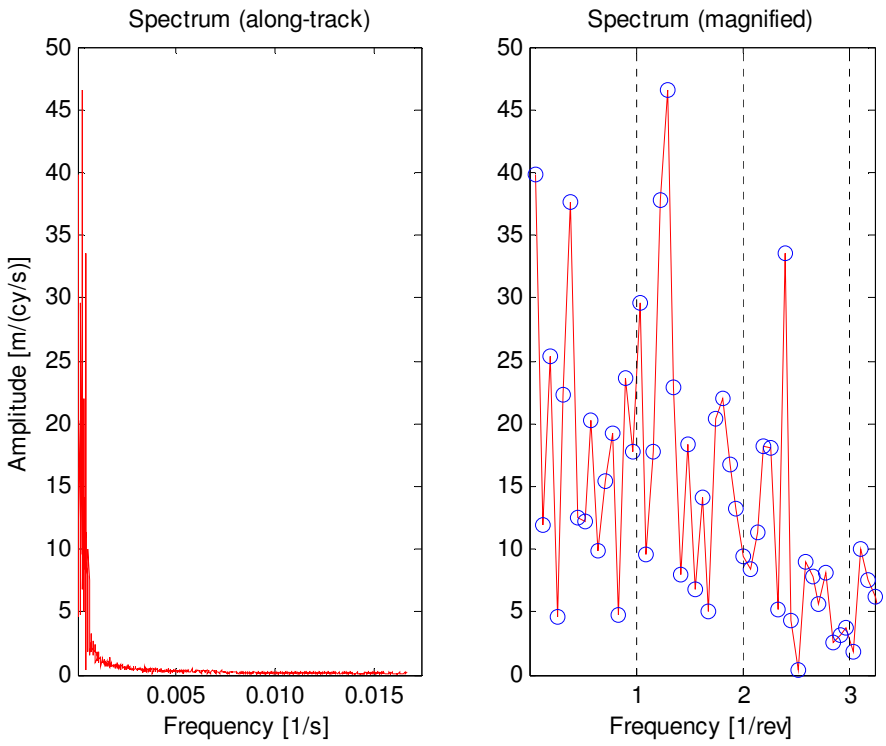

Figure 5.10 Fourier spectrum of the orbit error (along-track).

Drag interval		N [cm]	T [cm]	R [cm]	3D [cm]
1 hr	Mean	-0.76	1.39	-1.93	
	Std.	±3.80	±6.10	±3.33	±7.91
2 hrs	Mean	-0.76	0.12	-1.85	
	Std.	±3.81	±6.67	±3.31	±8.36
4 hrs	Mean	-0.75	-0.23	-1.80	
	Std.	±3.74	±8.53	±5.24	±10.69
8 hrs	Mean	-0.81	0.35	-2.15	
	Std.	±5.80	±25.24	±21.61	±33.73
10 hrs	Mean	-0.68	0.75	-2.05	
	Std.	±5.36	±19.94	±15.90	±26.06

Table 5.7 The statistics of the orbit solutions with various time intervals for the atmospheric drag parameter estimation.

In order to find out the optimal arc length of the atmospheric drag force parameters,

a total of five different cases was tested based on the "reference case" (Table 5.7); the atmospheric drag parameters were estimated every 1 hour, 2 hours, 4 hours, 8 hours and 10 hours of arc, where the 1-hour arc case corresponds to the "reference case." The results suggest that the orbit differences will dramatically increase if the drag coefficient is estimated with a frequency less than once per 4 hours. This is so because the atmospheric density at CHAMP altitude can fluctuate rapidly due to the varying density of the Sun flux particles and changing geographic location of the CHAMP satellite.

The velocity of the CHAMP satellite is obtained simultaneously by solving the equations of motion of the satellite in the dynamic POD via numerical integration techniques. Figure 5.11 illustrates the velocity differences in each component of the CHAMP orbit. The differences between the estimated and the published RSO velocity in the inertial frame are transformed to the RTN frame. It should be noted here that the noise level of the three components is almost the same, although the along-track component is slightly larger than the other two. The resulting velocity differences are at the level of ±0.07 mm/s in each component and ±0.12 mm/s in 3D RMS. These quality-of-fit results are comparable or even better than those for the CHAMP dynamic velocity estimates of various POD analysis centers. This result is computed by cross-comparison among the solutions from the IGS analysis centers, reporting average RMS deviation for each pair of solutions below the ±0.1 mm/s level (Švehla and Rothacher, 2003).

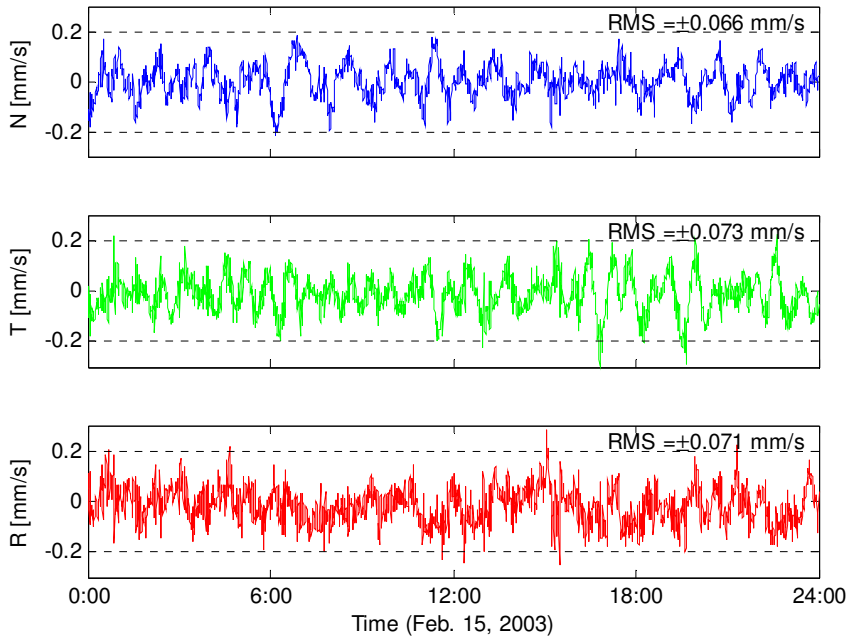

Figure 5.11 Velocity differences in the "reference case" when compared with the RSO in the RTN frame.

5.2.3 Reduced-Dynamic Solution with the Wave Algorithm

The reduced-dynamic solution is usually performed in two steps: estimation of the dynamic solution followed by process noise estimation (Yunck et al., 1994; Kuang et al., 2001). Once the dynamic solution has converged, all the dynamic parameters are fixed, for convenience, to the estimated values; then, the process noise in form of impulses can be estimated with the wave algorithm. As explained in Chapter 3, the wave algorithm is considered as a zero initial condition problem of the state vector. Thus, the estimated Dirac impulse vector is propagated to the last epoch of each cycle, which then becomes an update to the reference orbits. The fundamental difference between the reduced-dynamic algorithm developed at JPL and the wave algorithm used in this study is the fact that the process noise is estimated once every predetermined cycle instead of every epoch. The rationale of this approach is that the behavior of dynamic orbit errors shows a wave-like pattern even after the empirical parameters have been estimated (see Figure 5.8); thus, the error for a certain number of epochs is considered as one wave to be estimated.

Since the reference orbit for the wave filter is propagated from the initial epoch using the parameters which have been estimated in the dynamic approach, it should be close to the dynamic orbits. The only difference comes from the fact that the state transition matrix in Kalman sequential filtering is reinitialized at every epoch contrary to the dynamic solution. Thus, the remaining orbit errors are fitted to the wave function and finally added to the reference orbit to generate a wave estimated orbit. As is the case for the kinematic approach, the estimated wave (as correction to the state vector) has a bias at the initial epoch of each cycle. Therefore, this bias should be removed by the smoothing filter which computes the estimates backwards by using the state transition matrix that was stored during the forward filter. Also, the last epoch of the forward filter should be fixed for the smoothing process.

Figure 5.12 shows the variation of the error variances for the position vector after the forward wave filter was applied. Since the initial state vector of each cycle is assumed to have randomness, there are peaks at each cycle which will decrease as the measurements are processed. After smoothing, the sigma values remain at a level of a few millimeters with some fluctuation.

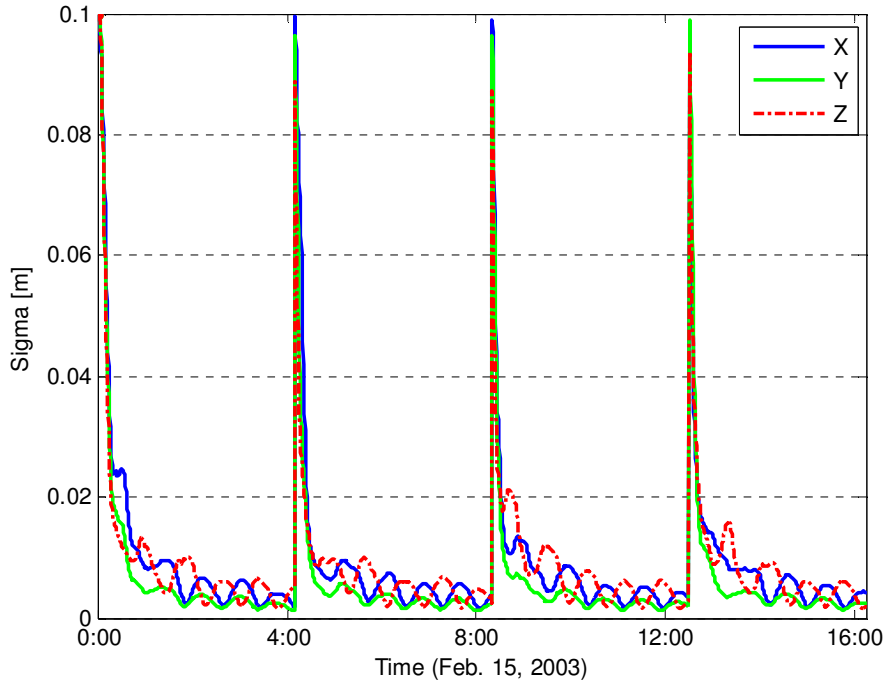

Figure 5.12 Error variances of the position vector (wave forward filter).

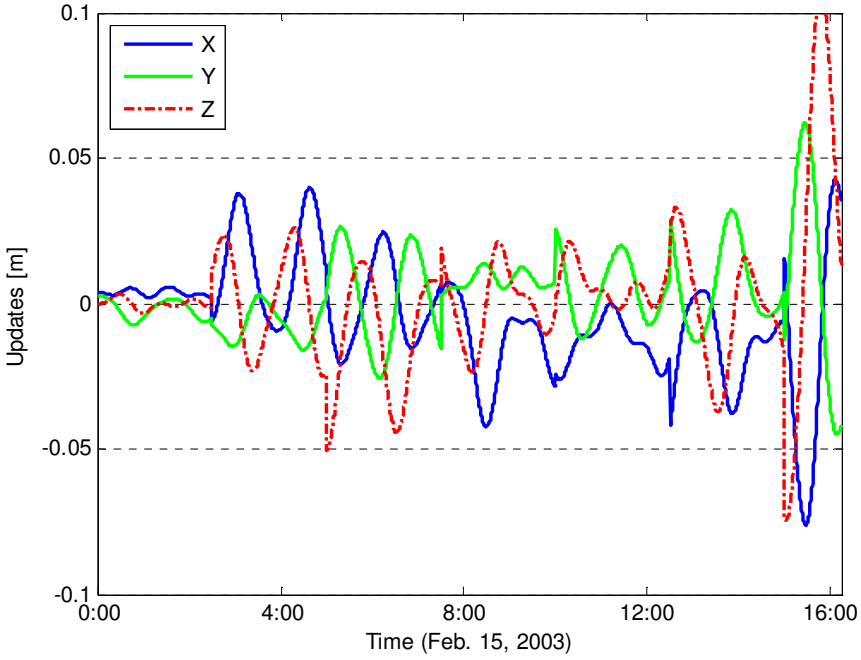

Figure 5.13 Position updates (wave-smoothed filter).

Based on the test to determine a suitable number of epochs for each cycle, the wave filter is applied to the 16 hours of arc with 300 epochs of cycle length, since there is a data gap beyond this point. During this gap, the estimates should be propagated using the dynamic model only because the filter diverges quickly without the measurement updates. Once the observations are available again, this filter can proceed furnishing the updates with the measurements. Figure 5.13 illustrates the position updates after the backward smoothed filter. Since the estimated values have not converged at the beginning of each cycle, the process should be smoothed by the backward smoothed filtering. The drawback of the wave filter is that there are discontinuities on both sides of each cycle, as can be seen in the figure. Although the orbit remains smooth in spite of these discontinuities, it is desirable to have smoothed updates for the orbit. Therefore, one must interpolate the position updates at the points of discontinuity using the data on both sides.

Method		N [cm]	T [cm]	R [cm]	3D [cm]
Dynamic orbit	Mean	0.53	-0.72	1.96	
	Std.	±3.60	±5.28	±2.83	±6.99
Wave filter	Mean	0.54	-1.92	2.06	
	Std.	±3.47	±5.05	±2.82	±6.75
Correlation coef.		0.98	0.93	0.97	

Table 5.8 Comparison of dynamic orbit and wave filter solution.

As can be seen in Table 5.8, there is a little improvement in the variance of the orbit difference of the wave filter solution; note that both orbits were compared with the published RSO. However, the wave filter solution has a slightly larger along-track bias. This seems to be a property of the wave filter, which means that each cycle must be estimated to compensate for the error in that cycle. Thus, the entire arc of the orbit might be biased depending on the error behavior of each cycle. The correlation coefficients in the table tell how much two orbit solutions are similar to each other in their behavior.

Clearly, the overall RMS fit of the wave filter solution is similar to that of the dynamic orbits. This is so because the dynamic approach already includes the empirical force models which correspond to the stochastic process noise in the reduced-dynamic approach. Thus, the unmodeled forces are absorbed by this modeling to a large extent. Also the reduced-dynamic procedure is performed after the dynamic solution has converged; therefore, there is no room for much variation from the dynamic orbits. In summary, the wave algorithm used in this study can absorb the unmodeled forces in the form of process noise while following the wave-like shape of the orbit errors favorably. It is expected that more pronounced impact of the wave algorithm could be observed if simplified force model were used in the dynamic solution

5.3 Consistency Testing

The orbit comparison for different solutions can also be accomplished by the consistency testing. Since the kinematic solution is interrupted due to the data gaps, and the published RSO is a solution based on the dynamic approach, it was decided to have a consistency test only for the dynamic solution. The basic idea of the consistency testing is to check the change in the sum of squared residuals of the measurements due to constraining the solution. Therefore, one can begin the consistency testing from the well-known Gauss-Markov model used here.

The Gauss-Markov model with stochastic constraints is again given by

$$y = A_{n\times m}\xi_{m\times 1} + e\,, \quad e \sim \mathcal{N}(0, \sigma_0^2 P^{-1})\,, \tag{5.3}$$

$$z_0 = K_{l\times m}\xi_{m\times 1} + e_0\,, \quad e_0 \sim \mathcal{N}(0, \sigma_0^2 Q_0), \quad C\{e, e_0\} = 0\,, \tag{5.4}$$

where n denotes the number of observations, m the number of unknown parameters and l denotes the number of stochastic constraints; $\mathcal{N}$ indicates the normal distribution. Along with the least-squares solutions, the sum of squared residuals, which is used for the hypothesis testing, is given by

$$\Omega := y^T P y - \hat{\xi}_u^T c\,, \tag{5.5}$$

$$R := (z_0 - K\hat{\xi}_u)^T (Q_0 + KN^{-1}K^T)^{-1}(z_0 - K\hat{\xi}_u)\,, \tag{5.6}$$

where $:=$ means "equal by definition" and $\hat{\xi}_u$ denotes an unconstrained solution, which is the solution of Eq. (5.3) only, with the notation of

$$\begin{bmatrix} N & c \end{bmatrix} = A^T P \begin{bmatrix} A & y \end{bmatrix}. \tag{5.7}$$

In order to check whether the stochastic constraints are consistent with the observation model, it is necessary to test the null hypothesis of

$$H_o:\ z_0 = K\xi + e_0 \tag{5.8}$$

against the alternative hypothesis of

$$H_a : \; z_0 \neq K\xi + e_0 . \tag{5.9}$$

The test statistic for the hypothesis testing can be represented by

$$T := \frac{R/l}{\Omega/(n-m)} \; \sim \; F(l, n-m), \tag{5.10}$$

which means that, under H_o, it follows the *F*-distribution with degrees of freedom of l and $n-m$. Let α be the significance level of the test which represents the probability of rejecting the null hypothesis when it is true – also called a type I error. Thus, the null hypothesis, H_o, is rejected if the test statistic, T, is greater than the criterion, $F_\alpha(l, n-m)$.

In this study the published RSO is used as stochastic constraints during the adjustment of dynamic parameters. The RSO is given for all epochs in the arc, though the satellite state is estimated for the first epoch. Therefore, it is reasonable to constrain the RSO (position only) for all epochs as stochastic information because the consistency of the entire arc is not guaranteed by the first epoch only. Since the unknown parameter vector, ξ, refers to the initial epoch of the arc, all the stochastic constraints should be mapped again back to the initial epoch to be consistent with the observation model. In other words, the stochastic constraints of the RSO can be expressed in detail to be identical with Eq. (5.4):

$$\underbrace{\begin{bmatrix} (\mathbf{r}_{RSO} - \mathbf{r}^o)_{t_1} \\ (\mathbf{r}_{RSO} - \mathbf{r}^o)_{t_2} \\ \vdots \\ (\mathbf{r}_{RSO} - \mathbf{r}^o)_{t_n} \end{bmatrix}}_{z_0} = \underbrace{\begin{bmatrix} \bar{K}\Phi(t_1, t_1) \\ \bar{K}\Phi(t_2, t_1) \\ \vdots \\ \bar{K}\Phi(t_n, t_1) \end{bmatrix}}_{K} \xi + e_0 , \tag{5.11}$$

where $(\mathbf{r}_{RSO} - \mathbf{r}^o)_{t_k}$ represents the difference between the RSO and the approximated coordinates of LEO at time t_k, Φ is the state transition matrix as explained in Chapter 3, and the coefficient matrix $\bar{K}$ is given by

$$\bar{K} = \begin{bmatrix} I_3 & 0_{3\times(m-3)} \end{bmatrix}_{3\times m} \tag{5.12}$$

because it is assumed that only the CHAMP position is constrained in this study. As can be seen in Eqs. (5.6) and (5.11), the matrix to be inverted is very large when the entire RSO is constrained. Therefore, it would be better to estimate the unknown

parameters first for the stochastic-constraints model, and then compute R by subtracting Ω, as given by Eq. (5.5), from the total sum of squares of the residuals:

$$(\Omega + R) = y^T P y + z_0^T P_0 z_0 - \hat{\xi}^T (c + K^T P_0 z_0), \tag{5.13}$$

$$R = (\Omega + R) - \Omega, \tag{5.14}$$

with $P_0 := Q_0^{-1}$.

Table 5.9 shows the results of the hypothesis testing with the stochastic constraints of the RSO. For 26 hours of arc, three components of the position vector are constrained at each epoch as given by Eq. (5.11). Therefore, the total number of 9330 constraints is used in the hypothesis testing. The number of unknowns in the parameter vector, ξ, is 121 as mentioned in the previous section. Given the degree-of-freedom and the significance level, $\alpha := 5\%$, the criterion for the hypothesis testing will be

$$F_\alpha(l, n-m) = F_{.95}(9330, 139104) = 1.025 .$$

σ_{RSO}	±5 cm	±4 cm	±3 cm	d.o.f
Ω	144852.293	144852.293	144852.293	139104
R	6599.331	9070.863	13620.958	9330
T	0.679	0.934	1.402	
	accept H_o	accept H_o	reject H_o	

Table 5.9 The results of the hypothesis testing.

As can be seen in Table 5.9, the dynamic orbit solution obtained in this study is consistent with the published RSO, as long as the absolute accuracy of RSO is considered to be no better than ±3 cm, which is a quite convincing result. In other words, this result indicates that the triple-differenced solution proposed here is of accuracy equivalent to RSO, while it offers the benefit of an algorithmic simplicity and efficiency combined with affordable processing time and smaller computational overhead.

5.4 SLR Residuals

Given that the absolutely true orbit solution is not known, SLR (Satellite Laser Ranging) residuals are commonly used as a means of independently validating the GPS-based orbit solution. SLR is still the most accurate satellite tracking method, claiming a

precision of just a few millimeters in RMS error for the normal point (NP) corrected data, which are derived from the statistical compression of the measured ranges. As explained in Chapter 2, CHAMP carries a Laser Retro-Reflector (LRR) onboard to reflect the laser signal back to the ground tracking stations. More than 50 SLR stations are currently operating - their network is shown in Figure 5.14. The performance of the SLR stations (since the year 2000) can be found in the station performance charts (http://ilrs.gsfc.nasa.gov/stations/station_info_plots_since_2000/index.html).

With the improved precision of SLR in the late 1980's, it was found that the ranging data from some satellites were distributed non-symmetrically (http://ilrs.gsfc.nasa.gov/). Thus, it was suggested that the full-rate data be reduced to the normal point using a statistical approach, and now NP data form the primary ILRS (International Laser Ranging Service) station data product. The idea behind this algorithm is to formulate range residuals from a trend function and data screening, and then compute the normal point by locating the particular observation to a certain bin (fixed interval). For the detailed algorithm of the normal point formulation, one can refer to Sinclair (1997).

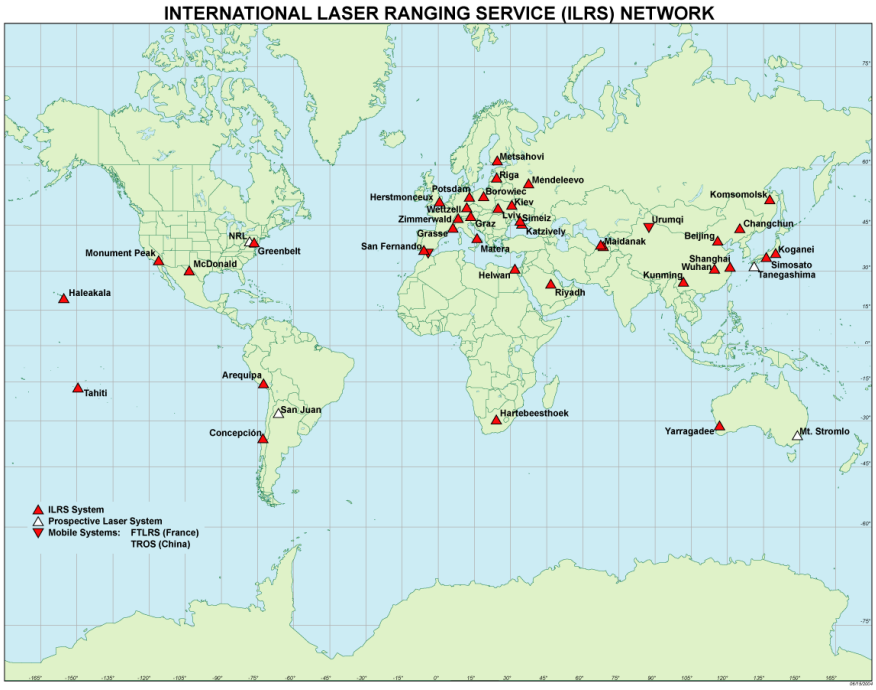

Figure 5.14 International Laser Ranging Service (ILRS) network (http://cddis.gsfc.nasa.gov/images/ilrsmap.gif).

The header record of the published ILRS NP data provides the wavelength of the laser and its time scale. The time of laser firing, the two-way time-of-flight as well as surface pressure, temperature and relative humidity are also in the SLR data record. Since the wavelength of the laser is very short (about 0.5 μm), only the tropospheric correction

needs to be applied to the measured range. The general relativistic correction is also too small and, thus, just neglected here. The formulation of the Marini and Murray model is generally used for the correction of SLR range measurements. The one-way range correction, which is subtracted from the measured range, is given by

$$\Delta R = \frac{f(\lambda)}{f(\phi, H)} \cdot \frac{A + B}{\sin E + \dfrac{B/(A+B)}{\sin E + 0.01}} \tag{5.15}$$

with

ΔR : the range correction in meters;
$f(\lambda)$: the laser frequency parameter;
$f(\phi, H)$: the laser site function;
E : the true elevation angle of the satellite;
λ : the wavelength in micrometers;
ϕ : the geodetic latitude;
H : the height above the geoid in kilometers.

The detailed expressions of A and B as well as $f(\lambda)$ and $f(\phi, H)$ can be found in (McCarthy and Petit, 2003).

CDDIS (Crustal Dynamics Data Information System) archives and provides the SLR data for each satellite and receiver (ftp://cddis.gsfc.nasa.gov/slr/). Unfortunately, since a small amount of SLR data for CHAMP is available (5 stations per day on average, and less than 5 minutes of arc for each station), only a small fraction of CHAMP orbit can be validated by SLR data. For the test data used in this study (February 15, 2003), the SLR data from two stations are available; Yarragadee has 38 observations of NP data (3.5 minutes of arc) and Riga has 16 (1.5 minutes of arc) for the entire 24-hour arc (see Figure 5.15). The published SLR station coordinates can be obtained at the ITRF (International Terrestrial Reference Frame) website (http://itrf.ensg.ign.fr/). Table 5.10 shows the published SLR station coordinates used in this study.

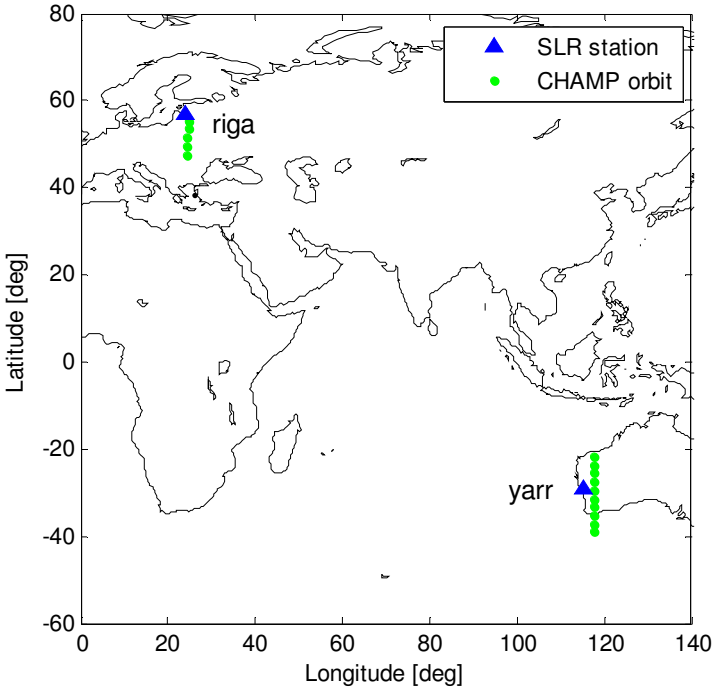

Figure 5.15 Geometry of two SLR stations and CHAMP orbits (Feb. 15, 2003).

Station		Position [m]	Velocity [m/yr]
Yarragadee	X	-2389006.924	-0.0470
	Y	5043329.339	0.0079
	Z	3078524.890	0.0488
Riga	X	3183895.938	-0.0221
	Y	1421497.041	0.0131
	Z	5322803.772	-0.0001

Table 5.10 The position and velocity of two SLR stations (1997.0).

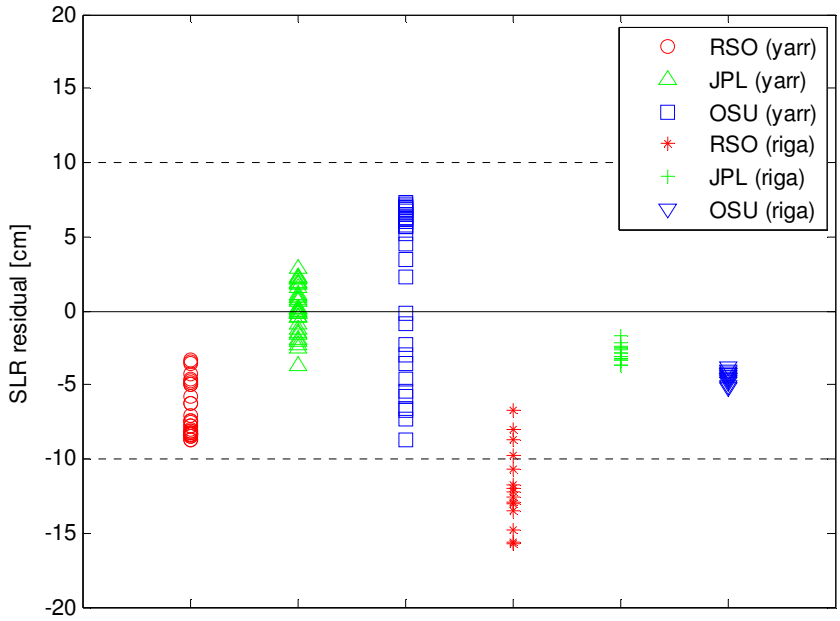

Figure 5.16 Comparison of the SLR residuals (Feb. 15, 2003).

Figure 5.16 shows the SLR residuals for two stations using three different orbit solutions, namely, the published RSO, the solution from JPL (denoted as JPL), and the dynamic orbit solution computed in this study (denoted as OSU). As can be seen in Figure 5.16 and Table 5.11, the dynamic solution of this study gives better results (up to more than two times) than the RSO in terms of the SLR residual RMS errors.

Station	Orbit	Mean [cm]	Std. [cm]	RMS [cm]
Yarragadee	RSO	-6.92	±1.71	±7.13
	JPL	0.14	±1.61	±1.62
	OSU	2.48	±5.36	±5.91
Riga	RSO	-11.97	±2.62	±12.25
	JPL	-2.83	±0.58	±2.89
	OSU	-4.42	±0.40	±4.44

Table 5.11 Statistics of the SLR residuals (Feb. 15, 2003).

For the comprehensive understanding of these results, three orbit solutions are compared to each other. Since the JPL orbit is provided in the 60-second intervals, the orbit comparison is done using this time interval. As can be seen in Table 5.12, the cross-comparison shows similar results for all three orbit solutions, although OSU is a little

closer to JPL than RSO. In particular, the bias of the radial component between JPL and OSU is almost negligible. Assuming that two orbit solutions (say A and B) are independent, the difference between the two solutions can be represented by (Boomkamp, 2003)

$$RMS_{AB} = \sqrt{RMS_A^2 + RMS_B^2}\ , \tag{5.16}$$

where RMS_A, RMS_B denote the RMS of differences between the (unknown) true CHAMP orbit and the orbit solution A and B, respectively. Therefore, the pair-wise value RMS can imply the true orbit errors.

The RMS error of the residuals of the triple-differenced ionosphere-free phase observations used in this study are at the level of ±1.6 cm, which is quite reasonable when compared to JPL's undifferenced ionosphere-free phase residuals of ±5-6 mm RMS error (Kuang, 2006). Based on the analyses performed in this chapter, the orbit accuracy estimated in this study is comparable to those from other analysis centers.

Solution pair		N [cm]	T [cm]	R [cm]	3D [cm]
RSO - JPL	Mean	0.48	-0.25	1.94	
	Std.	±3.68	±7.12	±3.29	±8.67
	RMS	±3.71	±7.13	±3.82	±8.90
RSO - OSU	Mean	0.76	-1.39	1.93	
	Std.	±3.80	±6.10	±3.33	±7.92
	RMS	±3.87	±6.25	±3.85	±8.30
JPL - OSU	Mean	-0.28	1.15	0.01	
	Std.	±3.19	±5.61	±2.93	±7.09
	RMS	±3.21	±5.72	±2.93	±7.19

Table 5.12 Orbit differences between various solutions (24 hours, 60 s interval).

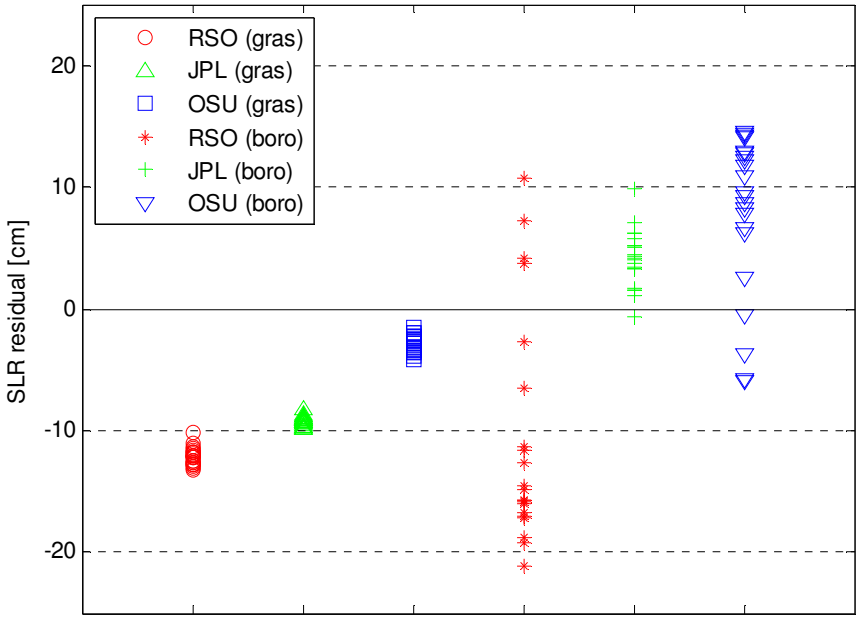

Figure 5.17 Comparison of the SLR residuals (Feb. 16, 2003).

Station	Orbit	Mean [cm]	Std. [cm]	RMS [cm]
Grasse	RSO	-12.15	±0.70	±12.17
	JPL	-9.25	±0.39	±9.26
	OSU	-2.87	±0.66	±2.95
Borowiec	RSO	-10.38	±9.30	±13.93
	JPL	4.00	±2.34	±4.64
	OSU	7.88	±6.54	±10.24

Table 5.13 Statistics of the SLR residuals (Feb. 16, 2003).

For further validation of the orbit solutions suggested in this study, another data set (16 February 2003, the following day) was processed with the dynamic approach. On this day, two SLR stations are available; Grasse (26 observations, 3.2 minutes) and Borowiec (22 observations, 2.3 minutes). As seen in Figure 5.17 and Table 5.13, the RMS error of the SLR residuals for the OSU solution for Grasse is less than ±3 cm, although 8 cm of bias is seen in Borowiec. However, as mentioned before, these results represent only a few minutes of coverage of the CHAMP orbit and are derived from only a few stations; thus, more comprehensive orbit validation by using SLR data over longer time periods (*i.e.*, considering numerous date arcs) is recommended in a future study.

According to Boomkamp (2003), the RMS absolute orbit error can be computed from the RMS error of the SLR residuals using the following empirical relationships:

$$RMS(orbit) = (1.52 \pm 0.18) RMS(slr), \tag{5.17}$$

which can be roughly understood by the geometric relation that there is a difference between the 3D orbit error vector and the SLR line-of-sight; thus, it can be considered as the lower limit of the 3D RMS orbit error.

CHAPTER 6

SUMMARY AND CONCLUSIONS

Notably, CHAMP is the first "authentic" LEO, given that it experiences much more perturbations because of its low altitude than satellites with higher altitudes. The precise orbit of CHAMP is estimated in this study in order to test different POD techniques based on GPS triple-differenced observations. The objective of this research was to estimate LEO orbits in near real-time to support GPS meteorology. Therefore, an accurate and efficient algorithm, as presented here, as well as its easy implementation, are important for this purpose. The triple-differenced observations, which are free from the cumbersome ambiguity-fixing step, are successfully applied in LEO orbit determination with far fewer unknown parameters, as compared to methods based on double-differenced, single-differenced or undifferenced measurements.

The widely used POD techniques include the kinematic, dynamic and reduced-dynamic approaches. It should be emphasized that new LEO precise orbit determination algorithms have been developed for all three methods and implemented in this study. This new approach is simple, fast and efficient, and includes no legacy software, and has been demonstrated to provide solutions of the accuracy equivalent to the existing solutions. The approach presented here is very easy to maintain and understand; and, if needed, it can be easily extended for more functionality. Simplicity, efficiency, easy maintenance, and no extra computational overhead are the primary advantages of this implementation, not to mention that it runs on a PC platform. The algorithms are ready to support near real-time operational LEO orbit determination and assure latency required by operational weather forecasting.

The kinematic method has its own benefit of being purely based on measurements, and not requiring complex force modeling. However, it is highly dependent on the quality and continuity of GPS data. Despite these drawbacks, the kinematic method, after backward filtering, satisfies the accuracy requirements pursued in this study. This is possible due to the insensitivity of the triple-differenced observations to the data quality, and careful modeling of correlation between the data point, as well as, optimal selection of ground station geometry.

The dynamic orbit, commonly used for POD, and less sensitive to the satellite's instantaneous perturbations, shows the best achievable accuracy. The modeling of the atmospheric drag force is crucial in the LEO dynamic orbit determination because it accounts for most of the nonconservative forces. The dynamic orbit has a predominantly large orbit error in the along-track component, because the most significant nonconservative force, which is, again, the drag force, is acting on the satellite in the direction opposite to the satellite motion. The proper modeling of the atmospheric drag, including the optimal arc length for the drag parameter estimation as addressed in this study, provides an orbit solution of about ±8 cm in 3D RMS error-of-fit with respect to the published RSO. The orbit errors, as a function of the degree/order of the geopotential model used, were also analyzed here. As expected, the higher the degree of the geopotential model, the better the results obtained; however, more sensitivity was observed for degree/order up to 70. The future studies should consider expanding the degree and order up to 200 or more, using for instance the newly published EIGEN-CG01C model. The different gravity models were not tested thoroughly in this study because the EIGEN2 gravity model is generated using CHAMP data only, and is thus assumed to be the most suitable for CHAMP dynamic orbit determination.

The reduced-dynamic technique with the wave algorithm shows slightly better results in its variance, but with a moderately larger bias in the along-track direction (about ±1 cm), resulting in similar statistics with the dynamic solution in 3D RMS errors. This is so because the dynamic approach, as used in this study, already includes the empirical force modeling for once- and twice-per-revolution parameters; thus, the unmodeled forces are assumed to be absorbed significantly by these parameters. Also, the wave filter is applied when the dynamic orbit solution has already converged. The discontinuities of the orbit update at each cycle need to be interpolated for smoother updates. The results indicate that the wave filter solution can be further improved as long as the biases are properly taken care of.

The internal consistency check shows that the redundant part before the main arc does not play an important role in the final orbit solution. This means that the accuracy orbit solution from 26 hours of arc is comparable to that from the 30-hour arc. Therefore, from the computational efficiency point of view, it is highly beneficial to estimate the initial state vector at the beginning of the target arc. Also, since there are only 121 unknowns (as mentioned in the previous chapter), the reduction of the observations takes the majority of the processing time, which is almost linearly increasing with the length of the processing arc.

The estimated orbit solution with once- and twice-per-revolution empirical forces significantly reduced the orbit errors at both frequencies. However, the actual correlation between the along-track and the radial components for the twice-per-revolution parameters was not clearly verified; this should be studied more rigorously in the future studies. The time interval for the estimation of the atmospheric drag parameters should not exceed 2 hours in order to obtain a precise orbit solution, because of the rapid change

in the atmospheric density along the trajectory. The CHAMP velocity results prove to fit the reference RSO solution with RMS errors better than ±0.073 mm/s in each component.

An efficient ground station network optimization algorithm was developed in this study, based on the network optimization theory. Although the ground station network should be chosen according to data availability and the quality of the GPS measurements, it should also be supported by the theoretical foundation. With this algorithm, the criteria to configure the ground station network are suggested; the algorithm is also applicable to the augmentation of the positioning satellites, as discussed in Chapter 4.

The computed orbits are validated independently using the SLR residuals. The SLR residuals are considered as an absolute orbit error in the absence of the true orbit. After applying the tropospheric correction for the laser signals, the measurements are compared with the geometric range between the estimated/interpolated CHAMP orbit and the SLR station. The results prove that the dynamic orbit computed in this study is comparable to the orbit solutions from other analysis centers, such as GFZ and JPL, which process CHAMP data routinely. This is also confirmed by the hypothesis testing to establish the consistency of the orbit solutions.

The precise orbit determination techniques presented and used in this study are believed to be applicable to other LEOs, especially the GRACE satellites which are orbiting with almost the same altitude and inclination. Also, the upcoming gravity mission satellite, GOCE (Gravity field and steady-state Ocean Circulation Explorer) which has a mean altitude of 250 km, can also use the techniques implemented here with further refined modeling of the atmospheric drag, higher degree/order geopotential models, and the inclusion of the Earth's radiation.

Currently, most LEO orbits are estimated separately by fixing GPS orbits and ground station coordinates; this can result in a bias in the final LEO orbit solution. As pointed out by Zhu et al. (2004), however, it would be desirable to estimate GPS and LEO orbits in one simultaneous least-squares solution (integrated or one-step adjustment), together with the coordinates of the ground stations, and, if needed, other Earth system parameters, such as geocenter variation and low-degree gravity field parameters. This is so, because the LEO orbit solution can be strengthened by the strong algebraic correlations between its ephemerides throughout the arc and the GPS constellation as well as the ground reference frame (*ibid.*). Therefore, the POD approaches in this study need to be reformulated and executed to include better constraints for multi-satellite missions, such as COSMIC, in the future.

Another issue to be considered is the fact that the accelerometer and attitude information from the CHAMP satellite is not used in this study. Theoretically, the accelerometer data should be suitable to replace all the nonconservative forces. The accelerometer data, however, are published at 10-second intervals by smoothing the sensed acceleration during that interval; but, in reality, there could be many more perturbations during the 10-second interval. Therefore, this information cannot be used to

replace completely the nonconservative force modeling. In spite of this drawback, use of the accelerometer data should be investigated in the future since these data will be improved further and can serve as useful information in orbit determination, indeed.

BIBLIOGRAPHY

Anthes, R.A., C. Rocken and Y.-H. Kuo (2000): Applications of COSMIC to Meteorology and Climate. Terrestrial, Atmospheric and Oceanic Sciences, Vol. 11, No. 1, pp. 115-156.

Bae, T.S., J.H. Kwon and D.A. Grejner-Brzezinska (2002): Data Screening and Quality Analysis for Kinematic Orbit Determination of CHAMP Satellite. ION National Technical Meeting, San Diego, CA, CD-ROM.

Bae, T.-S. (2005a): Optimized Network of Ground Stations for LEO Orbit Determination. ION National Technical Meeting, San Diego, CA, CD-ROM.

Bae, T.-S. (2005b): LEO Dynamic Orbit Enhancement Using Atmospheric and Empirical Force Modeling. ION GNSS, Long Beach, CA, CD-ROM.

Bertiger, W.I., Y.E. Bar-Sever, E.J. Christensen, E.S. Davis, J.R. Guinn, B.J. Haines, R.W. Ibanez-Meier, J.R. Jee, S.M. Lichten, W.G. Melbourne, R.J. Muellerschoen, T.N. Munson, Y. Vigue, S.C. Wu, T.P. Yunck, B.E. Schutz, P.A.M. Abusali, H.J. Rim, M.M. Watkins and P. Willis (1994): GPS precise tracking of TOPEX/POSEIDON: Results and implications. Journal of Geophysical Research, Vol. 99, No. C12, pp. 24,449-24,464.

Bisnath, S.B. and R.B. Langley (2001): Precise Orbit Determination of Low Earth Orbiters with GPS Point Positioning. ION National Technical Meeting, Long Beach, CA, CD-ROM.

Bisnath, S. (2004): Precise Orbit Determination of Low Earth Orbiters with a Single GPS Receiver-Based, Geometric Strategy. Ph.D. dissertation, Department of Geodesy and Geomatics Engineering Technical Report No. 220, University of New Brunswick, Fredericton, New Brunswick, Canada.

Blewitt, G. (1990): An Automatic Editing Algorithm for GPS Data. Geophysical Research Letters, Vol. 17, No. 3, pp. 199-202.

Bock, H. (2003): Efficient methods for determining precise orbits of Low Earth Orbiters using the Global Positioning System. Geodätisch-geophysikalische Arbeiten in der

Schweiz, Schweizerische Geodätisch Kommission, Vol. 65.

Boomkamp, H. (2003): The CHAMP Orbit Comparison Campaign. In: Reigber, Lühr and Schwintzer (eds.), *First CHAMP Mission Results for Gravity, Magnetic and Atmospheric Studies*, pp. 53-58, Springer-Verlag Berlin Heidelberg.

Boomkamp, H. (2004): Personal communications.

Brown, R.G. and P.Y.C. Hwang (1997): *Introduction to Random Signals and Applied Kalman Filtering* (3rd edn.). John Wiley & Sons, Inc., New York.

Byun, S.H. (1998): Satellite orbit determination using GPS carrier phase in pure kinematic mode. Ph.D. Dissertation, The University of Texas at Austin, TX.

Byun, S.H. and B.E. Schutz (2001): Improving satellite orbit solution using double-differenced GPS carrier phase in kinematic mode. Journal of Geodesy, **75**, 533-543.

Byun, S.H. (2003): Satellite orbit determination using triple-differenced GPS carrier phase in pure kinematic mode. Journal of Geodesy, **76**, 569-585.

Capitaine, N. (2002): Comparison of "Old" and "New" Concepts: The Celestial Intermediate Pole and Earth Orientation Parameters. In: Capitaine et al. (eds.), IERS Technical Note No. 29, Verlag des Bundesamts für Kartographie und Geodäsie, Frankfurt am Main.

Caspary, W. (1987): Concepts of Network and Deformation Analysis. Monograph No. 11, School of Surveying, University of New South Wales, Kensington (Australia).

Chadwell, C.D. (1995): Investigation of Stochastic Models to Improve the Global Positioning System Satellite Orbits. Report No. 429, Department of Geodetic Science and Surveying, The Ohio State University, Columbus, Ohio.

CHAMP (2002): Format Description: The CHAMP Data Format. http://www.gfz-potsdam.de/pb1/op/champ/docs_CHAMP/CH-GFZ-FD-001.pdf.

CHAMP (2005): CHAMP homepage. Available at: http://www.gfz-potsdam.de/pb1/op/champ/index_CHAMP.html, accessed April.

Colombo, O.L. (1981): Numerical methods for harmonic analysis on the sphere. Report No. 310, Department of Geodetic Science and Surveying, The Ohio State University, Columbus, Ohio.

Colombo, O.L. (2002): Personal communications.

COSMIC (2006): FORMOSAT-3/COSMIC homepage. Available at: http://www.cosmic.ucar.edu/, accessed May.

Cruickshank, D.R. (1998): Genetic Model Compensation: Theory and Applications. Ph.D. Dissertation, The University of Colorado at Boulder, CO.

Davis, G.W. (1996): GPS-Based Precision Orbit Determination for Low Altitude

Geodetic Satellites. Ph.D. Dissertation, The University of Texas at Austin, TX.

Eren, K. (1986): GPS Geodetic Network Adjustment Using Triple Difference Observations and A-Priori Information. Manuscripta Geodaetica, Vol. 11, pp. 289-292.

Eren, K. (1987): Geodetic Network Adjustment Using Triple Difference Observations and A-Priori Stochastic Information. Technical Report No. 1, Institute of Geodesy, University of Stuttgart, Germany.

Fontana, R.D., W. Cheung and T. Stansell (2001): The Modernized L2 Civil Signal: Leaping Forward in the 21st Century. *GPS World*.

Ge, M., E. Calais and J. Haase (2002): Sensitivity of zenith total delay accuracy to GPS orbit errors and implications for near-real-time GPS meteorology. Journal of Geophysical Research, Vol. 107, No. D16, 4315.

Goad, C.C. and L. Goodman (1974): A Modified Hopfield Tropospheric Refraction Correction Model. Presented at the Fall Annual Meeting of the American Geophysical Union, San Francisco, CA.

GPS/MET (2006): GPS/MET homepage. Available at: http://www.cosmic.ucar.edu/gpsmet/, accessed May.

GRACE (2005): GRACE homepage. Available at: http://www.gfz-potsdam.de/pb1/op/grace/index_GRACE.html, accessed April.

Grafarend, E. (1972): Genauigkeitsmaβe geodätischer Netze. Publ. of the German Geodetic Comm., DGK A-73, München.

Grafarend, E. (1974): Optimization of geodetic networks. Bolletino di Geodesia a Science Affini, Vol. 33, No. 4, pp. 351-406.

Grafarend, E. and B. Schaffrin (1979): Kriterion-Matrizen I – zweidimensionale homogene und isotrope geodätische Netze. Zeitschrift für Vermessungswesen, Vol. 104, pp. 133-149.

Grejner-Brzezinska, D. (1995): Analysis of GPS data processing techniques: In search of optimized strategy of orbit and Earth rotation parameter recovery. Report No. 432, Department of Geodetic Science and Surveying, The Ohio State University, Columbus, Ohio.

Grejner-Brzezinska, D.A., S. Ge, J.H. Kwon, C.K. Shum and C.Y. Zhao (2001): GPS/LEO Rapid Orbit Determination in Support of GPS Meteorology: Status and Future Plans. In: Adam and Schwarz (eds.), *Vistas for Geodesy in the New Millennium*, pp. 316-321, Springer-Verlag Berlin Heidelberg.

Grejner-Brzezinska, D.A., J.H. Kwon and C.K. Shum (2002): A Practical Algorithm for LEO Orbit Determination. Navigation, Vol. 49, No. 3, pp. 127-135; also in:

Proceedings of ION GPS, Salt Lake City, September, 2001, CD-ROM, pp. 3139-3148.

Grejner-Brzezinska, D., C.-K. Hong and T.-S. Bae (2004): Improving Kinematic LEO POD with the Use of a Space-Based and Ground-Based GPS Transceiver Constellation: Feasibility Study. ION National Technical Meeting, San Diego, CA.

Hedin, A.E. (1991): Extension of the MSIS thermosphere model into the middle and lower atmosphere. Journal of Geophysical Research, 96(A2), 1159-1172.

Heiskanen, W.A. and H. Moritz (1967): *Physical Geodesy*. W.H. Freeman, San Franscisco.

Hofmann-Wellenhof, B., H. Lichtenegger and J. Collins (2004): *GPS: Theory and Practice* (5th edn.). Springer-Verlag New York.

Hugentobler, U., S. Schaer and P. Fridez (eds.) (2001): Bernese GPS Software Version 4.2. Astronomical Institute University of Berne, Switzerland.

ICESat (2005): ICESat homepage. Available at: http://icesat.gsfc.nasa.gov/intro.html, accessed April.

IERS Conventions (2003): See McCarthy and Petit (2003).

JASON (2005): JASON-1 homepage. Available at: http://topex-www.jpl.nasa.gov/mission/jason-1.html, accessed April.

Jekeli, C. (1996): Spherical harmonic analysis, aliasing, and filtering. Journal of Geodesy, Vol. 70, pp. 214-223.

Jekeli, C. (2001): *Inertial Navigation Systems with Geodetic Applications*. Walter de Gruyter, Berlin New York.

Jekeli, C. (2005): *Geometric Reference Systems in Geodesy*. Lecture Notes (GS660), Department of Civil and Environmental Engineering and Geodetic Science, The Ohio State University.

Kang, Z., S. Bettadpur, B. Tapley and J. Ries (2003): Determination of CHAMP Accelerometer Calibration Parameters. In: Reigber, Lühr and Schwintzer (eds.), *First CHAMP Mission Results for Gravity, Magnetic and Atmospheric Studies*, pp. 19-25, Springer-Verlag Berlin Heidelberg.

König, R., S. Zhu, Ch. Reigber, K.-H. Neumayer, H. Meixner, R. Galas, G. Baustert and P. Schwintzer (2002): CHAMP Rapid Orbit Determination for GPS Atmospheric Limb Sounding. Advances in Space Research, Vol. 30, No. 2, pp. 289-293.

Kuang, D., Y. Bar-Sever, W. Bertiger, S. Desai, B. Haines, B. Iijima, G. Kruizinga, T. Meehan and L. Romans (2001): Precise Orbit Determination for CHAMP using GPS Data from Blackjack Receiver. ION National Technical Meeting, Long Beach, CA.

Kuang, D. (2006): Personal communications.

Kwon, J. (1997): The Orbit Determination Software GODIVA at The Ohio State University: A Review. Report No. 438, Department of Geodetic Science and Surveying, The Ohio State University, Columbus, Ohio.

Kwon, J., D. Grejner-Brzezinska and C.-K. Hong (2002): Kinematic Orbit Determination of Low Earth Orbiter using Triple Differences. ION National Technical Meeting, San Diego, CA.

Kwon, J., D. Grejner-Brzezinska, T.-S. Bae and C.-K. Hong (2003): Triple Difference Approach to Low Earth Orbiter Precision Orbit Determination. Journal of Navigation, Vol. 56, pp. 456-473.

Leandro, R., M. Santos and R.B. Langley (2006): UNB Neutral Atmosphere Models: Development and Performance. ION National Technical Meeting, Monterey, CA.

Leick, A. (1995): *GPS Satellite Surveying* (2nd edn.). John Wiley & Sons Inc., New York.

Lundberg, J.B. (1984): Computational Errors and Their Control in the Determination of Satellite Orbits. Ph.D. Dissertation, The University of Texas at Austin, TX.

McCarthy, D.D. and G. Petit (2003): IERS Technical Note No. 32. IERS Conventions (2003), IERS Conventions Centre, Verlag des Bundesamts für Kartographie und Geodäsie, Frankfurt am Main.

McCarthy, J.J., D.E. Pavlis, J.A. Marshall, S.B. Luthcke, L.S. Tsaoussi, S. Rowton and D.A. Williams (1991): GEODYN II Systems Description. Vol. 1, Space Geodesy Branch, Code 926, Goddard Space Flight Center, Greenbelt, MD.

Montenbruck, O. and E. Gill (2001): Satellite Orbits: Models, Methods, and Applications. Springer-Verlag Berlin Heidelberg New York.

Montenbruck, O. and R. Kroes (2003): In-flight performance analysis of the CHAMP BlackJack GPS Receiver. GPS Solutions, **7**, 74-86.

MSIS (2004): MSIS homepage. Available at: http://uap-www.nrl.navy.mil/models_web/msis/msis_home.htm, accessed August.

Novak, P. (2001): L2 and L5 Civil Signal Industry Day. http://www.navcen.uscg.gov/gps/modernization/industryday.htm.

Reigber, Ch., H. Lühr and P. Schwintzer (2002): CHAMP MISSION STATUS. Advances in Space Research, Vol. 30, No. 2, pp. 129-134.

Remondi, B.W. and G. Brown (2000): Triple Differencing with Kalman Filtering: Making It Work. GPS Solutions, Vol. 3, No. 3, pp. 58-64.

Rocken, C., F.S. Solheim, R.H. Ware, M. Exner, D. Martin and M. Rothacher (1995): Application of IGS Data to GPS Sensing of the Atmosphere for Weather and Climate Research. Proceeding for the 1995 IGS Meeting, Potsdam, Germany.

Salychev, O.S. and B. Schaffrin (1992): New Filter Approaches for GPS/INS Integration. In: Kumar and Fell (eds.), Proc. of the 6th International Geodetic Symposium on Satellite Positioning, Vol. II, pp. 670-680, Columbus, Ohio.

Salychev, O.S. (1998): *Inertial Systems in Navigation and Geophysics*. Bauman MSTU Press, Moscow.

Schaffrin, B. (1985): Network Design. In: Grafarend and Sansò (eds.), *Optimization and Design of Geodetic Networks*, Springer-Verlag Berlin Heidelberg New York Tokyo.

Schaffrin, B. and E. Grafarend (1986): Generating Classes of Equivalent Linear Models by Nuisance Parameter Elimination. Manuscripta Geodaetica, Vol. 11, pp. 262-271.

Schaffrin, B. (1995): A Generalized Lagrange Function Approach to Include Fiducial Constraints. Zeitschrift für Vermessungswesen, Vol. 120, pp. 325-333.

Schaffrin, B. (2002): Adjustment Computations. Lecture Notes (GS651), The Ohio State University, Columbus, Ohio.

Schmitt, G. (1980): Second Order Design of Free Distance Networks Considering Different Types of Criterion Matrices. Bull. Geod., **54**, pp. 531-543.

Schutz, B.E., B.D. Tapley, P.A.M. Abusali and H.J. Rim (1994): Dynamic orbit determination using GPS measurements from TOPEX/POSEIDON. Geophysical Research Letters, Vol. 21, No. 19, pp. 2,179-2,182.

Sinclair, A.T. (1997): Re-Statement of Herstmonceux Normal Point Recommendation. International Laser Ranging Service (ILRS), http://ilrs.gsfc.nasa.gov/products_formats_procedures/normal_point/np_algo.html.

Strang, G. and K. Borre (1997): *Linear Algebra, Geodesy, and GPS*. Wellesley-Cambridge Press.

Švehla, D. and M. Rothacher (2001): CHAMP Double-Difference Kinematic POD with Ambiguity Resolution. In: Reigber, Lühr and Schwintzer (eds.), *First CHAMP Mission Results for Gravity, Magnetic and Atmospheric Studies*, pp. 70-77, Springer-Verlag Berlin Heidelberg.

Švehla, D. and M. Rothacher (2003): Kinematic and reduced-dynamic precise orbit determination of low earth orbiters. Advances in Geosciences, **1**, 47-56.

Syndergaard, S. (2005): Introduction to GPS Radio Occultation. FORMOSAT-3/COSMIC Science Summer Camp, Taipei, Taiwan.

Tapley, B.D. and D.S. Ingram (1973): Orbit Determination in the Presence of Unmodeled Accelerations. IEEE Transaction on Automatic Control, Vol. AC-18, No. 4, pp. 369-373.

Tapley, B.D., J.C. Ries, G.W. Davis, R.J. Eeanes, B.E. Schutz, C.K. Shum, M.M. Watkins,

J.A. Marshall, R.S. Nerem, B.H. Putney, S.M. Klosko, S.B. Luthcke, D. Pavlis, R.G. Williamson and N.P. Zelensky (1994): Precise orbit determination for TOPEX/ POSEIDON. Journal of Geophysical Research, Vol. 99, No. C12, 24,383-24,404.

Tapley, B.D., B.E. Schutz and G.H. Born (2004): *Statistical Orbit Determination*. Elsevier Academic Press, San Diego.

Tscherning, C.C., R.H. Rapp and C. Goad (1983): A comparison of methods for computing gravimetric quantities from high degree spherical harmonic expansions. Manuscripta Geodaetica, Vol. 8, pp. 249-272.

Wickert, J., T. Schmidt, G. Beyerle, R. König, C. Reigber and N. Jakowski (2004): The radio occultation experiment aboard CHAMP: Operational data analysis and validation of vertical atmospheric profiles. Journal of Meteorological Society of Japan, Vol. 82, No. 1B, pp. 381-395.

Willis, P., Y.E. Bar-Sever and G. Tavernier (2005): DORIS as a potential part of a Global Geodetic Observing System. Journal of Geodynamics, Vol. 40, pp. 494-501.

Wimmer, H. (1982): Ein Beitrag zur Gewichtsoptimierung geodätischer Netze. Publ. of the German Geodetic Comm., DGK C-269, München.

Wu, S.C., T.P. Yunck and C.L. Thornton (1991): Reduced-Dynamic Technique for Precise Orbit Determination of Low Earth Satellites. Journal of Guidance, Control, and Dynamics, Vol. 14, No. 1, pp. 24-30.

Yunck, T.P., S. Wu, J. Wu and C. Thornton (1990): Precise Tracking of Remote Sensing Satellites With the Global Positioning System. IEEE Transaction on Geoscience and Remote Sensing, Vol. 28, No. 1, pp. 108-116.

Yunck, T.P., W.I. Bertiger, S.C. Wu, Y.E. Bar-Sever, E.J. Christensen, B.J. Haines, S.M. Lichten, R.J. Muellerschoen, Y. Vigue and P. Willis (1994): First assessment of GPS-based reduced dynamic orbit determination on TOPEX/POSEIDON. Geophysical Research Letters, Vol. 21, No. 7, pp. 541-544.

Zhao, C.Y. (1998): The sensitivity of atmospheric temperature retrieved from radio occultation technique to orbit errors of GPS and LEO satellites. Scientific Technical Report STR98/23, GeoForschungsZentrum Potsdam, Germany.

Zhu, S., Ch. Reigber and R. König (2004): Integrated adjustment of CHAMP, GRACE, and GPS data. Journal of Geodesy, **78**, 103-108.

APPENDIX A

THE PARTIAL DERIVATIVES OF THE GEOPOTENTIAL

Let V be the gravitational potential (see, Heiskanen and Moritz (1967), Eq. (2-39)) that can be represented as a function of (r,θ,λ):

$$V(r,\theta,\lambda)=\frac{kM}{r}\sum_{n=0}^{n_{\max}}\sum_{m=0}^{n}\left(\frac{R}{r}\right)^{n}\left(\overline{C}_{nm}\cos m\lambda+\overline{S}_{nm}\sin m\lambda\right)\overline{P}_{nm}(\cos\theta), \tag{A.1}$$

where

V: the gravitational potential;
kM: the product of the gravitational constant and the mass of the Earth;
R: the mean radius of the Earth;
r: the radial distance from the center of the Earth;
θ,λ: the geocentric co-latitude and longitude, respectively;
$\overline{P}_{nm}$: the fully normalized associated Legendre function;
n,m: the degree and order of $\overline{P}_{nm}$, respectively;
$n_{\max}$: the maximum degree;
$\overline{C}_{nm},\overline{S}_{nm}$: the spherical harmonic coefficients for each degree *n* and order *m*.

The variational partials of the gravitational forces with respect to the position vector

can be expressed by the chain rule (McCarthy et al., 1991):

$$\frac{\partial \ddot{\mathbf{r}}}{\partial \mathbf{r}^T} = \begin{pmatrix} \partial \ddot{r}_x/\partial x & \partial \ddot{r}_x/\partial y & \partial \ddot{r}_x/\partial z \\ \partial \ddot{r}_y/\partial x & \partial \ddot{r}_y/\partial y & \partial \ddot{r}_y/\partial z \\ \partial \ddot{r}_z/\partial x & \partial \ddot{r}_z/\partial y & \partial \ddot{r}_z/\partial z \end{pmatrix}$$
$$= \begin{pmatrix} \partial^2 V/\partial x^2 & \partial^2 V/\partial x \partial y & \partial^2 V/\partial x \partial z \\ \partial^2 V/\partial y \partial x & \partial^2 V/\partial y^2 & \partial^2 V/\partial y \partial z \\ \partial^2 V/\partial z \partial x & \partial^2 V/\partial z \partial y & \partial^2 V/\partial z^2 \end{pmatrix} \tag{A.2}$$
$$= C_1^T U_2 C_1 + \frac{\partial V}{\partial r} C_{21} + \frac{\partial V}{\partial \theta} C_{22} + \frac{\partial V}{\partial \lambda} C_{23} ,$$

where

$$U_2 = \begin{pmatrix} \partial^2 V/\partial r^2 & \partial^2 V/\partial r \partial \theta & \partial^2 V/\partial r \partial \lambda \\ \partial^2 V/\partial \theta \partial r & \partial^2 V/\partial \theta^2 & \partial^2 V/\partial \theta \partial \lambda \\ \partial^2 V/\partial \lambda \partial r & \partial^2 V/\partial \lambda \partial \theta & \partial^2 V/\partial \lambda^2 \end{pmatrix}, \tag{A.3}$$

$$C_1 = \begin{pmatrix} \partial r/\partial x & \partial r/\partial y & \partial r/\partial z \\ \partial \theta/\partial x & \partial \theta/\partial y & \partial \theta/\partial z \\ \partial \lambda/\partial x & \partial \lambda/\partial y & \partial \lambda/\partial z \end{pmatrix}, \tag{A.4}$$

$$C_{21} = \begin{pmatrix} \partial^2 r/\partial x^2 & \partial^2 r/\partial x \partial y & \partial^2 r/\partial x \partial z \\ \partial^2 r/\partial y \partial x & \partial^2 r/\partial y^2 & \partial^2 r/\partial y \partial z \\ \partial^2 r/\partial z \partial x & \partial^2 r/\partial z \partial y & \partial^2 r/\partial z^2 \end{pmatrix}, \tag{A.5}$$

$$C_{22} = \begin{pmatrix} \partial^2 \theta/\partial x^2 & \partial^2 \theta/\partial x \partial y & \partial^2 \theta/\partial x \partial z \\ \partial^2 \theta/\partial y \partial x & \partial^2 \theta/\partial y^2 & \partial^2 \theta/\partial y \partial z \\ \partial^2 \theta/\partial z \partial x & \partial^2 \theta/\partial z \partial y & \partial^2 \theta/\partial z^2 \end{pmatrix}, \tag{A.6}$$

$$C_{23}=\begin{pmatrix} \partial^2\lambda/\partial x^2 & \partial^2\lambda/\partial x\partial y & \partial^2\lambda/\partial x\partial z \\ \partial^2\lambda/\partial y\partial x & \partial^2\lambda/\partial y^2 & \partial^2\lambda/\partial y\partial z \\ \partial^2\lambda/\partial z\partial x & \partial^2\lambda/\partial z\partial y & \partial^2\lambda/\partial z^2 \end{pmatrix}. \tag{A.7}$$

The partial derivatives of the potential with respect to the spherical coordinates, (r,θ,λ), can easily be obtained as

$$\frac{\partial V}{\partial r}=-\frac{kM}{r^2}\left[1+\sum_{n=2}^{n_{\max}}\sum_{m=0}^{n}(n+1)\left(\frac{R}{r}\right)^n\left(\bar{C}_{nm}\cos m\lambda+\bar{S}_{nm}\sin m\lambda\right)\bar{P}_{nm}(\cos\theta)\right], \tag{A.8}$$

$$\frac{\partial V}{\partial \theta}=\frac{kM}{r}\sum_{n=2}^{n_{\max}}\sum_{m=0}^{n}\left(\frac{R}{r}\right)^n\left(\bar{C}_{nm}\cos m\lambda+\bar{S}_{nm}\sin m\lambda\right)\bar{P}'_{nm}(\cos\theta), \tag{A.9}$$

$$\frac{\partial V}{\partial \lambda}=\frac{kM}{r}\sum_{n=2}^{n_{\max}}\sum_{m=0}^{n}\left(\frac{R}{r}\right)^n\left(\bar{S}_{nm}\cos m\lambda-\bar{C}_{nm}\sin m\lambda\right)m\bar{P}_{nm}(\cos\theta), \tag{A.10}$$

$$\frac{\partial^2 V}{\partial r^2}=\frac{2kM}{r^3}+\frac{kM}{r^3}\sum_{n=2}^{n_{\max}}\sum_{m=0}^{n}(n+1)(n+2)\left(\frac{R}{r}\right)^n\left(\bar{C}_{nm}\cos m\lambda+\bar{S}_{nm}\sin m\lambda\right)\bar{P}_{nm}(\cos\theta), \tag{A.11}$$

$$\frac{\partial^2 V}{\partial r\partial \theta}=-\frac{kM}{r^2}\sum_{n=2}^{n_{\max}}\sum_{m=0}^{n}(n+1)\left(\frac{R}{r}\right)^n\left(\bar{C}_{nm}\cos m\lambda+\bar{S}_{nm}\sin m\lambda\right)\bar{P}'_{nm}(\cos\theta), \tag{A.12}$$

$$\frac{\partial^2 V}{\partial r\partial \lambda}=-\frac{kM}{r^2}\sum_{n=2}^{n_{\max}}\sum_{m=0}^{n}(n+1)\left(\frac{R}{r}\right)^n\left(-\bar{C}_{nm}\sin m\lambda+\bar{S}_{nm}\cos m\lambda\right)m\bar{P}_{nm}(\cos\theta), \tag{A.13}$$

$$\frac{\partial^2 V}{\partial \theta^2}=\frac{kM}{r}\sum_{n=2}^{n_{\max}}\sum_{m=0}^{n}\left(\frac{R}{r}\right)^n\left(\bar{C}_{nm}\cos m\lambda+\bar{S}_{nm}\sin m\lambda\right)\bar{P}''_{nm}(\cos\theta), \tag{A.14}$$

$$\frac{\partial^2 V}{\partial \theta\partial \lambda}=\frac{kM}{r}\sum_{n=2}^{n_{\max}}\sum_{m=0}^{n}\left(\frac{R}{r}\right)^n\left(-\bar{C}_{nm}\sin m\lambda+\bar{S}_{nm}\cos m\lambda\right)m\bar{P}'_{nm}(\cos\theta), \tag{A.15}$$

$$\frac{\partial V}{\partial \lambda^2} = -\frac{kM}{r}\sum_{n=2}^{n_{\max}}\sum_{m=0}^{n}\left(\frac{R}{r}\right)^n \left(\bar{C}_{nm}\cos m\lambda + \bar{S}_{nm}\sin m\lambda\right) m^2 \bar{P}_{nm}(\cos\theta)\,. \tag{A.16}$$

The computation of $\cos m\lambda$ and $\sin m\lambda$ can be accomplished recursively by the following relationships:

$$\begin{aligned} \cos m\lambda &= \cos\lambda\cos\left((m-1)\lambda\right) - \sin\lambda\sin\left((m-1)\lambda\right) \\ \sin m\lambda &= \sin\lambda\cos\left((m-1)\lambda\right) + \cos\lambda\sin\left((m-1)\lambda\right). \end{aligned} \tag{A.17}$$

The components of Eqs. (A.4)-(A.7) and the transformation matrix between the spherical coordinates and Cartesian coordinates can be represented based on the relationship between the two coordinate systems, specifically

$$r = \sqrt{x^2 + y^2 + z^2}\,, \tag{A.18}$$

$$\theta = \cos^{-1}\frac{z}{r}, \tag{A.19}$$

$$\lambda = \tan^{-1}\frac{y}{x}. \tag{A.20}$$

From (A.18)-(A.20) the transformation matrix from the spherical coordinates to the Cartesian coordinates will be given by

$$R = \begin{bmatrix} \frac{\partial r}{\partial x} & \frac{\partial \theta}{\partial x} & \frac{\partial \lambda}{\partial x} \\ \frac{\partial r}{\partial y} & \frac{\partial \theta}{\partial y} & \frac{\partial \lambda}{\partial y} \\ \frac{\partial r}{\partial z} & \frac{\partial \theta}{\partial z} & \frac{\partial \lambda}{\partial z} \end{bmatrix} = \begin{bmatrix} \frac{x}{r} & \frac{xz}{r^2\sqrt{x^2+y^2}} & -\frac{y}{x^2+y^2} \\ \frac{y}{r} & \frac{yz}{r^2\sqrt{x^2+y^2}} & \frac{x}{x^2+y^2} \\ \frac{z}{r} & -\frac{\sqrt{x^2+y^2}}{r^2} & 0 \end{bmatrix}. \tag{A.21}$$

The second derivatives of the (r,θ,λ) with respect to (x,y,z) can be obtained by

$$\frac{\partial^2 r}{\partial x^2} = -\frac{x^2}{r^3} + \frac{1}{r}, \quad \frac{\partial^2 r}{\partial y^2} = -\frac{y^2}{r^3} + \frac{1}{r}, \quad \frac{\partial^2 r}{\partial z^2} = -\frac{z^2}{r^3} + \frac{1}{r}, \tag{A.22}$$

$$\frac{\partial^2 r}{\partial x \partial y} = -\frac{xy}{r^3}, \quad \frac{\partial^2 r}{\partial x \partial z} = -\frac{xz}{r^3}, \quad \frac{\partial^2 r}{\partial y \partial z} = -\frac{yz}{r^3}, \tag{A.23}$$

$$\frac{\partial^2 \lambda}{\partial x^2} = \frac{2xy}{\left(x^2+y^2\right)^2}, \quad \frac{\partial^2 \lambda}{\partial y^2} = -\frac{2xy}{\left(x^2+y^2\right)^2}, \quad \frac{\partial^2 \lambda}{\partial z^2} = 0, \tag{A.24}$$

$$\frac{\partial^2 \lambda}{\partial x \partial y} = \frac{-x^2+y^2}{\left(x^2+y^2\right)^2}, \quad \frac{\partial^2 \lambda}{\partial x \partial z} = 0, \quad \frac{\partial^2 \lambda}{\partial y \partial z} = 0, \tag{A.25}$$

$$\frac{\partial^2 \theta}{\partial x^2} = -\frac{x^2 z}{\sqrt{x^2+y^2}}\left(\frac{1}{r^2(x^2+y^2)} + \frac{2}{r^4} - \frac{1}{r^2 x^2}\right), \tag{A.26}$$

$$\frac{\partial^2 \theta}{\partial y^2} = -\frac{y^2 z}{\sqrt{x^2+y^2}}\left(\frac{1}{r^2(x^2+y^2)} + \frac{2}{r^4} - \frac{1}{r^2 y^2}\right), \tag{A.27}$$

$$\frac{\partial^2 \theta}{\partial z^2} = \frac{2z\sqrt{x^2+y^2}}{r^4}, \tag{A.28}$$

$$\frac{\partial^2 \theta}{\partial x \partial y} = -\frac{xyz}{\sqrt{x^2+y^2}}\left(\frac{1}{r^2(x^2+y^2)} + \frac{2}{r^4}\right), \tag{A.29}$$

$$\frac{\partial^2 \theta}{\partial x \partial z} = -\frac{x}{\sqrt{x^2+y^2}}\left(\frac{2z^2}{r^4} - \frac{1}{r^2}\right), \tag{A.30}$$

$$\frac{\partial^2 \theta}{\partial y \partial z} = -\frac{y}{\sqrt{x^2+y^2}}\left(\frac{2z^2}{r^4} - \frac{1}{r^2}\right). \tag{A.31}$$

APPENDIX B

THE FULLY NORMALIZED ASSOCIATED LEGENDRE FUNCTIONS

The fully normalized associated Legendre functions are convenient to handle, thus, widely used in practice. The main advantage of the fully normalized spherical harmonics is that the average square of any fully normalized harmonic is a unity, where the average is taken over the sphere (Heiskanen and Moritz, 1967). The recursive method of computing these functions has been developed and tested by many researchers, such as Colombo (1981), Tscherning et al. (1983) and Jekeli (1996). These functions are summarized as follows:

1) $\overline{P}_{n,m}(\cos\theta)$

$$\overline{P}_{n,n}(\cos\theta) = \sqrt{\frac{2n+1}{2n}}\,\sin\theta\,\overline{P}_{n-1,n-1}(\cos\theta)\,, \quad (n=m) \tag{B.1}$$

$$\overline{P}_{n,n-1}(\cos\theta) = \sqrt{2n+1}\,\cos\theta\,\overline{P}_{n-1,n-1}(\cos\theta)\,, \quad (n=m+1) \tag{B.2}$$

$$\begin{aligned}\overline{P}_{n,m}(\cos\theta) = {} & \sqrt{\frac{(2n-1)(2n+1)}{(n-m)(n+m)}}\,\cos\theta\,\overline{P}_{n-1,m}(\cos\theta) \\ & -\sqrt{\frac{(2n+1)(n+m-1)(n-m-1)}{(2n-3)(n-m)(n+m)}}\,\overline{P}_{n-2,m}(\cos\theta)\,,\end{aligned} \quad (n \geq m+2) \tag{B.3}$$

where

$$\bar{P}_{0,0}(\cos\theta) = 1\,, \quad \bar{P}_{1,1}(\cos\theta) = \sqrt{3}\,\sin\theta\,. \tag{B.4}$$

2) $\bar{P}'_{n,m}(\cos\theta) = d\,\bar{P}_{n,m}(\cos\theta)/d\theta$

$$\bar{P}'_{n,n}(\cos\theta) = \sqrt{\frac{2n+1}{2n}}\left(\sin\theta\,\bar{P}'_{n-1,n-1}(\cos\theta) + \cos\theta\,\bar{P}_{n-1,n-1}(\cos\theta)\right), \quad (n = m,\, n \geq 2)\,, \tag{B.5}$$

$$\bar{P}'_{n,m}(\cos\theta) = \frac{1}{\sin\theta}\left(n\cos\theta\,\bar{P}_{n,m}(\cos\theta) - \sqrt{\frac{(n^2-m^2)(2n+1)}{2n-1}}\,\bar{P}_{n-1,m}(\cos\theta)\right),$$

$(n \geq m+1,\, n \geq 1)\,,$ (B.6)

where

$$\bar{P}'_{0,0}(\cos\theta) = 0\,, \quad \bar{P}'_{1,1}(\cos\theta) = \sqrt{3}\,\cos\theta\,. \tag{B.7}$$

3) $\bar{P}''_{n,m}(\cos\theta) = d^2\bar{P}_{n,m}(\cos\theta)/d\theta^2$

The 2nd partial derivative of the associated Legendre function can be computed using the following equation (see, Heiskanen and Moritz (1967), Eq. (1-49)):

$$\sin\theta\,\bar{P}''_{n,m}(\cos\theta) + \cos\theta\,\bar{P}'_{n,m}(\cos\theta) + \left(n(n+1)\sin\theta - \frac{m^2}{\sin\theta}\right)\bar{P}_{n,m}(\cos\theta) = 0\,. \tag{B.8}$$

APPENDIX C

REFERENCE FRAME TRANSFORMATIONS USED IN ORBIT ESTIMATION

Due to the fact that no clear distinction can be made between precession and nutation, the International Earth Rotation and Reference System Service (IERS) adopted new methods for the transformation between the celestial and terrestrial reference systems based on the kinematical definition of the Celestial Reference System (CRS) (Capitaine, 2002; McCarthy and Petit, 2003).

Let $\boldsymbol{P}_0$ and $\boldsymbol{\sigma}_0$ be the reference pole and the reference origin of the right ascension at some fundamental epoch, t_0, respectively. The position of the instantaneous pole, $\boldsymbol{P}$, on the celestial sphere at the epoch of date, t, can be described by two celestial coordinates, declination (d) and right ascension (E) (see Figure C.1). The origin for the right ascension, $\boldsymbol{\sigma}$, at the epoch of date, t, is defined kinematically under the condition that there is no rotation rate in the CRS about the pole due to precession and nutation, which is the concept of the non-rotating origin (NRO). This origin for right ascension on the instantaneous equator is called the Celestial Ephemeris Origin (CEO). This CEO-based transformation is consistent with IAU 2000A precession-nutation model.

The new method of coordinate transformation between the terrestrial reference system (TRS) and CRS at the epoch, t, of the observation can be given by

$$[CRS] = Q(t) \cdot R(t) \cdot W(t)\ [TRS], \tag{C.1}$$

where

$Q(t)$: the matrix arising from the motion of the celestial pole in the celestial system;

$R(t)$: the matrix arising from the rotation of the Earth around the axis of the

pole;

$W(t)$: the matrix arising from the polar motion.

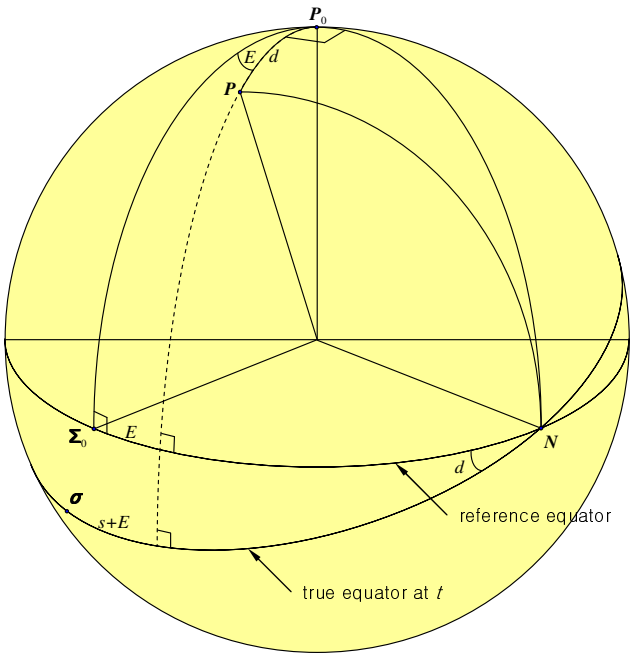

Figure C.1 Coordinates of instantaneous pole in the celestial reference system.

The frame, as realized from the TRS, by applying the transformations $W(t)$ and then $R(t)$ is called "the intermediate reference frame of epoch *t*."

The transformation matrix, $Q(t)$, from the system of the instantaneous pole and origin to the CRS, can be represented as

$$Q(t) = R_3(-E) \cdot R_2(-d) \cdot R_3(E) \cdot R_3(s), \tag{C.2}$$

where R_1, R_2 and R_3 denote the rotation about the x-axis, y-axis and z-axis, respectively, by the angle given as the parameter. Eq. (C.2) can be easily understood by considering the transformation of the origin point between the CRS origin, $\boldsymbol{\Sigma}_0$, and $\boldsymbol{\sigma}$. The additional parameter, *s*, in Eq. (C.2), is given by

$$s(t) = s(t_0) - \int_{t_0}^{t} \frac{X(t)\dot{Y}(t) - Y(t)\dot{X}(t)}{1 + Z(t)} dt \,, \tag{C.3}$$

where the arbitrary constant $s(t_0)$ is chosen to ensure continuity with the classical procedure at the date of change (1 January 2003) (McCarthy and Petit, 2003), that is,

$$s_0 = s(t_0) = +94 \mu as \,. \tag{C.4}$$

Since E and d are the coordinates of the instantaneous pole, $\boldsymbol{P}$, in the CRS, the coordinates used in Eq. (C.3) can be defined by

$$\begin{pmatrix} X \\ Y \\ Z \end{pmatrix} = \begin{pmatrix} \sin d \cos E \\ \sin d \sin E \\ \cos d \end{pmatrix}. \tag{C.5}$$

Substituting Eq. (C.5) into Eq. (C.2) yields the transformation matrix, Q, in a more explicit form as

$$Q(t) = \begin{pmatrix} 1 - aX^2 & -aXY & X \\ -aXY & 1 - aY^2 & Y \\ -X & -Y & 1 - a\left(X^2 + Y^2\right) \end{pmatrix} \cdot R_3(s), \tag{C.6}$$

where $a = 1/\left(1 + \cos d\right)$. The quantities used in Eq. (C.6) can be computed by the routine which is available at ftp://maia.usno.navy.mil/conv2003/chapter5/XYS2000A.f.

The transformation matrix for the polar motion, $W(t)$, can be expressed in terms of three fundamental components as follows:

$$W(t) = R_3(-s') \cdot R_2(x_p) \cdot R_1(y_p) \,, \tag{C.7}$$

where x_p and y_p are the "polar coordinates" of the Celestial Intermediate Pole (CIP) in the TRS, and s' is a quantity which provides the position of the Terrestrial Ephemeris Origin (TEO) on the equator of the CIP. The TEO is the non-rotating origin of the longitude, as is the case with the CEO. It should be noted that both the CEO and TEO represent an origin point associated with an instantaneous coordinate system which moves with respect to the reference system. The quantity, s', is necessary to provide an

exact realization of the "instantaneous prime meridian," which is given by

$$s' = (-47\mu as)\, t\,. \tag{C.8}$$

The parameter, t, in Eq. (C.8) is defined by

$$t = (\text{TT} - 2000 \text{ January 1d 12h TT}) \text{ in days} / 36525\,, \tag{C.9}$$

where TT represents the Terrestrial Time.

The transformation matrix for the Earth rotation, $R(t)$, is represented by

$$R(t) = R_3(-\theta)\,, \tag{C.10}$$

where θ denotes the Earth rotation angle between the CEO and the TEO at time t on the equator of the CIP, which provides a rigorous definition of the sidereal rotation of the Earth. The Earth rotation angle, θ, is given by

$$\theta(T_u) = 2\pi(0.7790572732640 + 1.00273781191135448T_u)\,, \tag{C.11}$$

where $T_u = (\text{Julian UT1 date} - 2451545.0)$.

For further explanation on this transformation method, one can refer to McCarthy and Petit (2003) and Jekeli (2005).